



uOttawa

L'Université canadienne
Canada's university

Finite Element Methods for a Microstructure-Based Model of Blood

Alexandre Iolov

Thesis Submitted to the Faculty of Graduate and Postdoctoral Studies
In partial fulfilment of the requirements for the degree of Master of Science in
Mathematics ¹

Department of Mathematics and Statistics
Faculty of Science
University of Ottawa

© Alexandre Iolov, Ottawa, Canada, 2009

¹The M.Sc. program is a joint program with Carleton University, administered by the Ottawa-Carleton Institute of Mathematics and Statistics

Abstract

The goal of this thesis is to solve numerically the equations for viscoelastic fluid flow that arise from a model of human blood. The model accounts for the elastic stress acting on the flow using a microstructure variable which itself depends on the flow. The resulting coupling offers a challenging numerical problem which however is capable of reproducing experimental results. This work implements a general Finite Element Code for solving the equations of motion, stress and microstructure state. Our work sought to validate the numerical scheme in two geometries, coaxial cylinders and a flat channel, and to further explore the model under a pulsatile flow regime in a non-trivial geometry – a dilated channel.

Acknowledgements

I would like to thank my supervisor, Professor Yves Bourgault; Professors Robert Owens at the Université de Montréal and André Fortin at the Université de Laval; Sabou Kane, Eric Chamberlain and Cristian Tibirna at GIREF; my Applied Math colleagues at UofO, my parents, my brother and Kirsten.

Contents

Abstract	ii
Acknowledgements	iii
List of Figures	vii
List of Tables	x
1 Mathematical Modelling of Blood Flow	1
1.1 Introduction	2
1.2 Navier-Stokes Equations	2
1.3 Oldroyd-B Equation	3
1.4 Rheological Models for Blood	4
1.5 A Microstructure-Based Model for Blood Fluid Mechanics	5
1.5.1 Non-dimensionalizing the Equations	8
1.5.2 Boundary Conditions	9
1.6 Outline of the Thesis	10
2 Finite Element Approximation	11
2.1 Finite Element Fundamentals	11
2.1.1 Weak Formulation of a PDE	11
2.1.2 The Galerkin Approach	13

2.1.3	inf-sup Conditions - Well-Posedness of the Discrete Problem	15
2.2	Finite Element Methods for Viscoelastic Flows	16
2.2.1	Discrete Elastic-Viscous Stress Splitting - DEVSS	17
2.2.2	The Petrov-Galerkin Approach - Streamline Upwinding	17
2.3	Time-Stepping	19
2.4	The Weak System	20
2.4.1	Picard Iteration	21
2.5	MEF++	23
3	Numerical Experiments	24
3.1	Coaxial Rheometer	25
3.1.1	Imposed Velocity	26
3.1.2	Resolution of Fully Coupled System	31
3.2	Flows in a Straight Channel	34
3.2.1	Geometry and Boundary Conditions for Flow in a Straight Channel	35
3.2.2	Steady Flow Experiment	36
3.2.3	Numerical Validation - Steady Shear Flows	37
3.2.4	Mesh Convergence	41
3.2.5	Determination of the apparent viscosity, η_a , for an equiva- lent Newtonian fluid	44
3.3	Flows in a Dilated Channel	46
3.3.1	Geometry and Boundary Conditions for Flow in a Dilated Channel	47
3.3.2	Steady Flow	49
3.3.3	Mesh Independence Study	52
3.3.4	Pulsatile Experiments	52
3.3.5	Comparison against Newtonian Flows	64

4 Conclusions

74

List of Figures

1.1 Hookean dumbbell model.	5
3.1 Flow in a coaxial rheometer - geometry and boundary conditions. See text for details.	25
3.2 Functional form of the applied shear rate, $\dot{\gamma}(t)$, for the coaxial rheometer experiment.	26
3.3 Close-up of the mesh for the coaxial rheometer experiment.	27
3.4 Graphs of model parameters as functions of $\dot{\gamma}$	28
3.5 Time plot of the solution \hat{N} (at top) and $\tau_{r\theta}$ (at bottom) for $\dot{\gamma}_{max} =$ 0.1, 0.29, 0.84.	29
3.6 Comparison of Matlab and FE numerical solutions.	31
3.7 Surface plots of \hat{N} and $ \boldsymbol{\tau} _{Frob}$ in the coaxial rheometer.	32
3.8 Comparison of coupled vs. uncoupled solutions.	33
3.9 Surface plots of \hat{N} and $ \boldsymbol{\tau} _{Frob}$ in the coaxial rheometer for the cou- pled problem.	34
3.10 Flow in a straight channel - geometry and boundary conditions. See text for details.	36
3.11 Mesh X1 for the straight channel.	37
3.12 Steady flow in a straight channel.	38
3.13 Steady flow in a straight channel, cut at $x = 4$	39

3.14 Cross-wise distribution for different profiles for De	40
3.15 $\tilde{e}_{\tau_{xx}}, \tilde{e}_{\tau_{xy}}$ for different De 's.	42
3.16 \hat{N} with mesh refinement.	43
3.17 u_x in straight channel with mesh refinement.	44
3.18 τ_{xx} with mesh refinement.	45
3.19 τ_{xy} with mesh refinement.	45
3.20 Pressure drops for Newtonian and viscoelastic fluids in straight channel.	47
3.21 Flow in a dilated channel - geometry and boundary conditions. See text for details.	48
3.22 The mesh X8 for the dilated channel.	49
3.23 Steady Flow in a Dilated Channel.	50
3.24 Steady Flow – cut at $x = 3.3$	53
3.25 Steady Flow – cut at $x = 4.7$	54
3.26 Steady Flow – cut at $x = 5.3$	55
3.27 Observation time instances for pulsatile flows.	57
3.28 Horizontal velocity, u_x , at times $I - IV$ of the pulsating test case. . .	58
3.29 Vertical velocity, u_y , at times $I - IV$ of the pulsating test case. . . .	59
3.30 Average rouleau size, \hat{N} , at times $I - IV$ of the pulsating test case. .	60
3.31 Component τ_{xx} of the elastic-stress tensor, at times $I - IV$ of the pulsating test case.	61
3.32 Component τ_{xy} of the elastic-stress tensor, at times $I - IV$ of the pulsating test case.	62
3.33 Component τ_{yy} of the elastic-stress tensor, at times $I - IV$ of the pulsating test case.	63
3.34 Time evolution for $\mathbf{u}, \hat{N}, \boldsymbol{\tau}$ over three pulsatile cycles inside the dilation of the dilated channel.	65

3.35 Pressure drops for a Newtonian fluid and a viscoelastic fluid in a dilated channel.	66
3.36 Comparison between u_x for a Newtonian fluid (blue) and the viscoelastic fluid (red) at four different times. The cut is taken along $x = 3.3$	68
3.37 Comparison between u_y for a Newtonian fluid (blue) and a viscoelastic fluid (red) at four different times. The cut is taken along $x = 3.3$	69
3.38 Comparison between σ_{xx} for a Newtonian fluid (blue) and a viscoelastic fluid (red) at four different times. The cut is taken along $x = 3.3$	70
3.39 Comparison between σ_{xy} for a Newtonian fluid (blue) and a viscoelastic fluid (red) at four different times. The cut is taken along $x = 3.3$	71
3.40 Comparison between σ_{yy} for a Newtonian fluid (blue) and a viscoelastic fluid (red) at four different times. The cut is taken along $x = 3.3$	72
3.41 Comparison between σ_{xy} for a Newtonian fluid (blue) and a viscoelastic fluid (red) over three pulsatile cycles at the top of the dilation, $(x, y) = (4, 1.81)$	73

List of Tables

3.1	Parameter values for the coaxial rheometer test case.	30
3.2	Parameter values for the channel test cases.	35
3.3	Errors for the viscoelastic variables in a straight channel.	41
3.4	Straight Channel Meshes.	43
3.5	Dilated channel meshes.	52
3.6	Pulsatile Parameters.	56

Chapter 1

Mathematical Modelling of Blood Flow

This thesis seeks to demonstrate the numerical resolution in arbitrary geometries of a very recent (2006) mechanical model for blood flow. It uses the finite element method for discretizing the resulting partial differential equations (PDE's). The model, due to Owens (the original reference is [20]), describes the effect of blood cells suspended in its plasma solvent on the overall macroscopic properties of the fluid such as viscous and elastic stress. The original content of our work lies primarily in the fact that a numerical resolution of the model under study has not yet been implemented in arbitrary spatial domains.

The current chapter on mathematical modeling first introduces the Navier-Stokes and Oldroyd-B equations, which are fundamental to the rheology of viscoelastic fluids. It then discusses several existing rheological models for blood and finally it introduces, in minimum detail necessary to appreciate the resulting numerical challenges and physical implications, the model of Owens [20] and the final form of the equations to be solved.

1.1 Introduction

Haemorheology is the study of how blood flows. Its primary variables of interest are the velocity at a given point in space (i.e we will take the Eulerian viewpoint), which will be denoted \mathbf{u} ; the scalar pressure, denoted p , and the total stress on the fluid, $\boldsymbol{\sigma}$, a tensor conventionally known as the Cauchy stress tensor. As for all fluids, the motion of blood is dictated by a balance of mass and forces. Given that for practical applications blood is incompressible, its conservation of mass equation also known as the continuity equation becomes:

$$\nabla \cdot \mathbf{u} = 0 \quad (1.1.1)$$

The forces acting on the fluid can be decomposed into body forces, \mathbf{f} , such as gravity or fictitious forces, and the pressure and stress, p and $\boldsymbol{\sigma}$. Coarsely speaking, $\boldsymbol{\sigma}$ lumps in all other internal or boundary forces such as traction. Balance of linear momentum then gives,

$$\rho_f \frac{D\mathbf{u}}{Dt} = -\nabla p + \rho_f \mathbf{f} + \nabla \cdot \boldsymbol{\sigma} \quad (1.1.2)$$

where ρ_f is the fluid density and $\frac{D}{Dt}$ is the material derivative of \mathbf{u} associated with the fact that variables at a given point in space are advected downstream by the flow, $\frac{D}{Dt} := \frac{\partial}{\partial t} + (\mathbf{u} \cdot \nabla)$.

1.2 Navier-Stokes Equations

Fluids differ in type by the expression for their internal stress $\boldsymbol{\sigma}$. The most fundamental case, viz. Newtonian fluids, expresses $\boldsymbol{\sigma}$ as proportional to the deformation-rate tensor, $\dot{\boldsymbol{\gamma}}(\mathbf{u}) = \frac{1}{2}(\nabla \mathbf{u} + \nabla \mathbf{u}^T)$. Then $\boldsymbol{\sigma} = 2\eta_N \dot{\boldsymbol{\gamma}}$, where η_N is a constant scalar called the viscosity. In this case, and neglecting body forces, we obtain the Navier-Stokes equations for a Newtonian fluid:

$$\rho_f \frac{D\mathbf{u}}{Dt} = -\nabla p + \nabla \cdot (2\eta_N \dot{\boldsymbol{\gamma}}) \quad (1.2.1)$$

The incompressible Navier-Stokes equations, (1.1.1) - (1.1.2), form the foundations of classical fluid dynamics. Relatively simple derivations can be found in [14] or [21]. Detailed discussions of their physics can be found in [2]. A classical reference for their mathematical analysis is [16].

1.3 Oldroyd-B Equation

The Newtonian expression for the internal stress is sufficient for simple fluids such as water or air, but not so for more complex ones such as molten plastics or body fluids. Much can be accomplished in this regard by considering the mechanical effect of microstructures such as long polymer chains suspended in the fluid. The Oldroyd-B equation expresses one of the simplest such relations and is derivable from kinetic theory if the microstructures are modeled as infinitely extensible Hookean dumbbells. A Hookean dumbbell is an elementary physical object representing two spherical masses connected by a Hookean spring. Derivations of the constitutive equation for the extra-stress tensor due to interactions between an ensemble of dumbbells and an immersing solvent can be found in [21] or [3]. Decomposing the stress tensor into viscous and elastic parts, $\boldsymbol{\sigma} = 2\eta_N\dot{\boldsymbol{\gamma}} + \boldsymbol{\tau}$, where $\dot{\boldsymbol{\gamma}}$ is the rate-of-deformation tensor, on the other hand, η_N is the plasma viscosity and $\boldsymbol{\tau}$ is the contribution of the elastic dumbbells to the stress, gives the following equation for $\boldsymbol{\tau}$:

$$\boldsymbol{\tau} + \mu \left(\frac{\partial \boldsymbol{\tau}}{\partial t} + (\mathbf{u} \cdot \nabla) \boldsymbol{\tau} - \nabla \mathbf{u} \cdot \boldsymbol{\tau} - \boldsymbol{\tau} \cdot \nabla \mathbf{u}^T \right) = 2\eta_p \dot{\boldsymbol{\gamma}}(\mathbf{u}) \quad (1.3.1)$$

The parameter μ is called the relaxation time and controls the delay between a change in the flow's shear rate $\dot{\boldsymbol{\gamma}}$ and the ensuing response in $\boldsymbol{\tau}$. In the case of simple shearing flow in the x - y plane such that $\mathbf{u} = (u_x(y), 0, 0)^T$, then $\dot{\boldsymbol{\gamma}} = |\partial_y u_x(y)|$. In the general case, $\dot{\boldsymbol{\gamma}} = \sqrt{2\dot{\boldsymbol{\gamma}} : \dot{\boldsymbol{\gamma}}}$, i.e. the shear rate is proportional to the modulus of the deformation-rate tensor. The coefficient η_p is called the polymeric viscosity.

1.4 Rheological Models for Blood

Several experimental studies have been done on the rheological properties of blood (e.g. [4], [22]). Notably they demonstrate that blood has non-constant viscosity with respect to shear, displays hysteresis, and is elastic at low shear rates.

A first attempt at modeling these phenomena is made by the class of models called Generalized Newtonian. In this case the viscosity in equation (1.2.1) becomes a function of the local shear-rate, $\eta_N = \eta_N(\dot{\gamma})$. An example, the application of the Herschel-Bulkley model to pulsatile flow through a stenosis is discussed in [23]. A similar comparison but with different expressions for the viscosity can be found in a 2003 paper of Neofytou et al. [19]. It compares the Quemada, Power-Law and Casson models. Another example is the Cross model [24]:

$$\eta(\dot{\gamma}) = \eta_0 \left(\frac{1 + \eta_\infty \beta / \eta_0 \dot{\gamma}^m}{1 + \beta \dot{\gamma}^m} \right) \quad (1.4.1)$$

In a broad review of this and several similar constitutive equations, Zhang and Kuang, [24], also introduce their bi-exponent equation in which an attempt is made to relate the parameters in the expression for η_N with the propensity of red blood cells to aggregate into and fragment out of network-like microstructures called rouleaux.

None of these however can account for the elasticity of blood, for example the residual stress on the fluid after a flow has come to rest. More generally they cannot describe hysteresis in the stress, i.e that given an applied increase and then symmetric decrease in the shear-rate, the stress evolution will not be asymmetric. Accounting for these however is possible with a more general model like Oldroyd-B. Using an Oldroyd-B type constitutive equation allows for a more physically-grounded description, since the peculiar features of the bulk flow can be seen to arise directly out of the effect of the cells suspended in it. An example of such a model is developed by Owens et al. in a series of papers starting with [20] and it is this that serves as basis for our numerical work.



Figure 1.1: *Hookean dumbbell model. Representation of a blood cell aggregation as a Hookean dumbbell*

1.5 A Microstructure-Based Model for Blood Fluid Mechanics

The main difference between blood and water is that alongside the plasma about half of its volume is occupied by red blood cells (RBC's). Since an RBC is significantly larger than water molecules, but still significantly smaller than the diameter of anything but the smallest arterioles (an RBC has diameter of $8\mu m$, while vessel diameters considered here have diameter on the order of $0.5mm$), this makes them appropriate to be represented by the Oldroyd-B model. The original paper of Owens [20] derives a model where the Oldroyd-B Hookean dumbbells correspond to coin-stack like columns called rouleaux (see Fig. 1.1). The difference with the classical Oldroyd-B model is that in the Owens model, a Hookean dumbbell can change its constitution during the flow as the cells aggregate and fragment out of a rouleau. Thus additionally to the stress due to the dumbbells (rouleaux) one must also consider the evolution of the dumbbell size.

Here we will quickly and roughly go over the equations related to the fluid model. A thorough discussion of their derivation can be found in the original papers [20],[17]. A representative length of the dumbbells is obtained by considering the number of cells in a rouleau. A complication immediately seen is that at any given time and point

in space there are rouleaux of various sizes which would have to be represented by dumbbells of various lengths and tensile properties. Working with this will necessitate a multi-mode Oldroyd-B equation where the elastic stress is a sum of all the stresses corresponding to the different dumbbells lengths, $\boldsymbol{\tau} = \boldsymbol{\tau}_k$. A simplification is to consider a representative rouleau size, $N(\boldsymbol{x}, t)$, assume *all* stacks in a control volume are of length N and set it to be the average length, $N = \hat{N}$. A rouleau of cells is a transient object whose interaction with other rouleaux or with the flow itself results in it aggregating with others to form bigger rouleaux or in itself fragmenting into smaller ones. Resolving the resulting aggregation-fragmentation equations results in the following advection-reaction equation for \hat{N}

$$\frac{D\hat{N}}{Dt} + \frac{1}{2}\mathbf{b}(\dot{\gamma})(\hat{N} - \hat{N}_{st})(\hat{N} + \hat{N}_{st} - 1) = 0 \quad (1.5.1)$$

Here $\mathbf{b}(\dot{\gamma})$ is a fragmentation rate and $\hat{N}_{st} = \hat{N}_{st}(\dot{\gamma})$ is the equilibrium value of \hat{N} given a steady flow. The value of \hat{N} , the average rouleau size, has an effect over the macroscopic elastic stress, $\boldsymbol{\tau}$ in (1.3.1), via its relaxation time, μ , in the following manner:

$$\mu = \mu(\hat{N}) = \frac{\lambda_H \hat{N}}{1 + g_{\hat{N}} \hat{N} \lambda_H}, \quad (1.5.2)$$

where $g_{\hat{N}}$ is an aggregation coefficient associated with stacks of length \hat{N} , such that $g_{\hat{N}} \hat{N} = (1/2)\mathbf{b}(\dot{\gamma})\hat{N}(\hat{N} - 1) + \mathbf{a}(\dot{\gamma})$, $\mathbf{a}(\dot{\gamma})$ is an aggregation rate for the RBC's and λ_H is the relaxation time associated with a single blood cell. In particular we would expect that at infinite shear-rates, all rouleaux would break up and therefore $\mu \rightarrow \lambda_H$ as $\dot{\gamma} \rightarrow \infty$. There is no experimental or theoretical form for the exact expression of the aggregation rate, $\mathbf{a}(\dot{\gamma})$. Heuristically, $\mathbf{a}(\dot{\gamma})$ has been assumed to be concave down such that it is linearly increasing at low shear-rates and goes to zero at very large shear-rates. Strictly speaking, $\mathbf{a}(\dot{\gamma})$ represents a sticking probability and therefore is a function of the RBC number density. However, since we assume the same RBC number density throughout the computational domain, we will ignore that. The later

papers of Owens *et al.*, [17][8], take into account that in small vessels the cell density is not uniform and that in particular there is a cell-depleted slippage layer near the walls. We will ignore this effect here. The assumed form for the aggregation rate will be a piecewise cubic polynomial in $\dot{\gamma}$ as follows:

$$\mathbf{a}(\dot{\gamma}) = \begin{cases} \sum_{i \leq 3} a_{1,i} \dot{\gamma}^i & \text{if } \dot{\gamma} \leq \dot{\gamma}_{crit} \\ \sum_{i \leq 3} a_{2,i} \dot{\gamma}^i & \text{if } \dot{\gamma} \in (\dot{\gamma}_{crit}, \dot{\gamma}_{max}) \\ 0 & \text{if } \dot{\gamma} \geq \dot{\gamma}_{max} \end{cases} \quad (1.5.3)$$

The values of $a_{j,i}$, $\dot{\gamma}_{crit}$, $\dot{\gamma}_{max}$ can be found tabulated along with the other parameter values in Ch. 3. The expression for $\mathbf{b}(\dot{\gamma})$ can then be determined by considering a balance in the case of steady shear such that:

$$\mathbf{b}(\dot{\gamma}) = \frac{\mathbf{a}(\dot{\gamma})}{\hat{N}_{st}(\hat{N}_{st} - 1)} \quad (1.5.4)$$

What remains is to express \hat{N}_{st} in terms of measurable quantities. Supposing that the polymeric viscosity η_p is proportional to the relaxation time μ and using the expression for μ , (1.5.2), implies that in a steady shear flow:

$$\eta_p = \frac{\eta_\infty \hat{N}_{st}}{1 + (3/2)\mathbf{a}(\dot{\gamma})\lambda_H} \quad (1.5.5)$$

Here η_∞ refers to the asymptotic value of η_p at infinite shear.

On the other hand, one can fit experimental data for *steady* shear to a Cross model (see Eq. (1.4.1)) such that the polymeric viscosity, η_p , is set to:

$$\eta_p(\dot{\gamma}) = \eta_0 \left(\frac{1 + \theta \dot{\gamma}^m}{1 + \beta \dot{\gamma}^m} \right) \quad (1.5.6)$$

where η_0 is the zero-shear polymeric viscosity, β and m are Cross Model parameters and $\theta := \eta_\infty \beta / \eta_0$.

Combining equations (1.5.5) and (1.5.6) one can solve for the average rouleau size, \hat{N}_{st} to obtain:

$$\hat{N}_{st} = \frac{\eta_0}{\eta_\infty} \left(\frac{1 + \theta \dot{\gamma}^m}{1 + \beta \dot{\gamma}^m} \right) (1 + (3/2)\mathbf{a}(\dot{\gamma})\lambda_H) \quad (1.5.7)$$

With that we can refer anew to the equation for the elastic stress in an Oldroyd-B fluid (1.3.1) where the functional form for its parameters, namely η_p and μ , have now been fully described.

1.5.1 Non-dimensionalizing the Equations

Similarly to what is done in [17], characteristic scales can be introduced as follows: Define characteristic length L and velocity U . From this one obtains a corresponding characteristic time $T = \frac{L}{U}$. Then non-dimensional variables can be defined as :

$$\begin{aligned} x' &= \frac{x}{L} & t' &= \frac{t}{T} & \mathbf{u}' &= \frac{\mathbf{u}}{U} \\ \boldsymbol{\tau}' &= \boldsymbol{\tau} \frac{\lambda_H}{\eta_\infty} & p' &= p \frac{\lambda_H}{\eta_\infty} & \hat{N}' &= \hat{N} \end{aligned}$$

Introduce the shear-rate dependent Deborah number De and its corresponding value at infinite shear De_∞

$$\text{De} = \mu \frac{U}{L} \quad \text{De}_\infty = \lambda_H \frac{U}{L} \quad (1.5.8)$$

After non-dimensionalizing our aggregation-fragmentation rates the constitutive equation, Eq. (1.3.1) is transformed to read:

$$\boldsymbol{\tau}' + \text{De} \left(\frac{\partial \boldsymbol{\tau}'}{\partial t'} + \mathbf{u}' \cdot \nabla' \boldsymbol{\tau}' - \nabla' \mathbf{u}' \cdot \boldsymbol{\tau}' - \boldsymbol{\tau}' \cdot \nabla' \mathbf{u}'^T \right) = 2\text{De} \dot{\boldsymbol{\gamma}}'(\mathbf{u}')$$

The second important non-dimensional number in viscoelastic flows is the Reynolds number, Re , whose definition here differs slightly from what is standard in the case of a Newtonian fluid.

$$\text{Re} = \frac{\rho_f U L \text{De}_\infty}{\eta_\infty}$$

We also define a non-dimensional plasma viscosity, η_s .

$$\eta_s = \frac{\eta_N \text{De}_\infty}{\eta_\infty}$$

The non-dimensional momentum equation becomes:

$$\text{Re} \frac{D\mathbf{u}}{Dt} - \eta_s \nabla \cdot \dot{\boldsymbol{\gamma}} - \nabla \cdot \boldsymbol{\tau} + \nabla p = 0 \quad (1.5.9)$$

The advection-reaction equation for \hat{N} , (1.5.1), is easily transformed after replacing the dimensional rates, $\mathbf{b}(\dot{\boldsymbol{\gamma}})$ and $\mathbf{a}(\dot{\boldsymbol{\gamma}})$ with their non-dimensional versions, respectively $\mathbf{b}'(\dot{\boldsymbol{\gamma}}')$ and $\mathbf{a}'(\dot{\boldsymbol{\gamma}}')$, where

$$\mathbf{b}'(\dot{\boldsymbol{\gamma}}') = \frac{L}{U} \mathbf{b}(\dot{\boldsymbol{\gamma}}) \quad \mathbf{a}'(\dot{\boldsymbol{\gamma}}') = \frac{L}{\bar{v}} \mathbf{a}(\dot{\boldsymbol{\gamma}})$$

Finally dropping the primes we have the complete set of equations to be solved:

$$\text{Re} \frac{D\mathbf{u}}{Dt} - 2\eta_s \nabla \cdot \dot{\boldsymbol{\gamma}} - \nabla \cdot \boldsymbol{\tau} + \nabla p = 0 \quad (1.5.10)$$

$$\nabla \cdot \mathbf{u} = 0 \quad (1.5.11)$$

$$\frac{D\hat{N}}{Dt} + \frac{1}{2} b(\dot{\boldsymbol{\gamma}})(\hat{N} - \hat{N}_{st})(\hat{N} + \hat{N}_{st} - 1) = 0 \quad (1.5.12)$$

$$\boldsymbol{\tau} + \text{De} \left(\frac{\partial \boldsymbol{\tau}}{\partial t} + (\mathbf{u} \cdot \nabla) \boldsymbol{\tau} - \nabla \mathbf{u} \cdot \boldsymbol{\tau} - \boldsymbol{\tau} \cdot \nabla \mathbf{u}^T \right) = 2\text{De} \dot{\boldsymbol{\gamma}}(\mathbf{u}) \quad (1.5.13)$$

1.5.2 Boundary Conditions

In order to close the system (1.5.10) - (1.5.13), an appropriate set of boundary conditions (BCs) is required. Once we have a domain Ω with boundary Γ , we will impose BCs as follows. First split Γ into three disjoint sets, Γ_i , Γ_o , Γ_w , respectively the inlet boundary, the outlet boundary and the walls. Along Γ_i , we will specify Dirichlet boundary conditions for \mathbf{u} , \hat{N} and $\boldsymbol{\tau}$. Since equations (1.5.12) and (1.5.13) are advection-reaction equations for a given velocity \mathbf{u} , Γ_i is the only place where we need to specify boundary conditions for \hat{N} and $\boldsymbol{\tau}$. For the velocity, we will further specify a no-slip condition along Γ_w , which means that \mathbf{u} moves with the walls and in particular that along fixed walls $\mathbf{u} = 0$. Finally along Γ_o , we will specify a mixed Dirichlet-Neumann boundary condition for the velocity. We will impose $\mathbf{u} \parallel \mathbf{n}_o$ and $[-p\mathbf{I} + 2\eta_s \dot{\boldsymbol{\gamma}}] \mathbf{n}_o = \mathbf{0}$, where \mathbf{n}_o is normal to Γ_o and $\mathbf{u} \parallel \mathbf{n}_o$ indicates that the velocity

is prescribed to be parallel to the normal. These boundary conditions anticipate the treatment of the various terms in the weak form of the equations as discussed in Ch. 2.

This thesis is the first instance, to our knowledge, where equations (1.5.10)-(1.5.13) are solved for in arbitrary spatial geometries. Note that although we restrict ourselves to 2D geometries here, the code 'as is' is capable of handling three dimensional problems.

1.6 Outline of the Thesis

The thesis is structured as follows: In chapter 1, we have described the physical background and the mathematical details of the model. In chapter 2, we discuss the discretization techniques necessary to solve the PDE's numerically. In chapter 3, we discuss numerical results including code validation. Finally the last chapter concludes with some general remarks including suggested future work.

Chapter 2

Finite Element Approximation

This chapter on the numerical discretization of the viscoelastic model (1.5.10)-(1.5.13), is divided into five sections. In the first section, we introduce the basics of the finite element method, while in the second we discuss the details most pertinent to viscoelastic flows. The third section presents the methods used to deal with transient (i.e. time-dependent) solutions. Once these are detailed, we restate Eqs. (1.5.10)-(1.5.13) in the weak discretized form used for the numerical solution. In section five, we mention a few words about the software packages used to implement our scheme.

2.1 Finite Element Fundamentals

2.1.1 Weak Formulation of a PDE

The principle of the finite element method arises naturally from the variational or weak formulation of a PDE. Take for example the Navier-Stokes equations (1.5.10) - (1.5.11). If we assume that the equation is satisfied for some pair (\mathbf{u}, p) , then multiplying the momentum equation by a test function $\phi_{\mathbf{u}}$ and the continuity equation by a test function ϕ_p will not alter the equality.

Consider the functional space $\mathcal{U} = \{u \in \mathcal{L}^2(\Omega); \nabla \mathbf{u} \in \mathcal{L}^2(\Omega); \mathbf{u}|_{\Gamma_i} = \mathbf{u}_{\Gamma_i}, \mathbf{u}|_{\Gamma_w} =$

$\mathbf{u}_{\Gamma_w}, \mathbf{u}|_{\Gamma_o} \parallel \mathbf{n}_{\Gamma_o}\}$, where $\mathbf{u}_{\Gamma_i}, \mathbf{u}_{\Gamma_w}$ are given functions on the inlet and the walls respectively, \mathbf{n}_{Γ_o} is the normal to the outlet and $\mathbf{u}|_{\Gamma_o} \parallel \mathbf{n}_{\Gamma_o}$ indicates that at the outlet, the velocity is prescribed to be parallel to the outlet's normal. Also consider the functional space $\mathcal{P} = \{p \in \mathcal{L}^2(\Omega), \int_{\Omega} p = 0\}$. \mathcal{U} and \mathcal{P} are the spaces in which we will seek our solution pair (\mathbf{u}, p) .

We will take the multiplying test functions $\phi_{\mathbf{u}}$ to be in \mathcal{U}_{test} and ϕ_p to be in \mathcal{P}_{test} , which are defined as: $\mathcal{U}_{test} = \{(\phi_{\mathbf{u}} \in \mathcal{L}^2(\Omega); \nabla \phi_{\mathbf{u}} \in \mathcal{L}^2(\Omega); \phi_{\mathbf{u}}|_{\Gamma_i} = \phi_{\mathbf{u}}|_{\Gamma_w} = \mathbf{0}, \phi_{\mathbf{u}} \cdot \mathbf{t}_o|_{\Gamma_o} = 0\}$, $\mathcal{P}_{test} = \{\phi_p \in \mathcal{L}^2(\Omega), \int_{\Omega} p = 0\}$, where \mathbf{t}_o is a tangent to the outlet

Then after multiplying the equations by the test functions and integrating by parts the viscosity term, $-\nabla \cdot \dot{\gamma}(\mathbf{u})$, and the pressure gradient, ∇p , and using the BC's we obtain the variational form of the Navier-Stokes equations:

Find $\mathbf{u} \in \mathcal{U}$ and $p \in \mathcal{P}$ such that:

$$\begin{aligned} \operatorname{Re} \frac{d}{dt} \langle \mathbf{u}, \phi_{\mathbf{u}} \rangle + \operatorname{Re} c(\mathbf{u}, \mathbf{u}, \phi_{\mathbf{u}}) + \\ b(\phi_{\mathbf{u}}, p) + \eta_s a(\mathbf{u}, \phi_{\mathbf{u}}) = 0, \quad \forall \phi_{\mathbf{u}} \in \mathcal{U}_{test}, \end{aligned} \quad (2.1.1)$$

$$b(\mathbf{u}, \phi_p) = 0, \quad \forall \phi_p \in \mathcal{P}_{test}, \quad (2.1.2)$$

where the bilinear and trilinear forms are defined as follows:

$$\begin{aligned} \langle \mathbf{u}, \mathbf{v} \rangle &= \int_{\Omega} \mathbf{u} \cdot \mathbf{v} \quad ; \quad a(\mathbf{u}, \mathbf{v}) = \int_{\Omega} \dot{\gamma}(\mathbf{u}) : \dot{\gamma}(\mathbf{v}) \\ b(\mathbf{u}, p) &= \int_{\Omega} p \nabla \cdot \mathbf{u} \quad ; \quad c(\mathbf{u}, \mathbf{v}, \mathbf{w}) = \int_{\Omega} (\mathbf{u} \cdot \nabla) \mathbf{v} \cdot \mathbf{w} \end{aligned}$$

The numerical approach to this problem is to reduce the solution and test spaces to finite dimensions. The first fundamental technique, the Galerkin approach, used primarily for elliptic or parabolic PDE's, is now detailed. The second technique, the Petrov-Galerkin approach, used for advection-dominated equations, is detailed in section 2.2.2.

2.1.2 The Galerkin Approach

The finite element method approximates the solution of the PDE by a finite linear combination of basis functions defined on the domain which is decomposed into a finite number of elements (also called cells). We need the following definitions.

Definition 2.1.1 (Mesh) *A mesh or a tessellation \mathcal{M}_h of a domain Ω is a disjoint cover of Ω such that $\mathcal{M}_h = \bigcup_i K_i$, K_i is a polygonal geometrical shape and $K_i \cap K_{j \neq i}$ is at most a vertex, an edge or a face (in 3D).*

There are no theoretical restrictions on the type of polygons used. In practice one uses triangles or quadrilaterals in 2D and tetrahedra, pyramids, prisms or hexahedra in 3D. In this work all our meshes are triangular. Note that the term 'cover' is used loosely. If Ω itself is not a polygon, all one can hope for (and insist on) is that the element vertices lying on the exterior boundary of \mathcal{M}_h also lie on $\partial\Omega$. The subscript h on an object is used to indicate that the object is mesh-dependent. h itself denotes in some sense the size of the largest element in a mesh, for example the length of the longest edge. It is expected that as $h \rightarrow 0$, then $\mathcal{M}_h \rightarrow \Omega$.

With the domain thus partitioned into finite elements, one can now define a finite element basis on the mesh \mathcal{M}_h by:

Definition 2.1.2 (Basis Functions) *The family of functions $\{\phi_j\}$ defines basis functions if these functions are defined on the mesh \mathcal{M}_h and form a linearly independent set.*

A special type of a basis is called the nodal or Lagrangian basis.

Definition 2.1.3 (Lagrangian Basis) *A basis $\{\phi_j\}$ is Lagrangian if \exists a set of points $\{p_j\}$ on \mathcal{M}_h , such that the basis functions $\{\phi_i\}$ satisfy $\phi_i(p_j) = \delta_{ij}$*

There are a number of alternatives to Lagrangian-type elements, e.g the Crouzeix-Raviart elements, which are also frequently used for viscoelastic flow (see [11]), the Raviart-Thomas elements, or more exotically the Nedelec elements used in electromagnetism. Ern and Guermond [6] give a thorough discussion on finite elements.

Now consider again a domain Ω where the Navier-Stokes equations (1.5.10)-(1.5.11) are to be solved. Let \mathcal{M}_h be a mesh on Ω . Let $\{\phi_{\mathbf{u},i}\}$ be a vectorial Lagrangian basis on \mathcal{M}_h and let $\mathcal{U}_h = \{\mathbf{u}_h \in \text{span}(\phi_{\mathbf{u},i}); \mathbf{u}_h|_{\Gamma_i} = \Pi_h \mathbf{u}_{\Gamma_i}, \mathbf{u}_h|_{\Gamma_w} = \Pi_h \mathbf{u}_{\Gamma_w}, \mathbf{u}_h|_{\Gamma_o} \parallel \mathbf{n}_{\Gamma_o}\}$, where Π_h is the Lagrange interpolation operator (see [6]). Let $\{\phi_{p,i}\}$ be a scalar Lagrangian basis on \mathcal{M}_h and let $\mathcal{P}_h = \{p_h \in \text{span}(\phi_{p,i}) \subset \mathcal{P}\}$. The Galerkin approach uses basis $\{\phi_{\mathbf{u},i}\}$ and $\{\phi_{p,i}\}$ that are the same for both the trial and test spaces. For the Navier-Stokes equations this means:

Find $\mathbf{u}_h \in \mathcal{U}_h$ and $p_h \in \mathcal{P}_h$ such that:

$$\frac{d}{dt} \langle \mathbf{u}_h, \phi_{\mathbf{u}} \rangle + c(\mathbf{u}_h, \mathbf{u}_h, \phi_{\mathbf{u}}) + b(\phi_{\mathbf{u}}, p) + a(\mathbf{u}, \phi_{\mathbf{u}}) = 0, \quad \forall \phi_{\mathbf{u}} \in \mathcal{U}_{test,h}, \quad (2.1.3)$$

$$b(\mathbf{u}_h, \phi_p) = 0, \quad \forall \phi_p \in \mathcal{P}_{test,h}, \quad (2.1.4)$$

where $\mathcal{U}_{test,h} = \text{span}(\phi_{\mathbf{u},i}) \cap \mathcal{U}_{test}$ and $\mathcal{P}_{test,h} = \text{span}(\phi_{p,i}) \cap \mathcal{P}_{test}$.

Common spaces used in the Galerkin approach are continuous, piecewise polynomials, which are here defined:

Definition 2.1.4 (P_n spaces) Let \mathcal{M}_h be a mesh on Ω . Given a cell $K \in \mathcal{M}_h$, let $\mathbb{P}^n(K)$ be the space of polynomials of degree $\leq n$ restricted to K . Then the space P_n on \mathcal{M}_h is defined such that $\phi \in P_n$ whenever $\phi \in C^0(\Omega)$ and $\phi|_K \in \mathbb{P}^n(K)$, $\forall K \in \mathcal{M}_h$.

In the case of multi-dimensional variables (vectors or tensors), then a multi-dimensional P_n space is understood to have each of its components in P_n as a scalar.

2.1.3 inf-sup Conditions - Well-Posedness of the Discrete Problem

The spaces chosen in the continuous case satisfy an important well-posedness criterion, that is the spaces \mathcal{U} and \mathcal{P} are such that there exists a constant $\beta > 0$ for which

$$\inf_{p \in \mathcal{P}} \sup_{\mathbf{u} \in \mathcal{U}} \frac{b(\mathbf{u}, p)}{\|\mathbf{u}\|_1 \|p\|_0} > \beta,$$

where $\|\cdot\|_1$ and $\|\cdot\|_0$ indicate the $\mathcal{H}^1(\Omega)$ and $\mathcal{L}^2(\Omega)$ norms, respectively.

When one chooses discrete approximation spaces, \mathcal{U}_h and \mathcal{P}_h that are conformal, meaning they are subspaces of \mathcal{U} and \mathcal{P} , one still has to ensure that the discrete spaces for the velocity and the pressure satisfy the discrete version of the inf-sup condition. Inf-sup conditions are fundamental in the theoretical study of finite element methods. The velocity-pressure case is amongst the first pair of finite element spaces that demonstrated the importance of the discrete inf-sup condition, which bears the name (L)BB-condition after (Ladyzhenskaya), Babuska and Brezzi (see [6], [18]). A pair of approximation spaces known to satisfy an (L)BB-condition is the P_2/P_1 element also known as the Taylor-Hood element (a proof can be found in [6]), i.e. velocity is taken to be quadratic on each element and pressure is taken linear. An alternative is to use the Pressure-Stabilized Petrov-Galerkin method (PSPG) where instead of testing the momentum equation with $\phi_{\mathbf{u}}$, we instead test with $\phi_{\mathbf{u}} + \tau_K \nabla \phi_p$ (see [18] for instance). This approach is not explored in this work.

The zero-mean condition on p in the formulation of the problem, i.e. the requirement that $\int_{\Omega} p = 0$ guarantees the uniqueness of the solution, since without this zero-average condition, if p is a solution so would be $p + \alpha$, for any constant α . Therefore insisting that $\int_{\Omega} p = 0$ is a way of removing one degree of freedom from the solution space for the pressure. But though removing this degree-of-freedom by requiring the pressure average to be zero is convenient theoretically, it is expen-

sive computationally. There are other tricks to accomplish the removal of that extra degree-of-freedom, such as imposing the value of the pressure at a single node on the mesh. Our solver for the momentum-continuity equations applies a technique which is referred to as 'artificial compressibility' [6]. Namely, we add the term $\epsilon_h \int p \phi_p d\Omega$ to the continuity equation (2.1.4) so that it becomes

$$\int_{\Omega} \phi_p \nabla \cdot \mathbf{u}_h + \epsilon_h \int_{\Omega} p_h \phi_p = 0; \quad \forall \phi_p \in \mathcal{P}_{test,h}, \quad (2.1.5)$$

where ϵ_h is normally set to a very small value such as $1e-7$. As discussed in Sec. 4.4 of Ern and Guermond, [6], this will have the dual effect of removing the extra-degree for the pressure (i.e. making the discrete problem well-posed) and rendering the matrix of the resulting linear system positive-definite, thus improving the performance of the linear solvers. The fact that the solution is changed only slightly by the added 'artificial compressibility' term is proven in Sec. 4.4. of [6].

2.2 Finite Element Methods for Viscoelastic Flows

The extension of the finite elements techniques used in classical fluid mechanics to viscoelastic flows is not trivial. The problem in (\mathbf{u}_h, p_h) becomes a problem in $(\mathbf{u}_h, p_h, \boldsymbol{\tau}_h)$ and in the case when $\eta_s = 0$ in (1.5.10) one needs that the discrete deformation-rate tensor $\dot{\boldsymbol{\gamma}}(\mathbf{u}_h) \in \mathcal{T}_h$, where \mathcal{T}_h is the test space for $\boldsymbol{\tau}_h$. This implies for example that if we choose $\mathcal{T}_h \subset C^0(\Omega)$, then we must have $\mathcal{U}_h \subset C^1$, which puts a significant computational overhead. In that case or even in the case where η_s is small a commonly used technique to overcome this compatibility condition is to introduce artificial viscosity (i.e 'increase' η_s) and compensate for that by introducing an extra variable to keep the problem consistent. There are several ways to do this. In this work we have used the Discrete Elastic-Viscous Stress Splitting method (DEVSS) of Guénette, Fortin et al. (see e.g. [11]). This allows us to work with the standard continuous P_1 elements for the elastic stress. Another concern is the propensity of first-order advection equa-

tions to give rise to spurious oscillations near the boundary. These can occur for both the upper-convected derivative for $\boldsymbol{\tau}_h$ and the material derivative for \hat{N}_h appearing in the PDE's for these unknowns and must be addressed in both cases.

2.2.1 Discrete Elastic-Viscous Stress Splitting - DEVSS

One of the major tools in ensuring convergence in viscoelastic flow simulations is by enlarging the coercivity of the elliptic operator in the momentum equation while retaining the consistency of the discretization. This is performed by introducing an auxiliary variable \mathbf{d} and its corresponding discrete space \mathcal{D}_h , adding a term to the momentum equation, increasing the solvent viscosity and adding an extra equation for \mathbf{d} , which can be termed the projection equation for the deformation-rate tensor $\dot{\boldsymbol{\gamma}}(\mathbf{u}_h)$. This gives:

$$\begin{aligned} \text{Re} \left\langle \frac{D\mathbf{u}_h}{Dt}, \phi_{\mathbf{u}} \right\rangle - \alpha \langle \mathbf{d}, \nabla \phi_{\mathbf{u}} \rangle + (\alpha + 2\eta_s) \langle \dot{\boldsymbol{\gamma}}(\mathbf{u}_h), \nabla \phi_{\mathbf{u}} \rangle \\ - \langle \nabla \cdot \boldsymbol{\tau}_h, \phi_{\mathbf{u}} \rangle - \langle p, \nabla \cdot \phi_{\mathbf{u}} \rangle = 0; \quad \forall \phi_{\mathbf{u}} \in \mathcal{U}_{test,h}, \\ \langle \mathbf{d} - \dot{\boldsymbol{\gamma}}(\mathbf{u}_h), \phi_{\mathbf{d}} \rangle = 0; \quad \forall \phi_{\mathbf{d}} \in \mathcal{D}_{test,h}, \end{aligned}$$

The proper choice of α is elucidated in Fortin et al. [11] and like there we usually set $\alpha = \text{De}$. However note that it has been suggested in informal talks with students at l'Université Laval that in smooth geometries one can take α to be much smaller and thus speed up convergence. A full numerical analysis of the DEVSS method can be found in the series of papers by Fortin et al. ([12],[10], [11]).

2.2.2 The Petrov-Galerkin Approach - Streamline Upwinding

Advection equations require a departure from the standard Galerkin approach [21],[18]. Coarsely speaking, standard Galerkin approximation often results in spurious oscil-

lations in the discrete solution that are not present in the true solution. A possible rectification consists in using modified test functions [18].

Consider the residual of the equation for $\boldsymbol{\tau}_h$ in (1.5.13):

$$\mathbf{R}(\boldsymbol{\tau}_h) := \boldsymbol{\tau}_h + \text{De} \left(\frac{\partial \boldsymbol{\tau}_h}{\partial t} + (\mathbf{u} \cdot \nabla) \boldsymbol{\tau}_h - \nabla \mathbf{u} \cdot \boldsymbol{\tau}_h - \boldsymbol{\tau}_h \cdot \nabla \mathbf{u}^T \right) - 2\text{De} \dot{\boldsymbol{\gamma}}(\mathbf{u}),$$

Then the Petrov-Galerkin approach to testing this equation is by changing the test functions as:

$$\phi_{\boldsymbol{\tau}} \longrightarrow \phi_{\boldsymbol{\tau}} + \alpha_h^{SU} \mathbf{u} \cdot \nabla \phi_{\boldsymbol{\tau}},$$

where α_h^{SU} is a stabilization parameter. The definition of α_h^{SU} is element-dependent and is dictated in the case of advection-diffusion equations with diffusivity κ by the local element Peclet number $Pe_h = \|\mathbf{u}\| * h_K / \kappa$ [18]. Treating a pure-advection equation as the case $Pe \rightarrow \infty$, the inferred form for α_h^{SU} is:

$$\alpha_h^{SU} := \frac{h_K}{\|\mathbf{u}\|}$$

Note that when coupled to the Navier-Stokes equations, instead of being given, the velocity is obtained from the most recent solution to (1.5.10), (i.e. $\mathbf{u} = \mathbf{u}_h(t)$). Moreover to avoid numerical problems when $\mathbf{u}_h \rightarrow 0$ we modify the definition to read:

$$\alpha_h^{SU} := \frac{h_K}{\sqrt{\|\mathbf{u}\|^2 + 1}} \quad (2.2.1)$$

There are several variants such as setting $\alpha_h^{SU} = 0$ if $\|\mathbf{u}\| < \epsilon$ for some ϵ or changing the denominator as in: $\alpha_h^{SU} := h_K / \sqrt{\|\mathbf{u}\|^2 + \epsilon}$. But experimenting with all three did not result in significant differences in the results.

Having thus introduced the Petrov-Galerkin technique, we can state succinctly its application to the second pure-advection equation in our system, namely the microstructure evolution equation (1.5.12).

Let \mathcal{N}_h be an approximation space for the average rouleau size, \hat{N} , and consider the residual of Eq. (1.5.12):

$$\mathbf{R}(\hat{N}_h) := \frac{D\hat{N}_h}{Dt} + \frac{1}{2}b(\dot{\gamma})(\hat{N}_h - \hat{N}_{st})(\hat{N} + \hat{N}_{st} - 1)$$

Then we seek an $\hat{N}_h \in \mathcal{N}_h$ such that:

$$\langle \mathbf{R}(\hat{N}_h), \phi_{\hat{N}} + \alpha_h^{SU} \mathbf{u} \cdot \nabla \phi_{\hat{N}} \rangle = 0; \quad \forall \phi_{\hat{N}} \in \mathcal{N}_{test,h} \quad (2.2.2)$$

SUPG methods are also indicated for the treatment of the classical Navier-Stokes equations at high Reynolds numbers. However since $\text{Re} \ll 1000$ in our case, we do not use this approach for the momentum equation (1.5.10).

2.3 Time-Stepping

All weak formulations presented so far include a continuous expression for the time derivative. The final step then is to discretize the equations in time. Ch. 6 of [6] details the general approach for transient solutions with finite element methods. More specifically, section 6.4 of [21] is dedicated to the treatment of time-dependent viscoelastic flows such as the Oldroyd-B equation. As is standard in the finite element method, we first discretize in space and then in time. Consider the equation for \hat{N} :

$$\frac{d\hat{N}}{dt} + \mathbf{u} \cdot \nabla \hat{N} + f(\hat{N}) = 0$$

where $f(\hat{N}) = \frac{1}{2}b(\dot{\gamma})(\hat{N} - \hat{N}_{st})(\hat{N} + \hat{N}_{st} - 1)$ is the reaction term.

Discretizing in space gives (we assume a Galerkin method here for simplifying notation):

$$\langle \frac{d\hat{N}_h}{dt} + \mathbf{u} \cdot \nabla \hat{N}_h + f(\hat{N}_h), \phi_{\hat{N}} \rangle = 0; \quad \forall \phi_{\hat{N}} \in \mathcal{N}_{test,h}$$

Finally we discretize in time using an Euler implicit method. Given an initial condition, $\hat{N}_h|_{t=0} = \hat{N}^{\{0\}}$, we solve :

$$\langle \frac{\hat{N}_h^{\{n\}} - \hat{N}_h^{\{n-1\}}}{\Delta t} + \mathbf{u} \cdot \nabla \hat{N}_h^{\{n\}} + f(\hat{N}_h^{\{n\}}), \phi_{\hat{N}} \rangle = 0; \quad \forall \phi_{\hat{N}} \in \mathcal{N}_{test,h}$$

for $\hat{N}_h^{\{n\}}$ at all times $t_n = n\Delta t, n = 1, 2, 3, \dots$

The final issue is how to linearize, the nonlinear reaction term, f . The standard approach is to apply Newton's method and solve iteratively at each time, t_n the following system until convergence:

$$\left\langle \frac{\hat{N}_h^{\{n,k\}} - \hat{N}_h^{\{n-1\}}}{\Delta t}, \phi_{\hat{N}} \right\rangle + \left\langle \frac{\partial f(\hat{N}_h^{\{n,k-1\}})}{\partial \hat{N}} \hat{N}_h^{n,k}, \phi_{\hat{N}} \right\rangle = 0; \quad \forall \phi_{\hat{N}} \in \mathcal{N}_h$$

where k indexes the successive iterates of Newton's method. We have chosen instead to do something else. Instead of evaluating both terms that appear in the expression for f we evaluate only one and use the already calculated value from the previous time step. That is we approximate

$$f(\hat{N}_h^{\{n\}}) = \frac{1}{2} \mathbf{b}(\dot{\gamma})(\hat{N}_h^{\{n\}} - \hat{N}_{st}^{\{n\}})(\hat{N}_h^{\{n\}} + \hat{N}_{st}^{\{n\}} - 1)$$

by

$$f(\hat{N}_h^{\{n\}}) = \frac{1}{2} \mathbf{b}(\dot{\gamma})(\hat{N}_h^{\{n\}} - \hat{N}_{st}^{\{n\}})(\hat{N}_h^{\{n-1\}} + \hat{N}_{st}^{\{n\}} - 1)$$

This makes f linear in $\hat{N}_h^{\{n\}}$ and completes both the space and time discretization.

The discretization for the other time operators is very similar and we simply state the equations in the next section.

2.4 The Weak System

We now state in full the discrete system to be solved.

Let \mathcal{M}_h be a tessellation on Ω . Let $\mathcal{U}_h = \{\mathbf{u}_h \in \mathbb{R}^3 | \mathbf{u}_h \in P_2\}$, let $\mathcal{P}_h = \{p_h \in \mathbb{R} | p_h \in P_1\}$, let $\mathcal{N}_h = \{\hat{N}_h \in \mathbb{R} | \hat{N}_h \in P_1\}$, let $\mathcal{T}_h = \{\boldsymbol{\tau}_h \in \mathbb{R}^{3 \times 3, sym} | \boldsymbol{\tau}_h \in P_1\}$, and let $\mathcal{D}_h = \mathcal{T}_h$.

Note that the tensor fields \mathcal{T}_h and \mathcal{D}_h are specified to contain symmetric tensors.

Then, given initial values, $(\mathbf{u}_h^0, p_h^0, \hat{N}_h^0, \boldsymbol{\tau}_h^0, \mathbf{d}_h^0)$ at $t = 0$ we seek iteratively at each time $t_n = n\Delta t, n = 1, 2, 3, \dots$, a quintuplet $(\mathbf{u}_h^n, p_h^n, \hat{N}_h^n, \boldsymbol{\tau}_h^n, \mathbf{d}_h^n) \in (\mathcal{U}_h \times \mathcal{P}_h \times \mathcal{N}_h \times \mathcal{T}_h \times \mathcal{D}_h)$ such that:

$$\begin{aligned} \text{Re} \left\langle \frac{(\mathbf{u}_h^n - \mathbf{u}_h^{n-1})}{\Delta t}, \phi_{\mathbf{u}} \right\rangle + \text{Re} \, c(\mathbf{u}_h^n, \mathbf{u}_h^n, \phi_{\mathbf{u}}) + \\ b(p_h^n, \phi_{\mathbf{u}}) + (\alpha + 2\eta_s)a(\mathbf{u}_h^n, \phi_{\mathbf{u}}) = \end{aligned} \quad (2.4.1)$$

$$\begin{aligned} \langle \nabla \cdot \boldsymbol{\tau}_h^n, \phi_{\mathbf{u}} \rangle + \alpha \langle \mathbf{d}_h^n, \nabla \phi_{\mathbf{u}} \rangle; \quad \forall \phi_{\mathbf{u}} \in \mathcal{U}_{test,h}, \\ b(\mathbf{u}_h^n, \phi_p) + \epsilon_h \langle p_h^n, \phi_p \rangle = 0; \quad \forall \phi_p \in \mathcal{P}_{test,h}, \end{aligned} \quad (2.4.2)$$

$$\langle \mathbf{d}_h^n, \phi_{\mathbf{d}} \rangle = \langle \dot{\boldsymbol{\gamma}}(\mathbf{u}_h^n), \phi_{\mathbf{d}} \rangle \quad \forall \phi_{\mathbf{d}} \in \mathcal{D}_{test,h}, \quad (2.4.3)$$

$$\begin{aligned} \left\langle \frac{\hat{N}_h^n - \hat{N}_h^{n-1}}{\Delta t}, \phi_{\hat{N}} \right\rangle + c(\mathbf{u}_h^n, \hat{N}_h^n, \phi_{\hat{N}}) + \\ \left\langle \frac{1}{2} \mathbf{b}(\dot{\boldsymbol{\gamma}}^n)(\hat{N}_h^{n-1} + \hat{N}_{st}(\dot{\boldsymbol{\gamma}}^n) - 1) \hat{N}_h^n, \phi_{\hat{N}} \right\rangle = \end{aligned} \quad (2.4.4)$$

$$\begin{aligned} \left\langle \frac{1}{2} \mathbf{b}(\dot{\boldsymbol{\gamma}}^n)(\hat{N}_h^{n-1} + \hat{N}_{st}(\dot{\boldsymbol{\gamma}}^n) - 1) \hat{N}_{st}(\dot{\boldsymbol{\gamma}}^n), \phi_{\hat{N}} \right\rangle \quad \forall \phi_{\hat{N}} \in \mathcal{N}_{test,h}, \\ \langle \boldsymbol{\tau}_h^n, \phi_{\boldsymbol{\tau}} \rangle + \langle \text{De}(\hat{N}_h^n) \left(\frac{\boldsymbol{\tau}_h^n - \boldsymbol{\tau}_h^{n-1}}{\Delta t} + (\mathbf{u}_h^n \cdot \nabla) \boldsymbol{\tau}_h^n - \right. \\ \left. \nabla \mathbf{u}_h^n \cdot \boldsymbol{\tau}_h^n - \boldsymbol{\tau}_h^n \cdot \nabla \mathbf{u}_h^n \right), \phi_{\boldsymbol{\tau}} \rangle = \\ \langle \text{De} \dot{\boldsymbol{\gamma}}(\mathbf{u}_h^n), \phi_{\boldsymbol{\tau}} \rangle \quad \forall \phi_{\boldsymbol{\tau}} \in \mathcal{T}_{test,h}, \end{aligned} \quad (2.4.5)$$

For readability we will henceforth drop the h subscript from the variables.

2.4.1 Picard Iteration

The system of equations (2.4.1) - (2.4.5) is tightly coupled and highly non-linear, for one when considering all the places the shear-rate $\dot{\boldsymbol{\gamma}}(\mathbf{u})$ comes up in the microstructure equation (2.4.4) and also due to the terms $\nabla \mathbf{u} \cdot \boldsymbol{\tau}$ and $\mathbf{u} \cdot \nabla \mathbf{u}$. The Deborah number itself, De is a rather complicated function of \hat{N} and $\dot{\boldsymbol{\gamma}}$. Therefore before the application of dedicated linear solvers, one must linearize the system. There are two main techniques for this, commonly called Picard iteration and Newton's method. Picard iteration solves one of the five equations at a time and loops over the equations until convergence of the unknowns, before stepping forward in time. Newton's method is based on linearizing the system all at once. A discussion of both methods

in the context of viscoelastic flows is given in Sec. 6.2 of [21].

For our purposes, we use a Picard-type iteration at each time-step to solve the system of equations (2.4.1) - (2.4.5). We first solve the momentum and continuity equations simultaneously (2.4.1) - (2.4.2), then we perform the discrete strain projection (2.4.3) using the newly obtained $\dot{\gamma}(\mathbf{u})$, then the advection-reaction equation, Eq. (2.4.4), is solved for \hat{N} using the newly obtained \mathbf{u} and $\dot{\gamma}$ and finally the constitutive equation, (2.4.5), is solved using the newly obtained $\text{De}(\hat{N})$. This cycle continues until some threshold of convergence. More precisely, at any fixed time $t_n = n\Delta t$, we perform an inner loop over the Picard indices $k = 1, 2, \dots, k_{max}$, and at each Picard step, k , we will look for a quintuplet $(\mathbf{u}^{n,k}, p^{n,k}, \hat{N}^{n,k}, \boldsymbol{\tau}^{n,k}, \mathbf{d}^{n,k})$ using the initial values $(\mathbf{u}^{n,0}, p^{n,0}, \hat{N}^{n,0}, \boldsymbol{\tau}^{n,0}, \mathbf{d}^{n,0}) = (\mathbf{u}^{n-1}, p^{n-1}, \hat{N}^{n-1}, \boldsymbol{\tau}^{n-1}, \mathbf{d}^{n-1})$ - the solution of the previous time-step. The system of equations is presented in the order in which the individual equations are solved:

$$\begin{aligned} \text{Re} \left\langle \frac{\mathbf{u}^{n,k} - \mathbf{u}^{n-1}}{\Delta t}, \phi_{\mathbf{u}} \right\rangle + \text{Re} \, c(\mathbf{u}^{n,k}, \mathbf{u}^{n,k}, \phi_{\mathbf{u}}) + \\ b(p^{n,k}, \phi_{\mathbf{u}}) + (\alpha + 2\eta_s)a(\mathbf{u}^{n,k}, \phi_{\mathbf{u}}) = \end{aligned} \quad (2.4.6)$$

$$\left\langle \nabla \cdot \boldsymbol{\tau}^{n,k-1}, \phi_{\mathbf{u}} \right\rangle + \alpha \left\langle \mathbf{d}^{n,k-1}, \nabla \phi_{\mathbf{u}} \right\rangle; \quad \forall \phi_{\mathbf{u}} \in \mathcal{U}_{test,h},$$

$$b(\mathbf{u}^{n,k}, \phi_p) + \epsilon \left\langle p^{n,k}, \phi_p \right\rangle = 0; \quad \forall \phi_p \in \mathcal{P}_{test,h}, \quad (2.4.7)$$

$$\left\langle \mathbf{d}^{n,k}, \phi_{\mathbf{d}} \right\rangle = \left\langle \dot{\gamma}(\mathbf{u}^{n,k}), \phi_{\mathbf{d}} \right\rangle \quad \forall \phi_{\mathbf{d}} \in \mathcal{D}_{test,h}, \quad (2.4.8)$$

$$\begin{aligned} & \left\langle \frac{\hat{N}^{n,k} - \hat{N}^{n-1}}{\Delta t}, \phi_{\hat{N}} \right\rangle + c(\mathbf{u}^{n,k}, \hat{N}^{n,k}, \phi_{\hat{N}}) + \\ & \left\langle \frac{1}{2} \mathbf{b}(\dot{\gamma}^{n,k})(\hat{N}^{n-1} + \hat{N}_{st}(\dot{\gamma}^{n,k}) - 1) \hat{N}^{n,k}, \phi_{\hat{N}} \right\rangle = \end{aligned} \quad (2.4.9)$$

$$\left\langle \frac{1}{2} \mathbf{b}(\dot{\gamma}^{n,k})(\hat{N}^{n-1} + \hat{N}_{st}(\dot{\gamma}^{n,k}) - 1) \hat{N}_{st}(\dot{\gamma}^{n,k}), \phi_{\hat{N}} \right\rangle \quad \forall \phi_{\hat{N}} \in \mathcal{N}_{test,h},$$

$$\begin{aligned} \left\langle \boldsymbol{\tau}^{n,k}, \phi_{\boldsymbol{\tau}} \right\rangle + \left\langle \text{De}(\hat{N}^{n,k}) \left(\frac{\boldsymbol{\tau}^{n,k} - \boldsymbol{\tau}^{n-1}}{\Delta t} + (\mathbf{u}^{n,k} \cdot \nabla) \boldsymbol{\tau}^{n,k} - \right. \right. \\ \left. \left. \nabla \mathbf{u}^{n,k} \cdot \boldsymbol{\tau}^{n,k} - \boldsymbol{\tau}^{n,k} \cdot \nabla \mathbf{u}^{n,k} \right), \phi_{\boldsymbol{\tau}} \right\rangle = \end{aligned} \quad (2.4.10)$$

$$\left\langle \text{De} \dot{\gamma}(\mathbf{u}^{n,k}), \phi_{\boldsymbol{\tau}} \right\rangle \quad \forall \phi_{\boldsymbol{\tau}} \in \mathcal{T}_{test,h},$$

Note that we will use a newly computed solution for a quantity (say \mathbf{u} in Eq. (2.4.10)) as soon as it is available from the same Picard iteration, rather than wait until the next iteration. This is analogous to using the Gauss-Seidel method for the iterative solution of a linear system vs. the Jacobi method.

We have chosen for our Picard iteration convergence criterion, the max norm of the incremental difference in the discrete vectors representing the variables $(\mathbf{u}, \hat{N}, \boldsymbol{\tau})$. Letting U represent the coefficients of $\{\phi_{\mathbf{u},i}\}$ in the solution for \mathbf{u}^k , the system is considered resolved if $\|U^k - U^{k-1}\|_\infty < \epsilon_{picard}$ and similarly for $\boldsymbol{\tau}^k$ and \hat{N}^k . We have set $\epsilon_{picard} = 1e - 5$.

Once decoupled in this manner, the system retains only one non-linearity, the advection term $\mathbf{u} \cdot \nabla \mathbf{u}$ in (2.4.6). To deal with it, we linearize and solve it using Newton's method at each Picard iteration. This is a standard technique in the finite elements treatment of the Navier-Stokes equations that will not be discussed here.

2.5 MEF++

The C++-based finite element code MEF++ ([5]) is developed under le Groupe Interdisciplinaire de Recherche en Éléments Finis (GIREF) at l'Université Laval. It has an object-oriented design that allows for adding arbitrary terms in a PDE. It links to the Portable Extensible Toolkit for Scientific Computations (PETSc) library ([1]) for the solution of the resulting linear system. All finite element calculations presented have been performed using the MEF++ suite of libraries.

Chapter 3

Numerical Experiments

This chapter is about the validation of our numerical scheme and a series of computational experiments inside a 2D geometry that have not been previously performed with this rheological model. In the first section we discuss results in a coaxial rheometer where we duplicate some results from the original paper of Owens [20]. In the second section we perform several experiments in a channel, which is a geometry often used to validate the numerical schemes for Oldroyd-B and related models. We also determine the apparent viscosity of an equivalent Newtonian fluid. In the final section we discuss new results obtained in a dilated channel under steady and, more interestingly, pulsatile flow conditions. In particular we compare the results of the viscoelastic model against the behaviour of a Newtonian fluid given the same flow set-up.

Note that throughout the three sections there are several discussions about the major numerical techniques used in this paper. In particular why we need DEVSS is quickly discussed in Sec. 3.2.2, while a deleterious effect of not using SUPG is pointed out in Sec. 3.3.4.

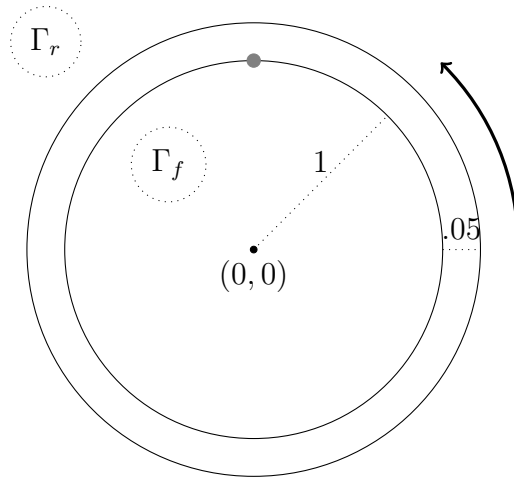


Figure 3.1: *Flow in a coaxial rheometer - geometry and boundary conditions. See text for details.*

3.1 Coaxial Rheometer

The original paper of Owens [20] replicates results in a coaxial rheometer of Bureau et al. [4]. The geometrical set-up for this problem is illustrated in Fig. 3.1. A coaxial rheometer consists of two concentric cylinders separated by a narrow gap. Also called a viscometer, it is used primarily for measuring the shear-dependence of a fluid's viscosity. In the experiment, the inner cylinder is held fixed, while the outer cylinder is accelerated for time $t \in [0, t_f/2]$ and then decelerated over $t \in [t_f/2, t_f]$. Experimentally this can be done such that the shear-rate $\dot{\gamma}$ is a piecewise-linear function of time, as in see Fig. 3.2, increasing from $[0, \dot{\gamma}_{max}]$ and then decreasing to 0, and such that $\dot{\gamma}$ is almost independent of space. Experimentally, the shear-stress, $\tau_{r\theta}$, can be inferred by measuring the torque on the inner wall. In our numerical experiments this is represented as follows (refer to Fig. 3.1): Γ_r is the outer, rotating wall and Γ_f is the inner, fixed wall. At both locations, we impose no-slip on \mathbf{u} , i.e. \mathbf{u} rotates with Γ_r and is fixed at Γ_f . Since the flow does not enter or leave the geometry, no boundary conditions need to be imposed on \hat{N} or $\boldsymbol{\tau}$.

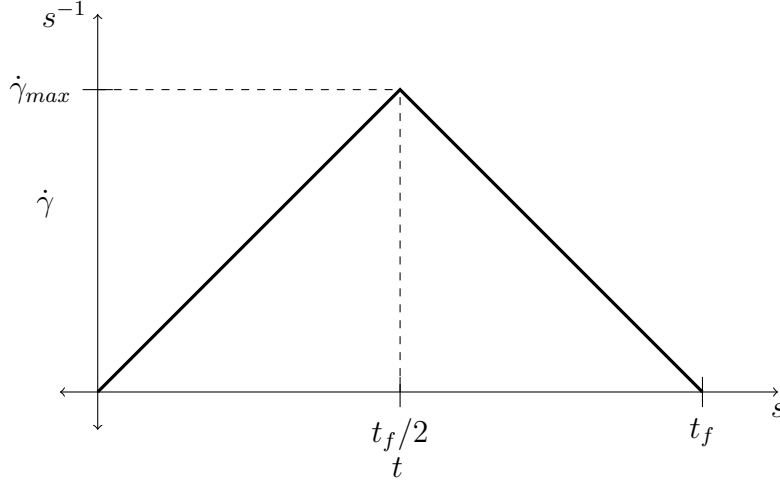


Figure 3.2: *Functional form of the applied shear rate, $\dot{\gamma}(t)$, for the coaxial rheometer experiment.*

3.1.1 Imposed Velocity

If we take the flow as imposed, i.e that \mathbf{u} is known on the geometry such that $\nabla \mathbf{u}$ is constant then the solution for \hat{N} and $\boldsymbol{\tau}$ will also be uniform in space. More specifically, given the geometry dimensionalized as in Fig. 3.1 and a piecewise-linear $\dot{\gamma}(t)$ as in Fig. 3.2, then the velocity is assumed to be a radial function everywhere on the domain, which in polar coordinates is:

$$u_r = 0 \quad (3.1.1)$$

$$u_\theta = \dot{\gamma}(t) r \log r \quad (3.1.2)$$

The shear-rate $\dot{\gamma}$ and the deformation-rate tensor $\dot{\boldsymbol{\gamma}}$ are then uniform in space implying that so should \hat{N} and $\boldsymbol{\tau}$. Therefore the entire problem reduces to a system of coupled ODE's in time, which looks as follows:.

$$\frac{d\hat{N}}{dt} = -\mathbf{b}(\dot{\boldsymbol{\gamma}})(\hat{N} - \hat{N}_{st})(\hat{N} + \hat{N}_{st} - 1) \quad (3.1.3)$$

$$\frac{d\tau_{r\theta}}{dt} = \frac{\text{De}(\hat{N})\dot{\boldsymbol{\gamma}}(t) - \tau_{r\theta}}{\text{De}(\hat{N})} \quad (3.1.4)$$

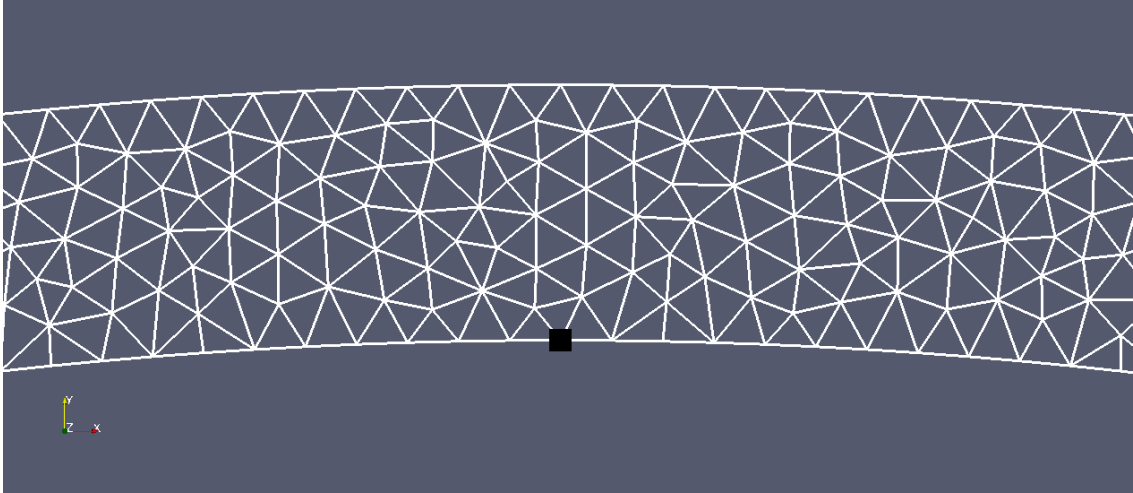


Figure 3.3: *Close-up of the mesh for the coaxial rheometer experiment.*

Such a system can be solved in any numerical package such as Matlab. This is the first step we take so that we can use the results from the ODE's calculations for comparison with our finite element (FE) calculations from the 2D coaxial rheometer geometry. This will also serve as an illustration of the behaviour of the various non-constant parameters in the system as functions of the shear rate, $\dot{\gamma}$ (see Fig. 3.4).

Three different test cases are shown matching what is in the original paper by Owens, [20]. The difference between the three cases is the maximum value of the shear-rate, $\dot{\gamma}_{max}$, at the experiment's midtime, $t_f/2$. The three values are $\dot{\gamma}_{max} = 0.1, 0.29, 0.84s^{-1}$. For all three experiments we have $t_f = 40s$. Table 3.1 shows the parameter values used in the coaxial rheometer simulations. Figure 3.5 shows the results for \hat{N} and $\tau_{r\theta}$ obtained by solving the ODE's in Matlab. As is done in [20], the values of the variables during the second portion of the experiment (when shear is decreasing) are plotted on top of the values from the first portion. This highlights the hysteresis in the evolution of $\tau_{r\theta}$.

In order to validate our finite element code, we seek to match the results in

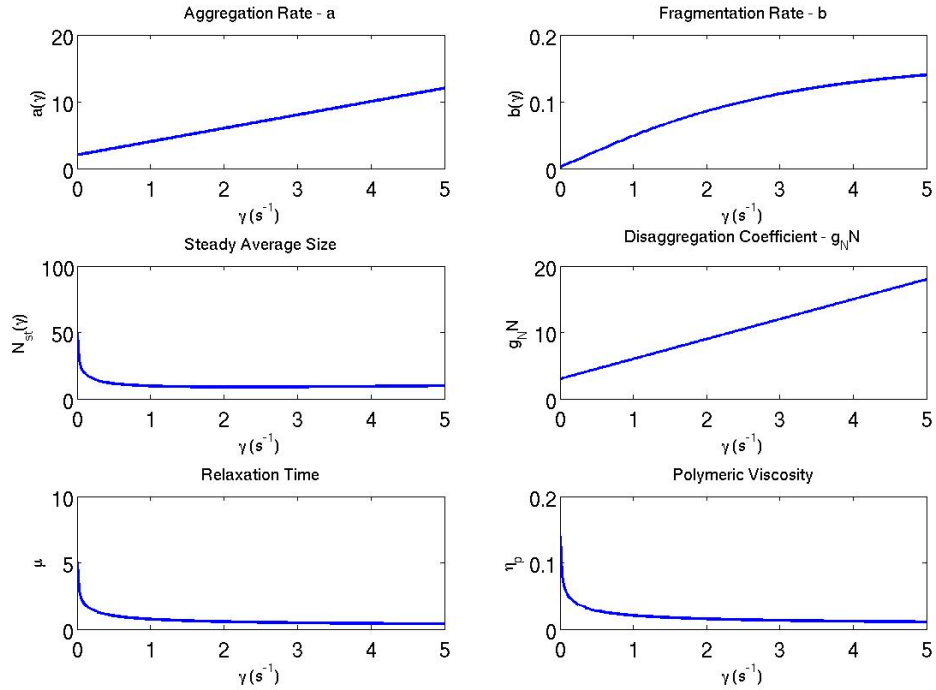


Figure 3.4: *Graphs of model parameters as functions of $\dot{\gamma}$. Going left-to-right, top-to-bottom, they are the aggregation rate, $\mathbf{a}(\dot{\gamma})$, the fragmentation rate, $\mathbf{b}(\dot{\gamma})$, the steady average rouleaux size, \hat{N}_{st} , the disaggregation coefficient, $g_{\hat{N}_{st}}$, the dumbbell relaxation time μ , and the polymeric viscosity, η_p . Note that some of these quantities are functions of both $\dot{\gamma}$ and \hat{N} . In such a case we set $\hat{N} = \hat{N}_{st}$. Refer to Ch. 1 for their physical meaning and algebraic form. For details see [20] and [17].*

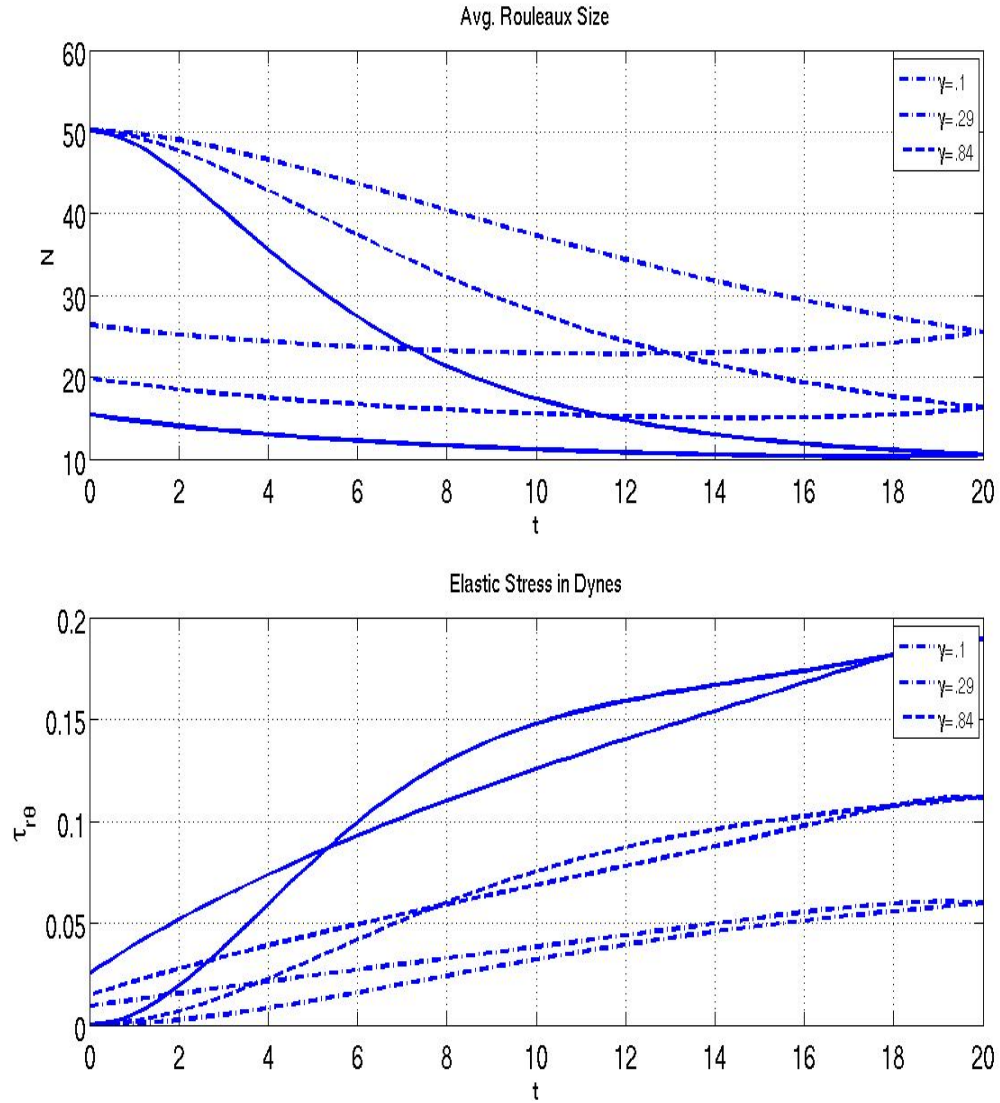


Figure 3.5: Time plot of the solution \hat{N} (at top) and $\tau_{r\theta}$ (at bottom) for $\dot{\gamma}_{max} = 0.1, 0.29, 0.84$. All solutions are plotted from $\hat{N}(0) = 50$ and $\tau_{r\theta}(0) = 0$ over $t \in [0, t_f/2]$ for increasing $\dot{\gamma}$ and over $t \in [t_f, t_f/2]$ for decreasing $\dot{\gamma}$.

parameter	value	comments, (units)
η_0	0.14	zero-shear polymeric viscosity, ($kg\ s^{-1}m^{-1}$)
η_∞	0.004	infinite-shear polymeric viscosity, ($kg\ s^{-1}m^{-1}$)
β	7.2	Cross model coefficient
m	.6	Cross model exponent
λ_H	0.145	single cell relaxation time, (s)
η_N	.001	plasma (Newtonian) viscosity, ($kg\ s^{-1}m^{-1}$)
ρ_f	1053.6	plasma fluid density, ($kg\ m^{-3}$)

Table 3.1: *Parameter values for the coaxial rheometer test case. The model's parameters used for the numerical experiment in the coaxials rheometer geometry. For the coefficients in the functional form for $\mathbf{a}(\dot{\gamma})$ we have used the values as in [20]*

Fig. 3.5. Since our model is implemented in dimensionless units one needs to keep track of the corresponding dimensional units in the experiment. However since the triangular-ramp shear-rate experiment is characterized by the dimensional values of the shear-rate, it is not really important what the characteristic length and velocity scales are, as long as the corresponding dimensional shear-rate is the same as in [20]. For our characteristic scales we set $U_{char} = 0.0229$, $L_{char} = 0.0066$. In order to measure $\tau_{r\theta}$ from a Cartesian coordinate system, which is what we employ for our FE calculations, we probe τ_{xy} at the top of the inner cylinder, $(x, y) = (0, 1)$. For this point $\tau_{r\theta} = \tau_{xy}$. Figure 3.3 shows a closeup of the mesh used and the point (thick grey dot) where τ_{xy} and \hat{N} are measured for comparison with the solutions of the ODE's shown in Fig. 3.5. The measurement point is also marked on Fig. 3.1.

This somewhat coarse mesh has 4320 vertices and 7356 elements, which leaves about 5-6 elements across the gap. We take $\Delta t = 0.1U_{char}/L_{char}$, i.e. 400 time steps are done for the entire FE simulation. This is of the same order of magnitude as the time step taken by the Matlab ODE solvers (though of course Matlab employs methods with a higher order of convergence in time.) The FE solutions can be seen in Fig.3.6 plotted on the same graph as the Matlab solution. The ODE and FE solutions are almost identical, the maximum difference being about 1%. Finally we

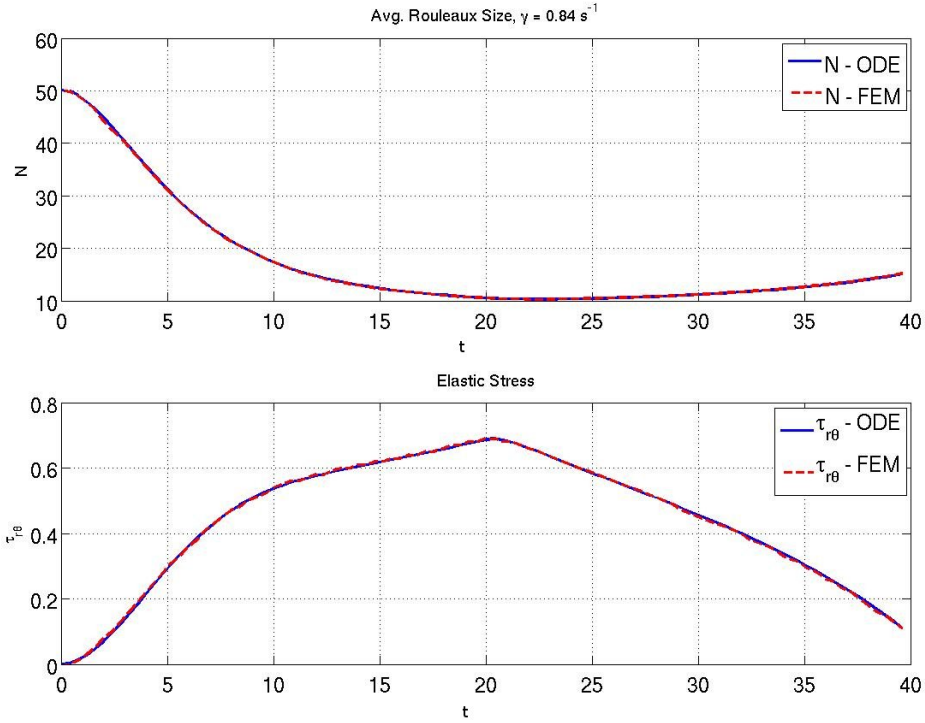


Figure 3.6: Comparison of Matlab and FE numerical solutions. Time-history of \hat{N} (at top) and $\tau_{r\theta}$ (at bottom). Results obtained from Matlab (i.e. from the ODE's) are in blue, the finite element results are in red. These are solutions for $\hat{\gamma}_{max} = 0.84s^{-1}$ and the velocity given in Eq. (3.1.1).

look at the distribution of \hat{N} and $\boldsymbol{\tau}$ in space, which should be constant. We find this to be indeed the case when we take a look at surface plots of both variables in Fig. 3.7. The spatial variation in the variables is on the order of less than .2% for $|\boldsymbol{\tau}|_{Frob}$ and less than .001% for \hat{N} .

3.1.2 Resolution of Fully Coupled System

The next test case is to attempt to solve the fully coupled problem, Eqs. (2.4.1)-(2.4.5). For the boundary conditions on \mathbf{u} , we set $\mathbf{u}|_{\Gamma_f} = 0$ on the fixed wall and we

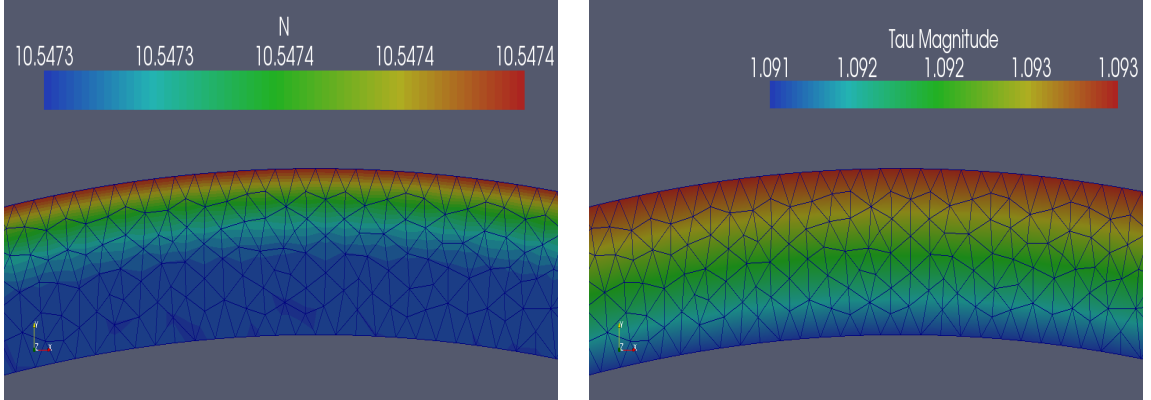


Figure 3.7: *Surface plots of \hat{N} and $|\boldsymbol{\tau}|_{F_{rob}}$ in the coaxial rheometer. \hat{N} (left) and $|\boldsymbol{\tau}|_{F_{rob}}$ (right) at the midtime, $t_f/2$ of the triangular-ramp shear experiment assuming the given velocity, Eq. (3.1.1). Noting the scale, there is almost no cross-sectional variation.*

prescribe an accelerating rotation at Γ_r :

$$u_r|_{\Gamma_r} = 0 \quad (3.1.5)$$

$$u_\theta|_{\Gamma_r} = \dot{\gamma}(t) R \log(R) \quad (3.1.6)$$

where $R = 1.05$ is the radius of the outer wall and $\dot{\gamma}(t)$ has exactly the same form as in Fig. 3.2. Using the same mesh, the results from the fully coupled problem can be seen in Fig. 3.8, where we have also included the results from the uncoupled simulation for comparison.

It is immediately clear that the shape and scale are very similar. In fact whatever discrepancy between values coming from the coupled vs. the non-coupled solutions can be explained by the fact that the shear-rate is no longer radially constant in the fully coupled problem. Instead, in the fully coupled problem, the shear rate is a radially decreasing function, such that near Γ_f it is slightly higher than the imposed value from the non-coupled case. Thus if near the wall, $\dot{\gamma}$ is larger, we would expect $\tau_{r\theta}$ to be also larger and \hat{N} to be slightly smaller. This is indeed what is observed in Fig. 3.8.

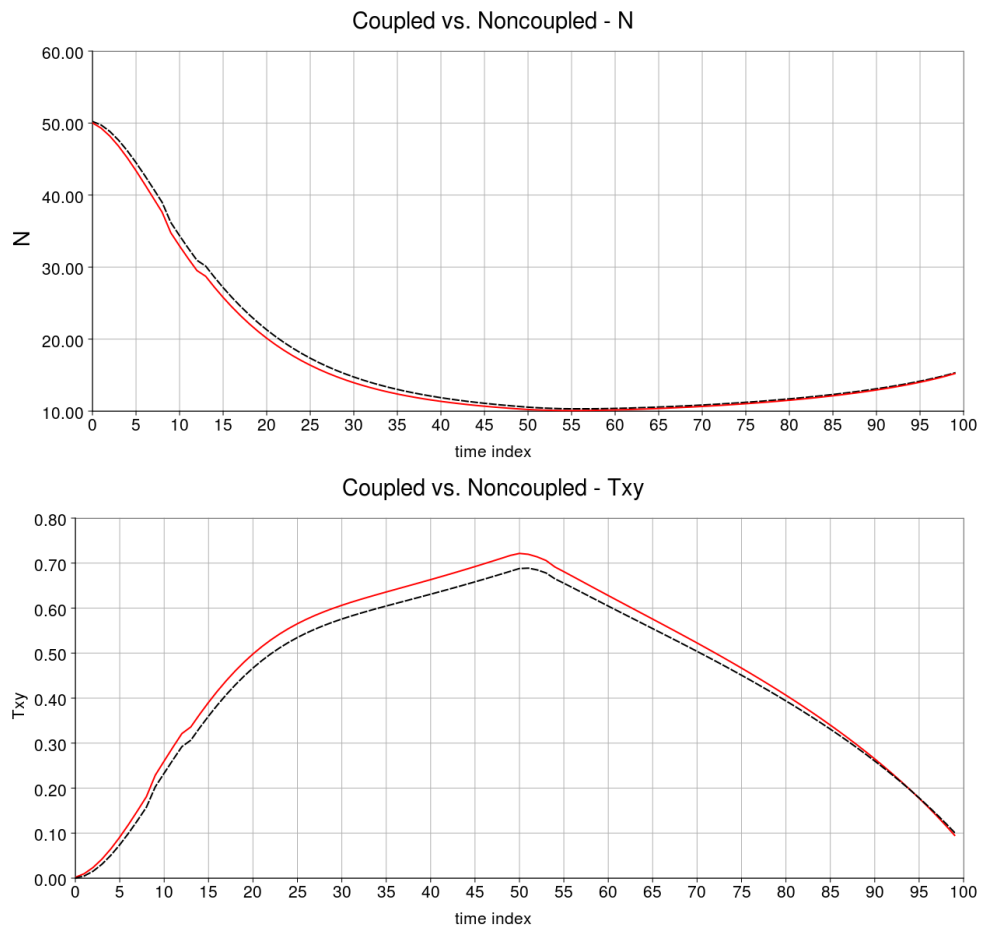


Figure 3.8: Comparison of coupled vs. uncoupled solutions. Time-history of \hat{N} (at top) and $\tau_{r\theta}$ (at bottom). Results obtained from the uncoupled problem are in black, results from the fully coupled problem are in red. $\dot{\gamma}_{max} = 0.84s^{-1}$

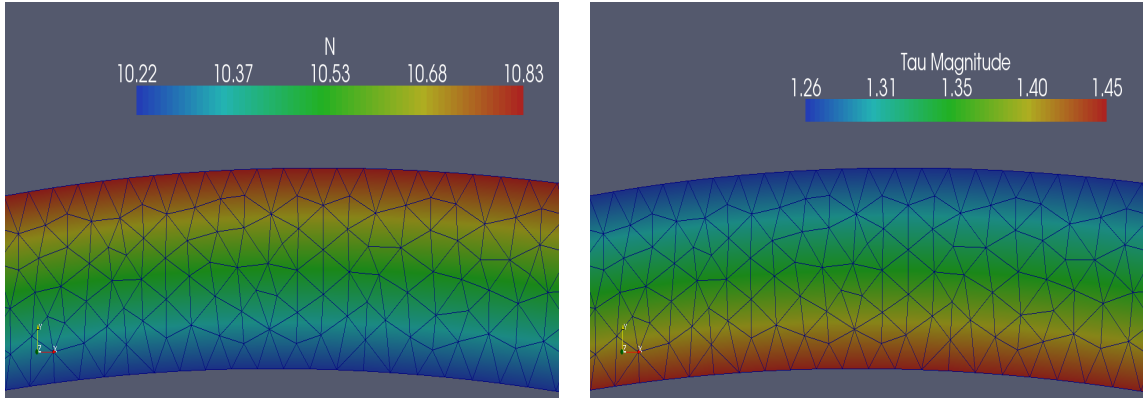


Figure 3.9: *Surface plots of \hat{N} and $|\boldsymbol{\tau}|_{Frob}$ in the coaxial rheometer for the coupled problem. \hat{N} (left) and $|\boldsymbol{\tau}|_{Frob}$ (right) at the midtime, $t_f/2$ of the triangular-ramp shear experiment after solving the complete problem*

Note further that the radial variation in the shear-rate induces a variation in \hat{N} as well as $\boldsymbol{\tau}$ (see Fig. 3.9).

In summary we feel satisfied that our code correctly represents the model at least in this geometry and we have seen the first example of the complete coupling between all the variables in 2D. Now we can proceed to the main type of experiments we want to perform, viz. flow in channels.

3.2 Flows in a Straight Channel

Since blood vessels have a tubular, pipe-like shape, it makes sense to explore this rheological model in pipe-like or, in the 2D case, channel geometries. A straight channel allows for further testing of our numerical scheme and it gives us a convenient test-bed for determining the value of the viscosity in an 'equivalent' Newtonian fluid, which is done in Sec. 3.2.5.

Table 3.2 shows the parameter values used in experiments in channel-type ge-

Parameter	Value	Comments
η_0	0.0326	zero-shear polymeric viscosity, ($kg\ s^{-1}m^{-1}$)
η_∞	0.0030	infinite-shear polymeric viscosity, ($kg\ s^{-1}m^{-1}$)
β	1.0	Cross model coefficient
m	1	Cross model exponent
λ_H	0.005	single cell relaxation time, (s)
η_N	.001	plasma (Newtonian) viscosity, ($kg\ s^{-1}m^{-1}$)
ρ_f	1053.6	plasma fluid density, ($kg\ m^{-3}$)

Table 3.2: *Parameter values for the channel test cases. The model's parameters used for the numerical experiment in the channel geometries. For the coefficients in the functional form for $\mathbf{a}(\dot{\gamma})$ we have used the values as in [8]*

ometries for both straight and dilated channels in all numerical simulations in both this and the next sections. The values have been taken from the later papers of Owens et al. [17], [8].

3.2.1 Geometry and Boundary Conditions for Flow in a Straight Channel

Consider the problem illustrated in Fig. 3.10, which we term flow in a straight channel. Our domain is simply a rectangle of length 5 and width 1. The flow goes from left to right, entering the domain at the inlet, Γ_i , and exiting at the outlet, Γ_o . At Γ_i we impose values for all \mathbf{u} , $\boldsymbol{\tau}$ and \hat{N} . At Γ_o we set $u_y = 0$ and the natural outflow condition, $-p + 2\eta_s\partial_x u_x = 0$. Along both walls, Γ_w , we put no-slip condition on the velocity, $\mathbf{u} = \mathbf{0}$.

The simplest such flow is a steady, shear flow such that $\mathbf{u} = (u_x(y), 0)^T$, for any function $u_x = u_x(y)$. If so, then the solution for the microstructure equation, (1.5.12) and the extra stress equations (1.5.13) is given by:

$$\begin{aligned}\hat{N} &= \hat{N}_{st}(|\partial_y u_x|) \\ \tau_{xx} &= 2\text{De}^2(\hat{N}_{st})(\partial_y u_x)^2\end{aligned}\tag{3.2.1}$$

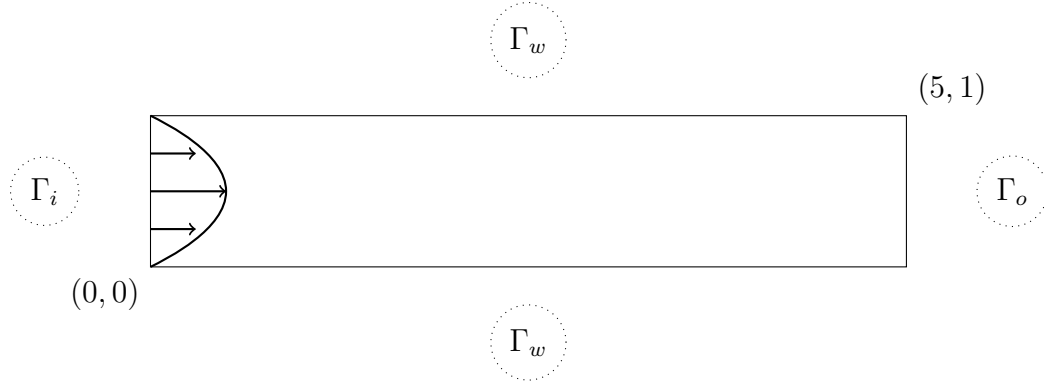


Figure 3.10: *Flow in a straight channel - geometry and boundary conditions. See text for details.*

$$\begin{aligned}\tau_{xy} &= \text{De}(\hat{N}_{st}) \partial_y u_x \\ \tau_{yy} &= 0\end{aligned}$$

as long as we add the following right-hand function, \mathbf{f} to the momentum equation, (1.5.10).

$$\mathbf{f} = \left[-(\text{De} + \eta_s) \frac{\partial^2 u_x}{\partial y^2} - \frac{\partial \text{De}}{\partial y} \frac{\partial u_x}{\partial y}, 0 \right]^T \quad (3.2.2)$$

i.e Eq. (1.5.10) becomes

$$\text{Re} \frac{D\mathbf{u}}{Dt} - 2\eta_s \nabla \cdot \dot{\gamma} - \nabla \cdot \boldsymbol{\tau} + \nabla p = \mathbf{f} \quad (3.2.3)$$

3.2.2 Steady Flow Experiment

We choose a mesh with 4482 elements, mesh X1 in Tab. 3.4. The mesh is shown in Fig. 3.11. The black, vertical line across in Fig. 3.11 indicates a cut along which we later plot our variables. With this mesh we have about 20 elements across the width of the channel. For this test case, we set the inflow to be a quadratic, $u_x(y)|_{\Gamma_i} = 4(1-y)y$, and we apply the expressions from Eq. 3.2.1 as both inlet BC's and initial conditions. However evaluating the derivative $\frac{\partial \text{De}}{\partial y}$ is a cumbersome and error-prone task and so we instead simply set $f_x = -(\text{De} + \eta_s) \frac{\partial^2 u_x}{\partial y^2}|_{\Gamma_i} = 8(\text{De} + \eta_s)$. The values for the Reynolds

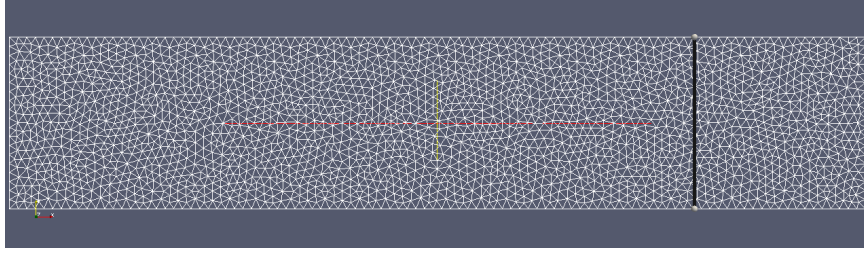


Figure 3.11: *Mesh X1 for the straight channel.*

and the infinite-shear Deborah numbers are $\text{Re} = 25.45$ and $\text{De}_\infty = 0.1$. Surface plots for the solutions over the entire domain are shown in Fig. 3.12. In Fig. 3.13 we plot cuts of the variables along a vertical line at $x = 4$. Note that we are solving the fully coupled problem such that $\text{De} = \text{De}(\hat{N})$ and thus given our simplified form for \mathbf{f} , Eq. 3.2.1 is not a solution (except of course that $\hat{N} = \hat{N}_{st}$). Nevertheless to a large extent the variables behave as in Eq. 3.2.1. With the shear-rate, $\dot{\gamma}$ increasing linearly from the midline of the channel, \hat{N} has a bell-like profile centred at the midline. This has the effect of reducing De near the walls and thus tempering the growth of τ_{xx} and τ_{xy} near the walls.

Remark 3.2.1 Using the same parameters we tried to perform our simulations without using the DEVSS technique, i.e. setting $\alpha = 0$ in Eq. (2.4.1) and ignoring the \mathbf{d} variable altogether. However we found that we could no longer obtain convergent solutions.

3.2.3 Numerical Validation - Steady Shear Flows

In order to validate our schemes we compare the results from our FE code to the analytical solutions in Eq. 3.2.1. Since we need to evaluate the y -partial derivative of De , $\frac{\partial \text{De}}{\partial y}$ in the expression for f_x , Eq. 3.2.2, we will simplify the expression of De in order to simplify calculations. We compute two different flows as test cases with two different expressions for De . For our first new test case we set $\text{De} = \text{De}_{const} = 0.137$

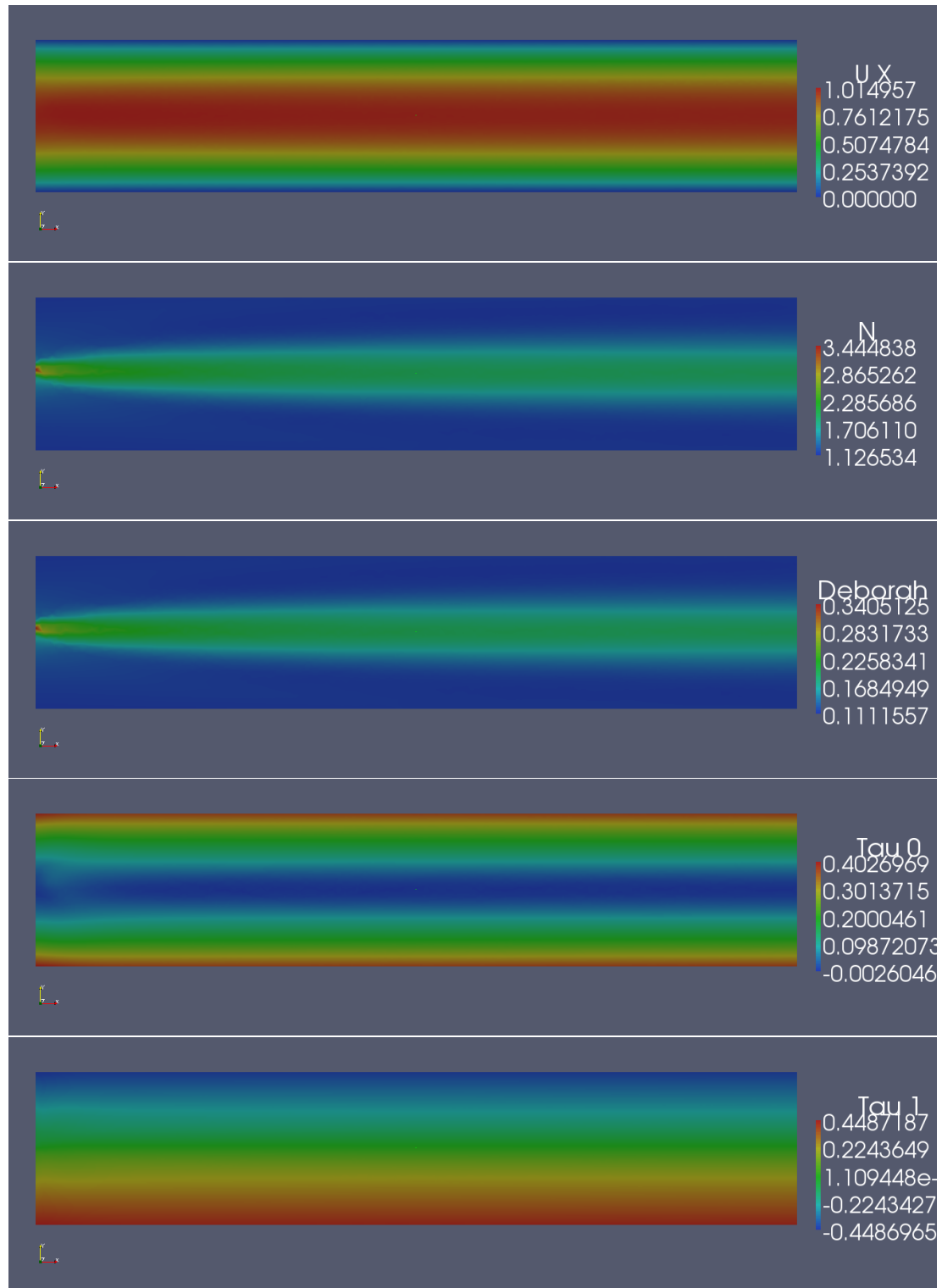


Figure 3.12: *Steady flow in a straight channel. Plotted from top to bottom are: u_x , \hat{N} , De , τ_{xx} and τ_{xy} .*

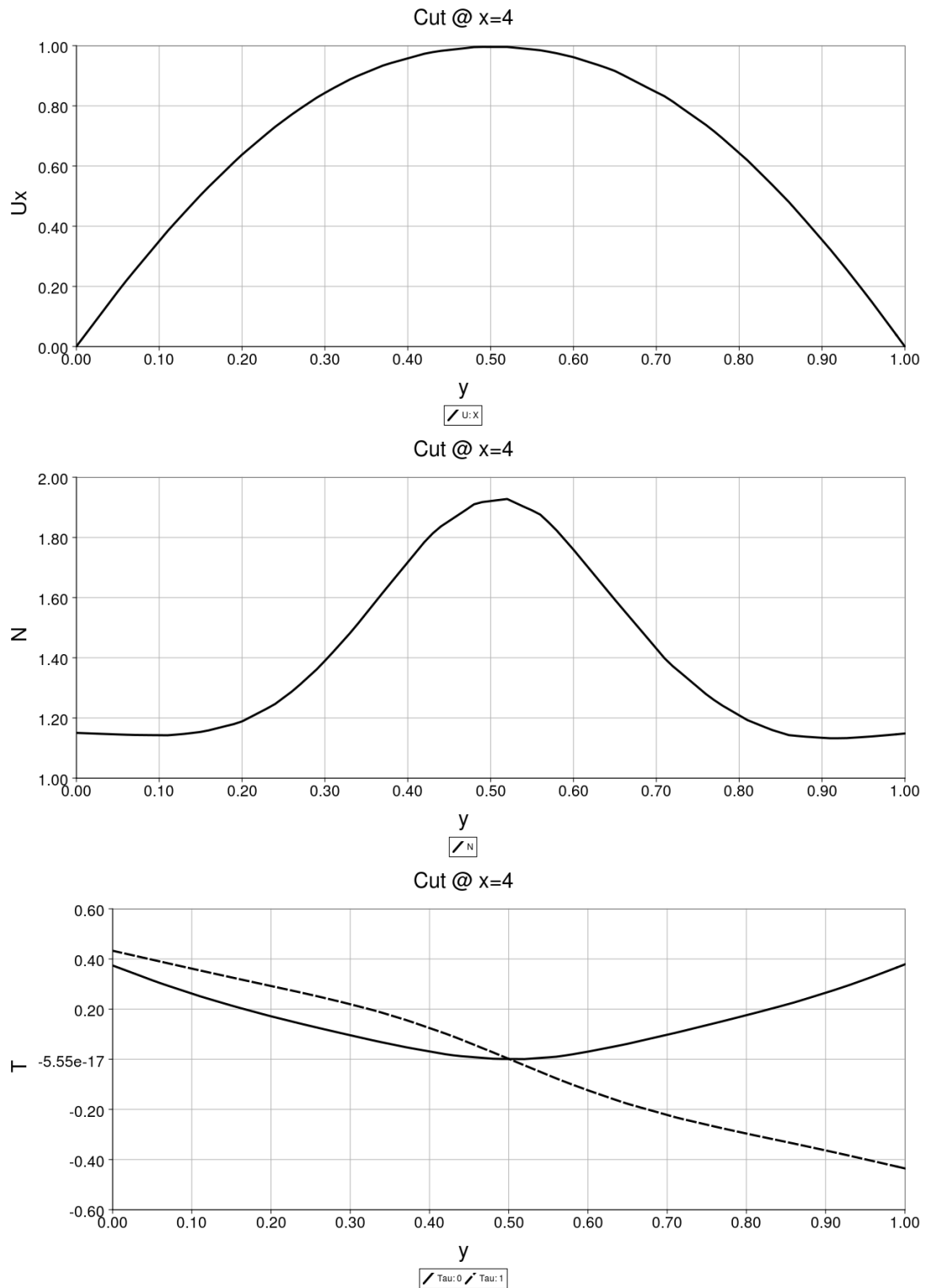


Figure 3.13: Steady flow in a straight channel, cut at $x = 4$. Plotted from top to bottom are: u_x , \hat{N} , and $\boldsymbol{\tau}$. On the bottom graph, the two variables are τ_{xx} (in solid) and τ_{xy} (dashed).

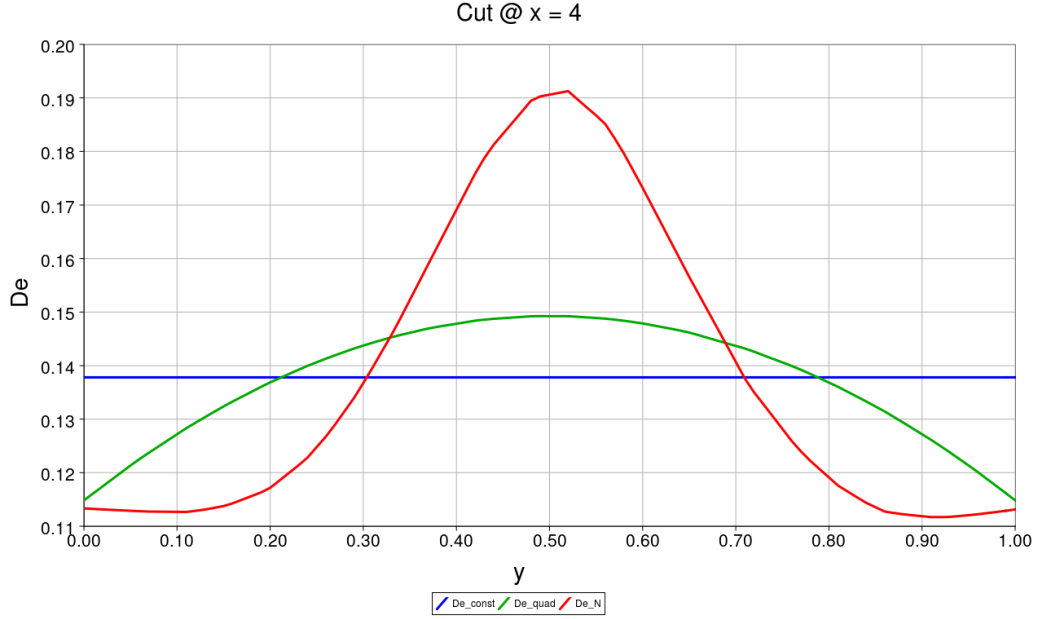


Figure 3.14: *Cross-wise distribution for different profiles for De . De_{const} (blue), De_{quad} (green) and $De_{\hat{N}}$ (red)*

everywhere on Ω , effectively removing the effect of \hat{N} on the other variables. We have chosen this value since it equals the average value of $De(\hat{N})$ in the straight channel experiment computed in the previous section. We also want to see what is the effect of having a y -dependent De on the accuracy of our solution. Thus for our second test case we set $De = De_{quad} = 0.137(5/6 + (1-y)y)$. This is just a scaled quadratic whose average over the domain will be the same as De_{const} . We will compare the solutions arising from both test cases against the analytic solution given in Eq. 3.2.1. Note that in assuming these expressions for De , the entire role of \hat{N} has been eliminated from the system of equations. For comparison, in Fig. 3.14 we plot the profiles of De_{const} , De_{quad} and our solution from the previous section, $De = De(\hat{N})$, along a vertical cut at $x = 4$.

We will look at the $\mathcal{L}^1(\Omega)$ errors for the two test cases for the variables, u_x , τ_{xx}

Test Case	$\tilde{E}_{\tau_{xx}}$	$\tilde{E}_{\tau_{xy}}$	\tilde{E}_{u_x}
De_{const}	0.0044	0.0001	0.0000
De_{quad}	0.0226	0.0109	0.0035

Table 3.3: *Errors for the viscoelastic variables in a straight channel.*

and τ_{xy} . We define the local error on, for example, τ_{xx} as:

$$e_{\tau_{xx}}(x, y) := |\tau_{xx}^h - \tau_{xx}^a|$$

where τ_{xx}^h is the FE solution and τ_{xx}^a is the analytical solution from Eq. 3.2.1.

Again using τ_{xx} as an example, we define the relative local error, $\tilde{e}_{\tau_{xx}}(x, y)$ as:

$$\tilde{e}_{\tau_{xx}}(x, y) := e_{\tau_{xx}}(x, y) / (|\tau_{xx}^h| + 0.01) * 100$$

And the relative global error, $\tilde{E}_{\tau_{xx}}$ on τ_{xx} as:

$$\tilde{E}_{\tau_{xx}} := \|e_{\tau_{xx}}\|_{\mathcal{L}^1(\Omega)} / \|\tau_{xx}\|_{\mathcal{L}^1(\Omega)}$$

The relative global errors for the two cases are given in Tab. 3.3.

We see that the case of De_{quad} is more difficult and we incur a higher error, but nevertheless our scheme is quite accurate. We also plot the relative error $\tilde{e}_{\tau_{xy}}$ in Fig. 3.15 over a vertical cut at $x = 4$. The areas where \tilde{e} is largest is in the middle and it corresponds to areas of very low values for τ_{xx} , τ_{xy} , i.e. this is less a symptom of inaccuracy than of dividing by a small number.

With this we feel that our scheme accurately captures the features for Oldroyd-B type fluids in steady flow.

3.2.4 Mesh Convergence

As is standard in numerical PDE's experiments, we now proceed to establish that our solution converges with mesh refinement. We return to steady flow for the fully coupled problem with $De = De(\hat{N})$ and consider three meshes on the channel, whose

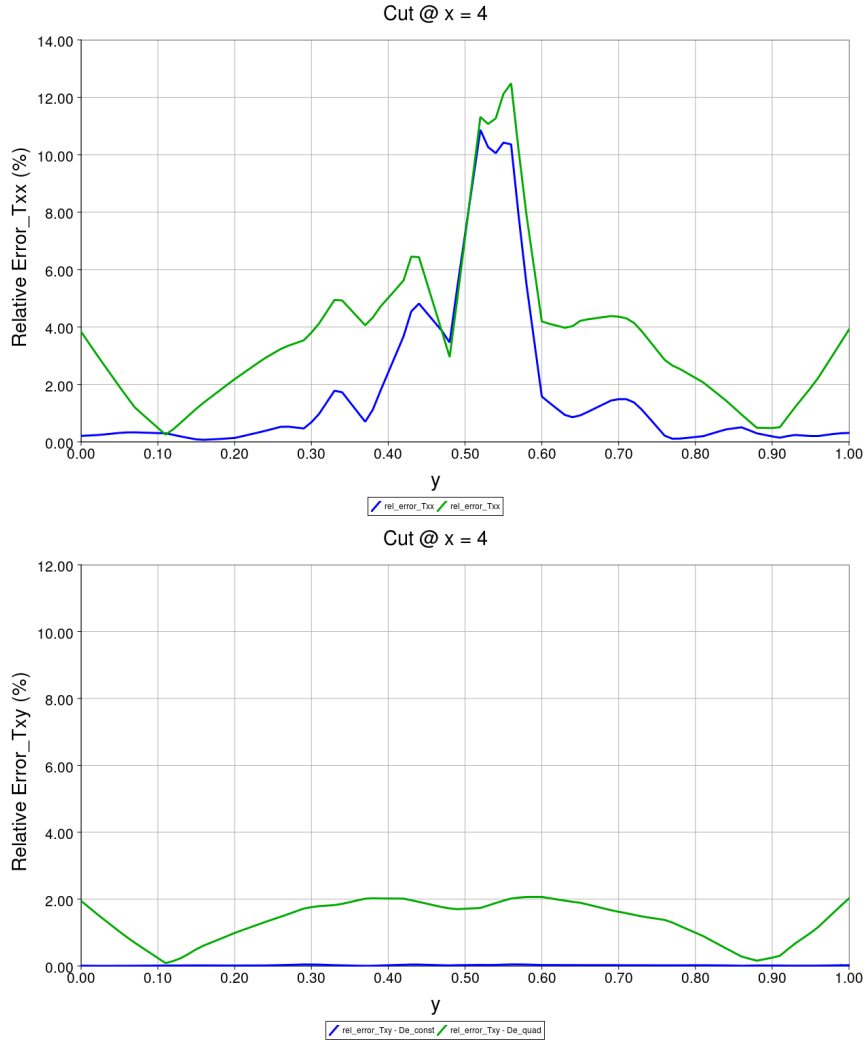


Figure 3.15: $\tilde{e}_{\tau_{xx}}$, $\tilde{e}_{\tau_{xy}}$ for different De 's. $\tilde{e}_{\tau_{xx}}$ (top), $\tilde{e}_{\tau_{xy}}$ (bottom) The relative error for De_{const} is plotted in blue, the relative error for De_{quad} is plotted in green.

Mesh ID	# Elements	# Vertices
X1	4482	2360
X2	17928	9201
X3	39374	20040

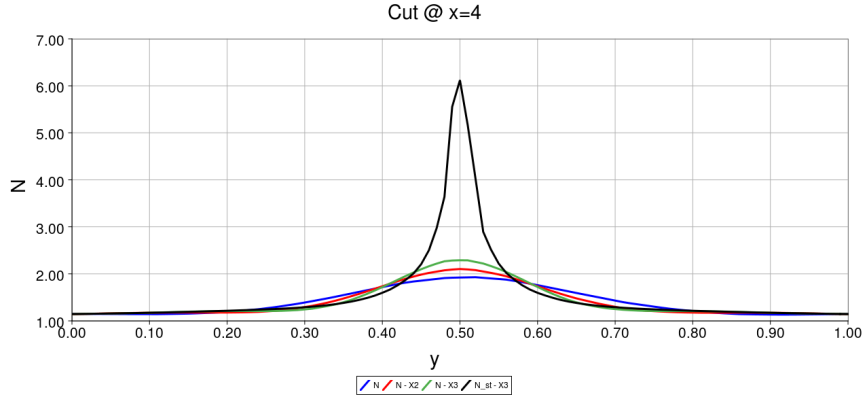
Table 3.4: *Straight Channel Meshes.*

Figure 3.16: \hat{N} with mesh refinement. \hat{N} on mesh X1 is plotted in blue. \hat{N} on mesh X2 is plotted in red. \hat{N} on mesh X3 is plotted in green. \hat{N}_{st} calculated on the finest mesh, X3, is plotted in black. These are plotted on a vertical cut through the channel taken at $x = 4$.

characteristics are provided in Tab. 3.4. X2 is obtained from X1 by splitting uniformly every edge of the mesh in two. This creates four triangles in X2 for every triangle in X1. X3 is obtained by reducing the length of an edge in X2 by a factor of about 1.5.

In this steady flow test case, one of the biggest challenges turns out to be capturing the step peak in the value of \hat{N}_{st} in the FE solution of \hat{N} near areas of low shear-rate such as near the axis of the channel. Recall that according to Eq. 3.2.1 \hat{N} should equal \hat{N}_{st} . Figure 3.16 shows that even though the finer meshes improve the solution, there is still a gap between \hat{N} and \hat{N}_{st} near the middle of the flow, where the shear-rate vanishes.

We observe however that the incremental changes on De with mesh refinement have only a negligible effect on the behaviour of the elastic stress and the velocity.

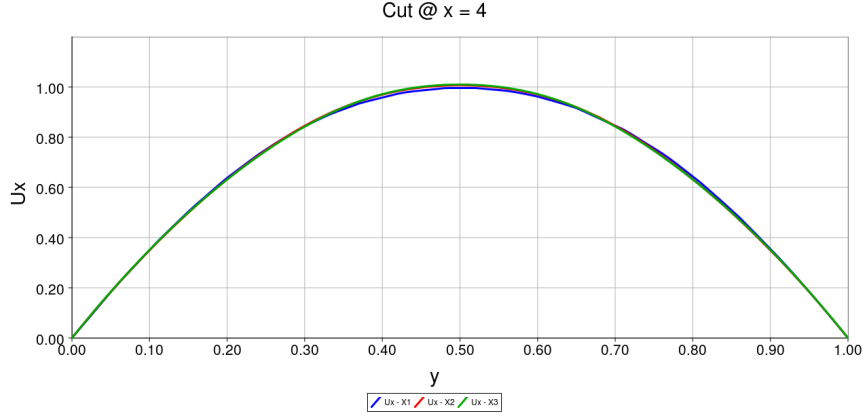


Figure 3.17: u_x in straight channel with mesh refinement. u_x on mesh X1 blue, u_x on mesh X2 red, u_x on mesh X3 green

Plotting \mathbf{u} , τ_{xx} and τ_{xy} along the same vertical cut shows almost no change in their profile for the finer meshes (see Figs. 3.17 - 3.19). We conclude then that using a mesh resolution as in X1 is sufficient to provide accurate solutions for this rheological model.

3.2.5 Determination of the apparent viscosity, η_a , for an equivalent Newtonian fluid

Here we sketch out the procedure for determining the apparent viscosity η_a needed to make a Newtonian fluid 'equivalent' to the viscoelastic fluid modelled by (1.5.10)-(1.5.13). The two fluids are deemed equivalent if given identical values for the Reynolds number, Re , and velocity at the inlet, $\mathbf{u}|_{\Gamma_i}$, they have identical pressure gradients longitudinally along the channel. Consider the following expression for the Navier-Stokes equations for a Newtonian fluid in non-dimensional form:

$$\text{Re} \frac{D\mathbf{u}}{Dt} = -\nabla p + \nabla \cdot (2\eta_a \dot{\boldsymbol{\gamma}}) \quad (3.2.4)$$

We solve Eq. (3.2.4) together with the incompressibility condition, Eq. (1.5.11) in the straight channel domain detailed in Sec. 3.2.1 subject to exactly the same BC's for

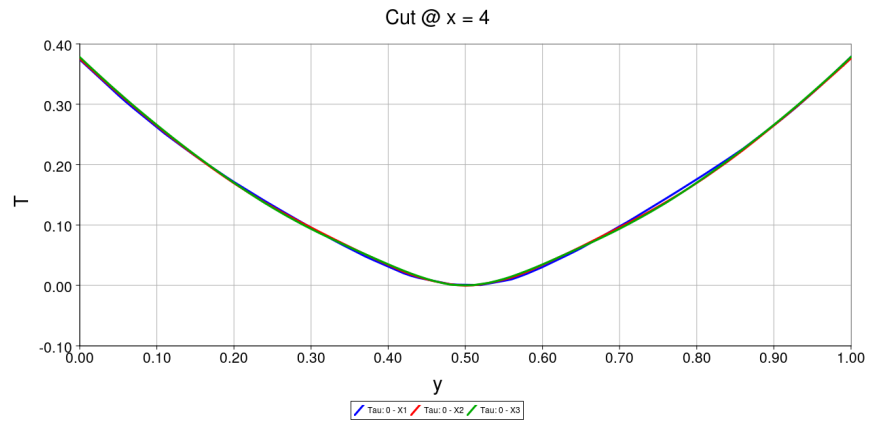


Figure 3.18: τ_{xx} with mesh refinement. τ_{xx} on mesh X1 blue, τ_{xx} on mesh X2 red, τ_{xx} on mesh X3 green

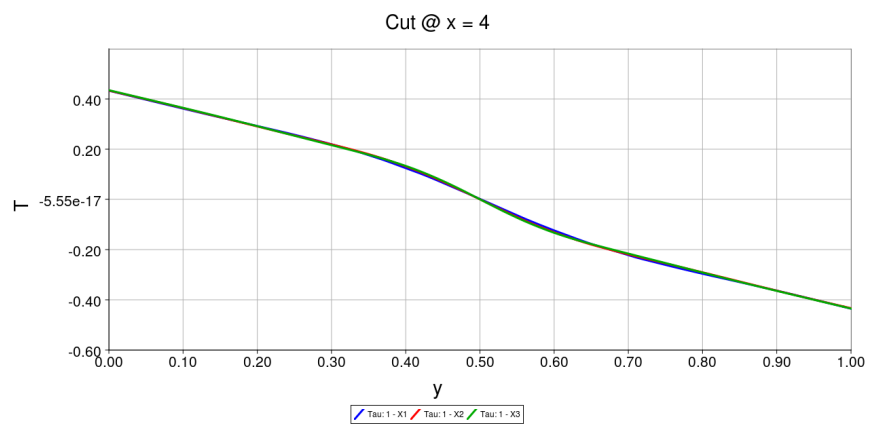


Figure 3.19: τ_{xy} with mesh refinement. τ_{xy} on mesh X1 blue, τ_{xy} on mesh X2 red, τ_{xy} on mesh X3 green

the velocity \mathbf{u} as for the viscoelastic fluid, with one notable exception, the inlet profile for the velocity. In particular we impose a constant inlet velocity $u_x = 1/2$ on both the Newtonian fluid model and the viscoelastic model. This is done in anticipation of the pulsatile simulations in Sec. 3.3. With this inlet velocity, we will obtain exactly the average of the time-varying volume influx during the pulsatile simulations. The determination of an equivalent Newtonian fluid is done in an ad-hoc way by varying the viscosity η_a in Eq. (3.2.4) until one obtains a pressure gradient in the Newtonian model that is identical to the one obtained from the viscoelastic model. Fig. 3.20 shows the difference between the pressures along the x -direction calculated with the fully coupled viscoelastic model vs. the pressure solution for the Newtonian model. Though the pressure gradients are almost identical in the downstream part of the channel, there is some discrepancy near the inlet. This, we attribute to the fact that the constant velocity across the inlet is transformed into a Poiseuille profile as the flow progresses into the geometry, but this has a different effect on the pressure in the momentum equation depending on whether the stress tensor has an elastic part, $\boldsymbol{\tau}$, or not. Indeed if we were to try to match the viscoelastic pressure near the inlet, by lowering η_a we will have worse agreement between the curves downstream. We have decided that the appropriate thing to match is the pressure downstream from the inlet, which is why we have chosen the η_a which gives us the blue curve in Fig. 3.20. The exact value is $\eta_a = 0.1532 = 4.6\eta_s$, where the value of the solvent viscosity, η_s , is taken from the equivalent viscoelastic simulation.

3.3 Flows in a Dilated Channel

Ultimately our goal is to perform pulsating flow experiments simulating physiological conditions in blood vessels. Of particular interest would be to investigate the model's behaviour near geometric features which allow for stagnant or recirculatory flow. An example is the case of an abrupt dilation in a channel, which is what we now pursue.

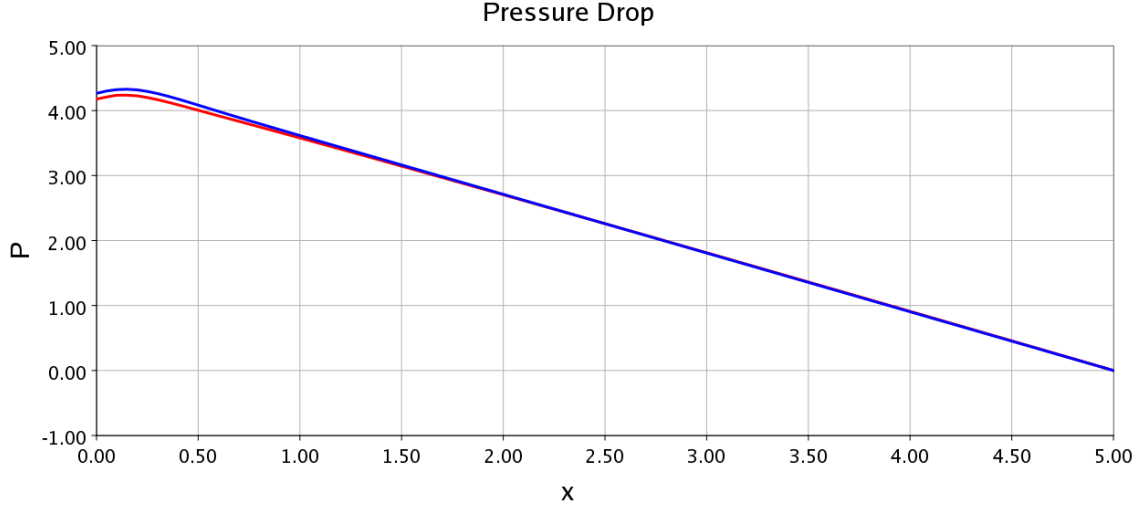


Figure 3.20: *Pressure drops for Newtonian and viscoelastic fluids in straight channel. Newtonian fluid is in blue and the viscoelastic fluid is in red. For the Newtonian fluid we have $\eta_a = 4.6\eta_s$.*

3.3.1 Geometry and Boundary Conditions for Flow in a Dilated Channel

The configuration for this experiment is illustrated in Fig. 3.21. As explained in Sec. 1.5.2, we separate the boundary in three segments: inlet, Γ_i ; walls, Γ_w , and outlet, Γ_o . At Γ_i , we impose values for \mathbf{u} , $\boldsymbol{\tau}$ and \hat{N} . We impose a time-dependent plug flow in the lateral direction, $\mathbf{u}|_{\Gamma_i} = (u_x(t), 0)^T$, for some time dependent $u_x(t)$. In the case of a plug flow, the consistent values to impose for $\boldsymbol{\tau}$ and \hat{N} are: $\boldsymbol{\tau}|_{\Gamma_i} = \mathbf{0}$ and $\hat{N}|_{\Gamma_i} = \hat{N}_{st}(\dot{\gamma} = 0)$. On Γ_w we impose no-slip condition on the velocity, $\mathbf{u} = \mathbf{0}$. At the outlet, Γ_o , we impose the natural outflow condition, $-p + 2\eta_s\partial_x u_x = 0$, and no flow in the y -direction, $u_y = 0$.

Note that applying a plug inflow for the velocity allows to write down simple inlet conditions for \hat{N} and $\boldsymbol{\tau}$. If we choose to use other profiles for the velocity, for example pressure-driven Womersley-like flow, then we would have to solve a simplified version

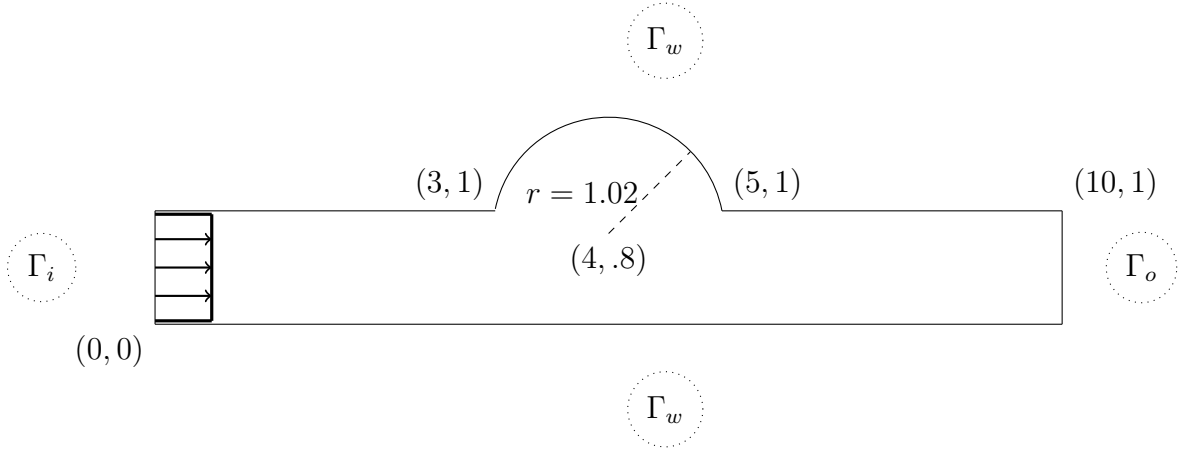


Figure 3.21: *Flow in a dilated channel - geometry and boundary conditions. See text for details.*

of the system of equations, (1.5.10)-(1.5.13), for the case of an infinite channel that is for a 1D geometry and then apply the 1D solution as an inlet BC.

For the majority of our pulsatile experiments we will use the mesh shown in Fig. 3.22. It has 5760 triangular elements and 3049 nodes. What is immediately clear from a visual inspection of the mesh are the regions of larger elements near the inlet and outlet. This was an artifact of the meshing algorithm, but we also generated meshes where the element size was uniform throughout. However we found that having the mesh coarser near the inlet allowed us to compute at higher values of De_∞ . While it is not exactly clear why that is, a possible explanation might be that the coarser elements near the inlet, rectify the plug inflow near the corners and thus reduce the strength of the corner singularities for $\dot{\gamma}_{xy}$ and $\nabla \mathbf{u}$, which both appear in the equation, (1.5.13), for $\boldsymbol{\tau}$.

The black, vertical lines crossing the mesh in Fig. 3.22 indicate the locations of the cuts across the geometry along which we later plot the variables; the precise locations are $x = 3.3, 4.7, 5.3$.

Note that we have smoothed the corners where the dilation begins and ends by using

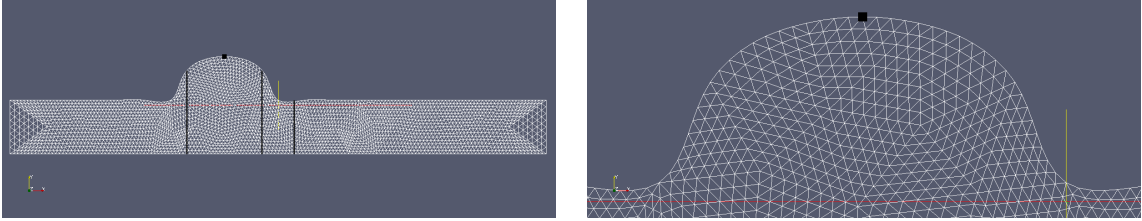


Figure 3.22: *The mesh X8 for the dilated channel. Entire mesh on the left, close-up of the dilation on the right.*

the MEF++ tool iMEF++ which has an internal mechanism for eliminating sharp corners in the geometry. .

3.3.2 Steady Flow

We first compute a steady flow in the dilated channel. This steady flow will be used to initiate pulsatile flow simulations in this geometry. At the inflow, we set $\mathbf{u}|_{\Gamma_i} = (1, 0)^T$. The surface plots for the variables can be seen in Fig. 3.23. Longitudinally the flow goes through three distinct sections. In the first section, between the inlet and the dilation, we see the plug inflow developing into a Poiseuille flow. In the next section where the dilation occurs, the flow slows down and diverts upward to follow the geometry. And in the third section, past the dilation, the flow evolves again into the Poiseuille flow of an infinite straight channel. Prescribing a plug inflow generates very high shear stresses along the walls immediately past the inlet. This is seen in the high values for all components of $\boldsymbol{\tau}$ near the inlet walls. Though the shear decreases downstream from the inlet as the plug profile for u_x is rectified into a parabolic profile, these high value for $\boldsymbol{\tau}$ only progressively relax downstream since the large elastic stress, $\boldsymbol{\tau}$, near the inlet is advected by the flow into the domain. Note for example the difference in the elastic stress between the area of the channel just before and just past the dilation. These differences occur even though the velocity and thus viscous shear stresses, $2\eta_s \dot{\boldsymbol{\gamma}}$, are roughly identical in both areas. The high-shear stresses near

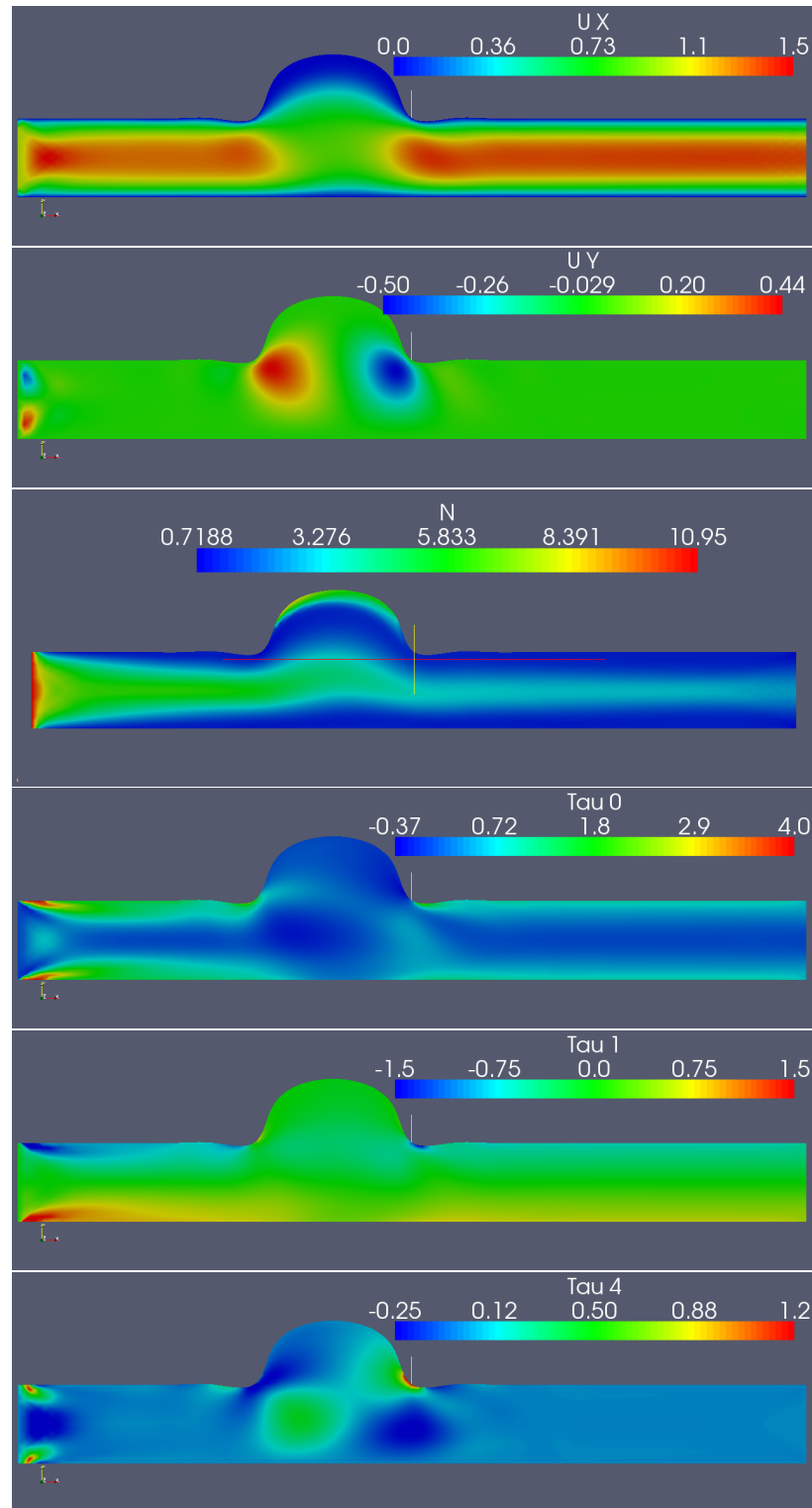


Figure 3.23: *Steady Flow in a Dilated Channel.* The steady state solution given a plug inflow. From top to bottom, u_x , u_y , \hat{N} , τ_{xx} , τ_{xy} , τ_{yy} . $\text{Re} = 25.4553$, $\text{De}_\infty = 0.1$.

the walls induce the opposite reaction for the average rouleau size, \hat{N} . The inlet value for \hat{N} is high given the absence of shear in the assumed incoming flow for the inlet BC, but the wall induced viscous shear immediately reduces the average rouleau size near the walls. Nevertheless the high values for \hat{N} entering at the inlet do continue to have some effect on the cross-sectional profile of \hat{N} as they are advected well into the dilation.

At $\text{Re} \approx 25$, the flow is well in the laminar regime and the velocity varies smoothly through the dilation, symmetrically rising and falling in direction to follow the boundary of the geometry. On the other hand the distribution of the elastic stress through the dilation is rather asymmetric. We see that the corners of the dilation have a strong effect on the elastic stress, with τ_{yy} increasing near the downstream corner, while τ_{xx} being greatest near the upstream corner after which it makes a shallow arch across the dilation before reentering the post-dilation channel. The behaviour of \hat{N} is dictated by the local shear-rate and the flow direction. With the fluid moving upward, the distribution of \hat{N} entering the dilation from the pre-dilation channel also shifts to follow the flow. More interestingly, there is an area of quite low viscous shear, $\dot{\gamma}$, and flow stagnation near the upper wall of the dilation and this causes the largest values of \hat{N} to appear near that upper wall. An increase in \hat{N} implies an increase in De and so near the upper wall a tug-of-war occurs in the behaviour of $\boldsymbol{\tau}$. On one hand we have low shear-rates and therefore low values for the components of $\dot{\boldsymbol{\gamma}}$. On the other hand, the local Deborah number, De , is increased. In effect this results in a rather uniform value for $\boldsymbol{\tau}$ cross-sectionally within the dilation.

The effect of the dilation over the flow is quite short in space. As can be seen in Fig. 3.26, by $x = 5.3$, which is .3 non-dimensional length units past the end of the dilation, the velocity and rouleau size have already re-assumed their straight channel profiles. The effect on $\boldsymbol{\tau}$ lasts a little further downstream, but not much before the elastic stress also recovers its infinite straight channel profile. This is another example of the viscoelastic response of the fluid.

Mesh	# Elements	# Vertices
X4	1440	805
X8	5760	3049

Table 3.5: *Dilated channel meshes.*

3.3.3 Mesh Independence Study

We now compare the solutions over two meshes to see the effect of mesh refinement. The mesh characteristics are given in Tab. 3.5. Mesh X4 is not shown here, but it is coarser than X8 (shown in Fig. 3.22) by a factor of two. In fact we obtain X8 by cutting all edges in X4 in two, thus creating four smaller triangle elements in X8 for every element in X4.

As indicated in Fig. 3.22, by the vertical black lines, we take three cuts across the geometry and compare the variables along them. The cuts are at $x = 3.3, 4.7, 5.3$, respectively at the beginning of the dilation, towards its end and just past the dilation. We compare the variables in Figs. 3.24 - 3.26. Note that the dilation is on top of the geometry and the abscissa on the graphs has $y = 0$ on its left so on the graphs the region with the dilation appears on the right.

We see then that the difference between the solution on the two meshes is not large. Moreover, the element size in X8 is close to the element size of mesh X1 for the straight channel, which was fine enough to obtain good solutions. Therefore we feel confident in using mesh X8 for the rest of the dilated channel simulations.

3.3.4 Pulsatile Experiments

For the pulsatile flow in the dilated channel we impose the following boundary condition on the inlet boundary, Γ_i :

$$u_x(t)|_{\Gamma_i} = (1 + \cos(2\pi\omega t))/2 \quad (3.3.1)$$

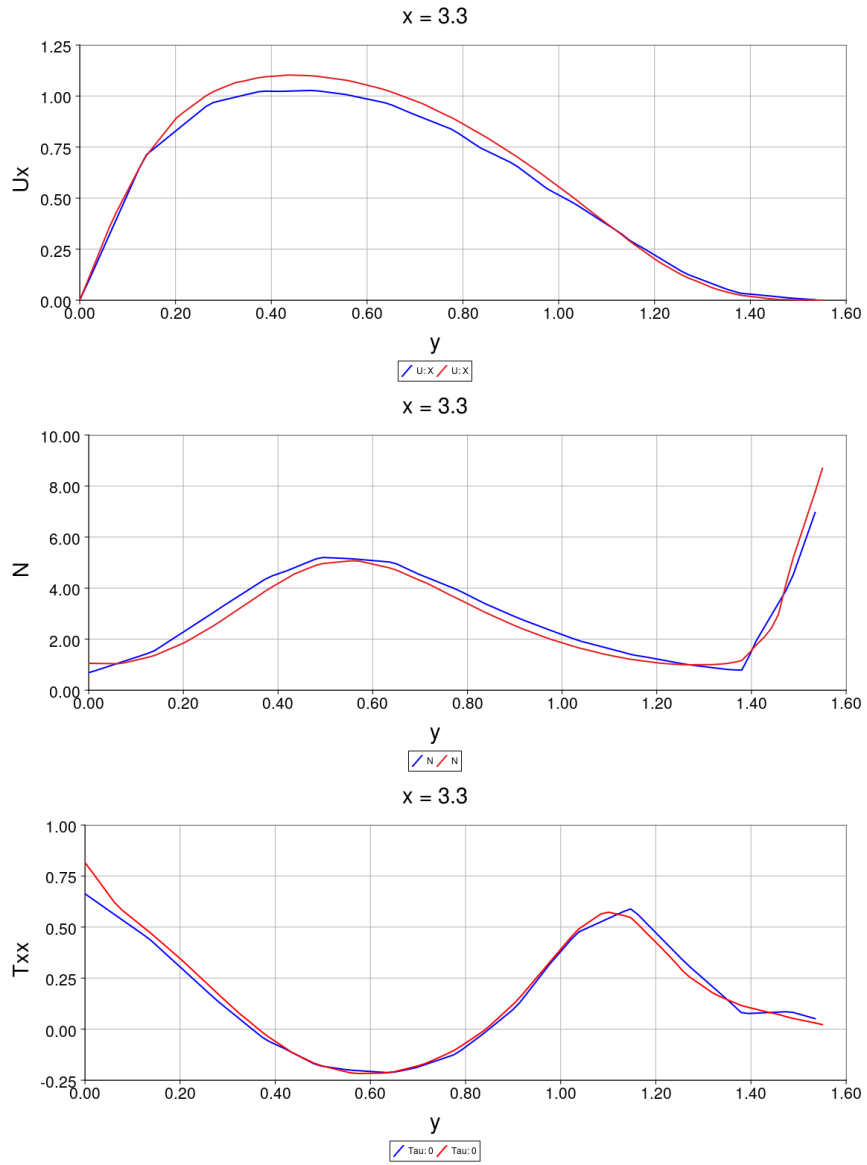


Figure 3.24: *Steady Flow – cut at $x = 3.3$. From top-to-bottom: u_x , \hat{N} , τ_{xx} . In dashed blue is the value for mesh X_4 , in red is the value for mesh X_8 .*

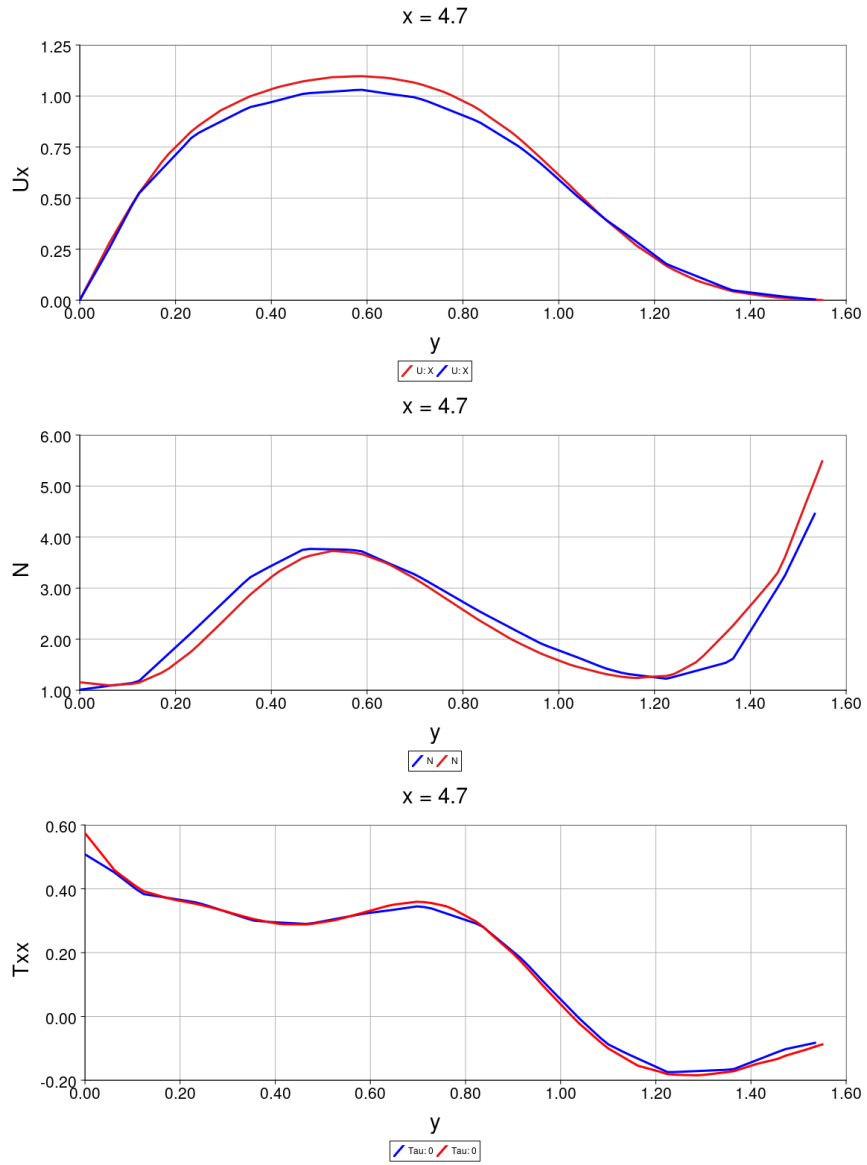


Figure 3.25: *Steady Flow – cut at $x = 4.7$. From top-to-bottom: u_x , \hat{N} , τ_{xx} . In dashed blue is the value for mesh X4, in red is the value for mesh X8.*

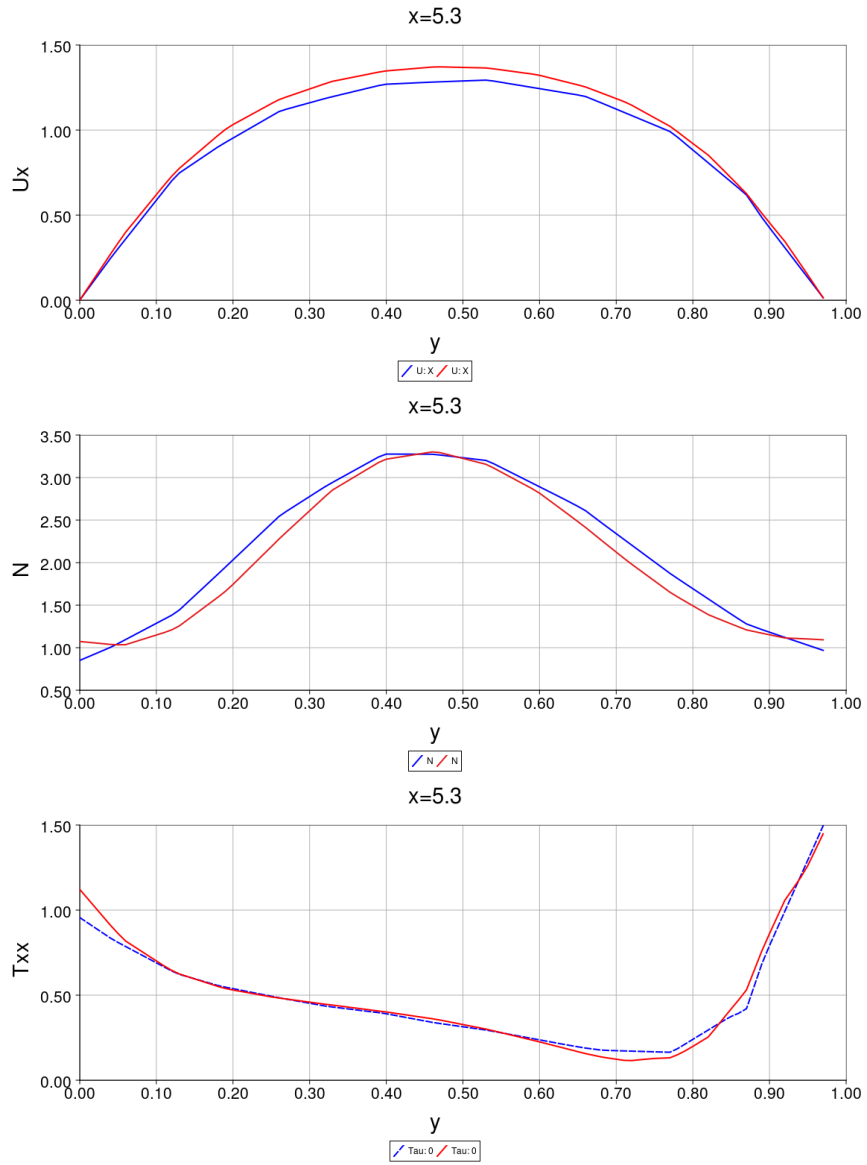


Figure 3.26: *Steady Flow – cut at $x = 5.3$. From top-to-bottom: u_x , \hat{N} , τ_{xx} . In dashed blue is the value for mesh X4, in red is the value for mesh X8.*

Parameter	Value	Comments (units)
Re	25.4553	Reynolds number
De_∞	0.1	Deborah number at infinite shear
ω'	1	physical frequency (Hz)
ω	0.05	non-dimensional frequency
<i>Cycles</i>	3	number of cycles computed
Δt	$0.01/\omega$	time-step size

Table 3.6: *Pulsatile Parameters.*

The steady solution obtained in Sec. 3.3.2 is used as initial condition for the pulsatile simulations. Tab. 3.6 shows the parameter values used in the computations. We have chosen Re and De_∞ as in the most recent papers of Owens et al. [8]. Unfortunately with our computational scheme and this form of the constitutive model, there is a limit on the values of De_∞ at which we can obtain convergent solutions. $\text{De}_\infty = 0.1$ is quite close to what we found to be an upper bound. For our physical frequency we have chosen a physiologically-reasonable value corresponding to 60 heart beats per minutes.

Snapshots of the flow variables during a single cycle over four equally spaced time intervals can be seen in Figs. 3.28 - 3.33. These are taken from the last (third) cycle of the simulation. The pressure p is not shown since essentially it is falling linearly across the domain. The time instances during the cycle when we show the variables are illustrated in Fig. 3.27. Time *I* corresponds to peak deceleration, time *II* to the minimal inflow velocity (peak diastole), time *III* to peak acceleration and time *IV* to maximum inflow velocity (peak systole).

A few things are notable when looking at the pulsatile solution. At this low Reynolds number, we have a lot of damping on the fluid and thus there is almost no flow at peak diastole, time *II*. At peak systole, time *IV*, we have a lot of shear which generates large values for the components of $\boldsymbol{\tau}$. $\text{De} \approx .26$ at time *II* and $\text{De} \approx .31$ at

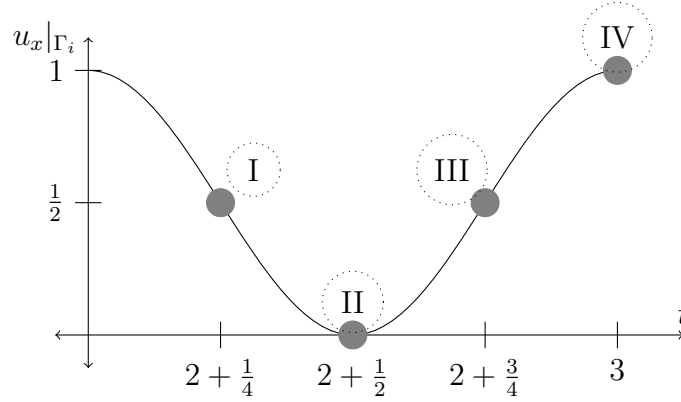


Figure 3.27: *Observation time instances for pulsatile flows.*

time *IV* is not a very high range for the Deborah number and so the delay in τ is not long.

With this parameter set, the solutions for \mathbf{u} and τ are quite symmetric in time around the middle of a cycle. That is \mathbf{u} and τ behave in the same way during the deceleration of the inlet velocity as they do during the acceleration as can be seen by comparing their respective surface plots at times *I* and *III*, which are very similar. We do not see the hysteresis for τ displayed in the coaxial rheometer experiment in Sec. 3.1. Moreover, we do not see a significant difference in the variables between different cycles; it seems a periodic solution is reached quickly. This is most obvious when we consider the graphs in Fig. 3.34, which detail the time evolution of the variables inside the dilation. We have chosen to sample them at the point $(x, y) = (3.7, 1.45)$, which is close to the middle of the dilation both laterally and longitudinally. What is interesting is that while \mathbf{u} and τ both oscillate in time due to the pulsation, \hat{N} remains quite constant. A similar behaviour was observed in the time-dependent simulations in the original papers of Owens et al. [20], [7], and we see that again here. Our initial conditions correspond to peak systole and correspondingly a low value for the average rouleau size across the domain. Even though during each pulse cycle the shear is reduced, the time-scales inherent in the parameter values for \hat{N} imply

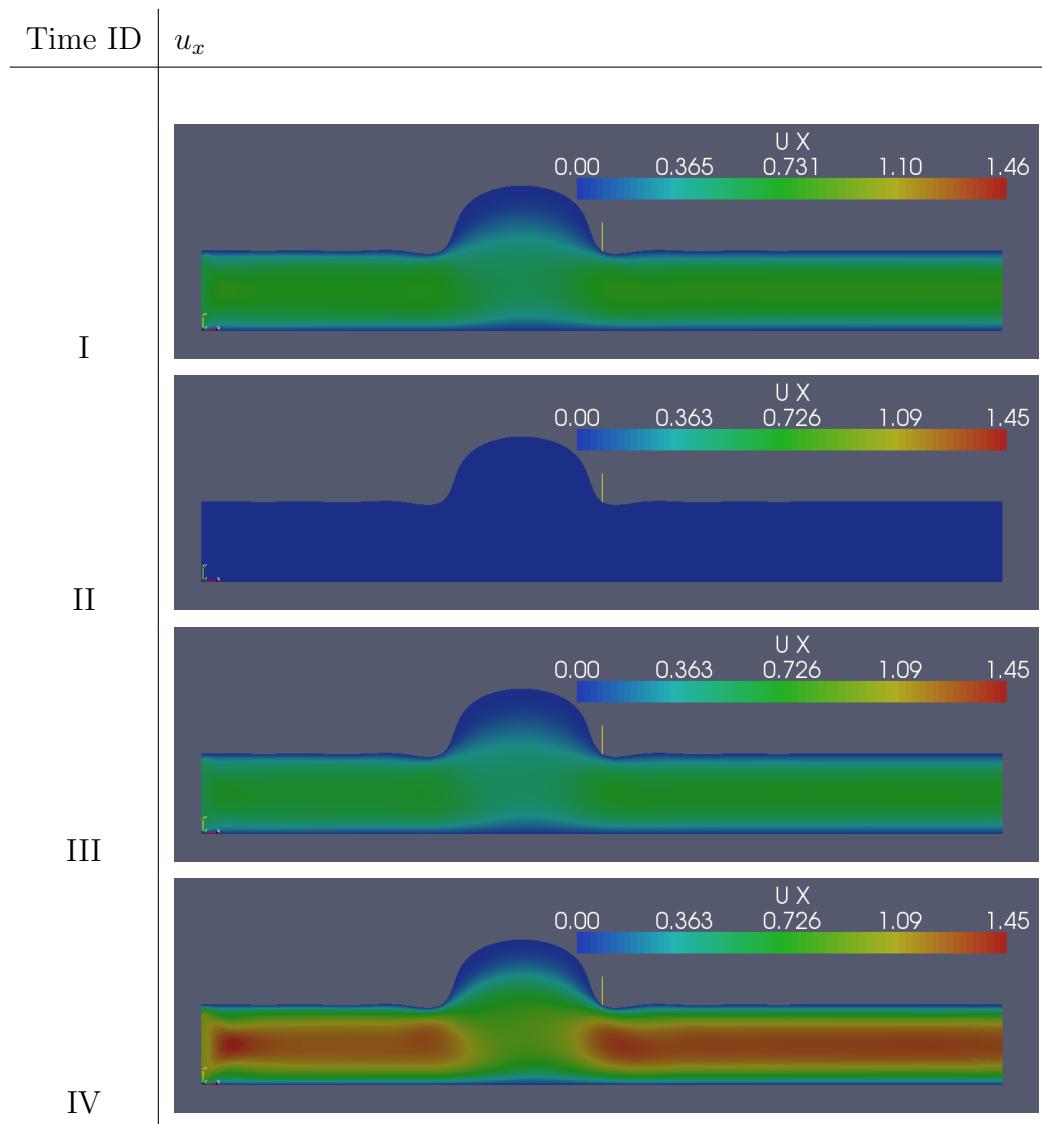


Figure 3.28: Horizontal velocity, u_x , at times I - IV of the pulsating test case.

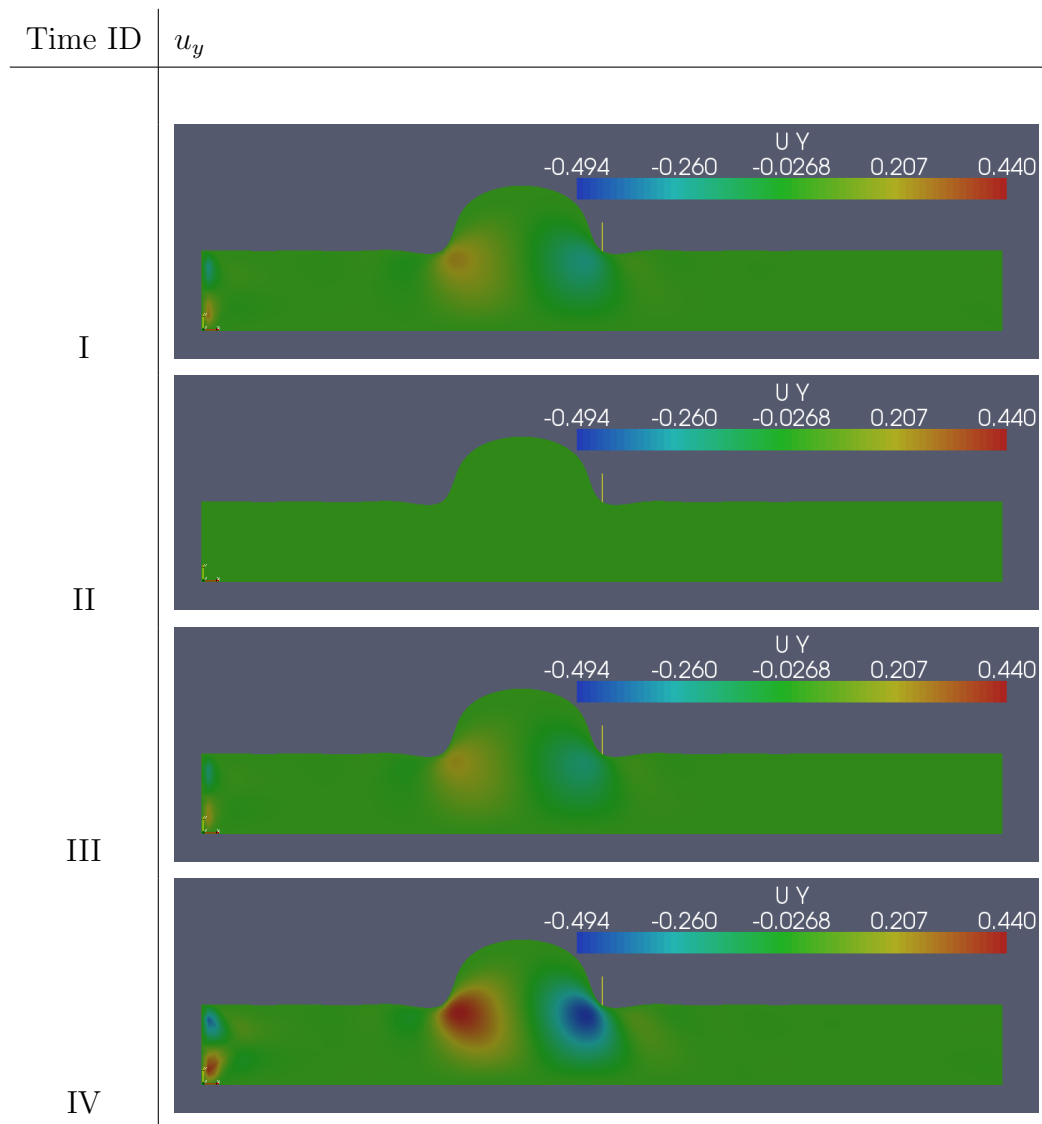


Figure 3.29: Vertical velocity, u_y , at times I - IV of the pulsating test case.

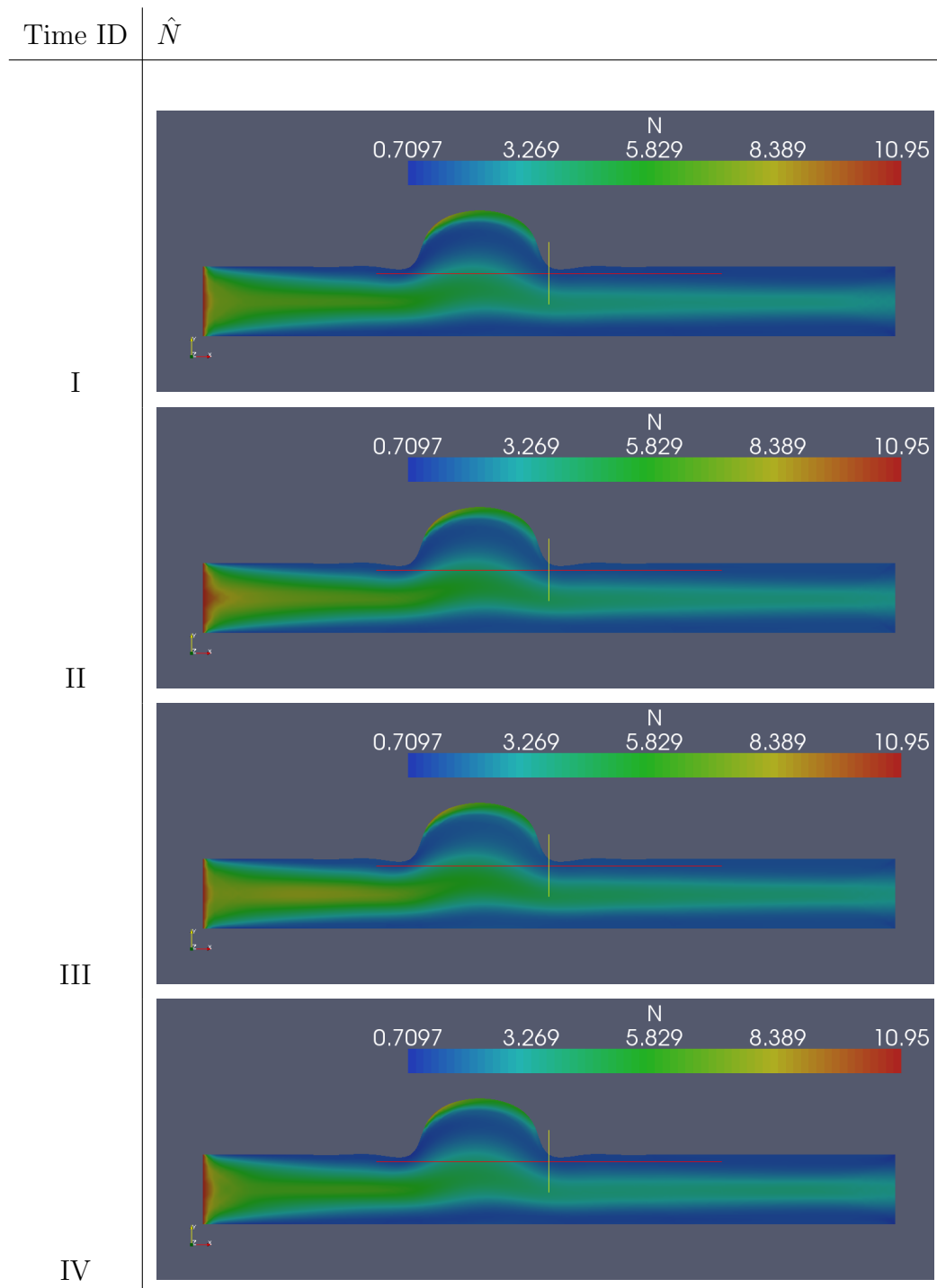


Figure 3.30: Average rouleau size, \hat{N} , at times I - IV of the pulsating test case.

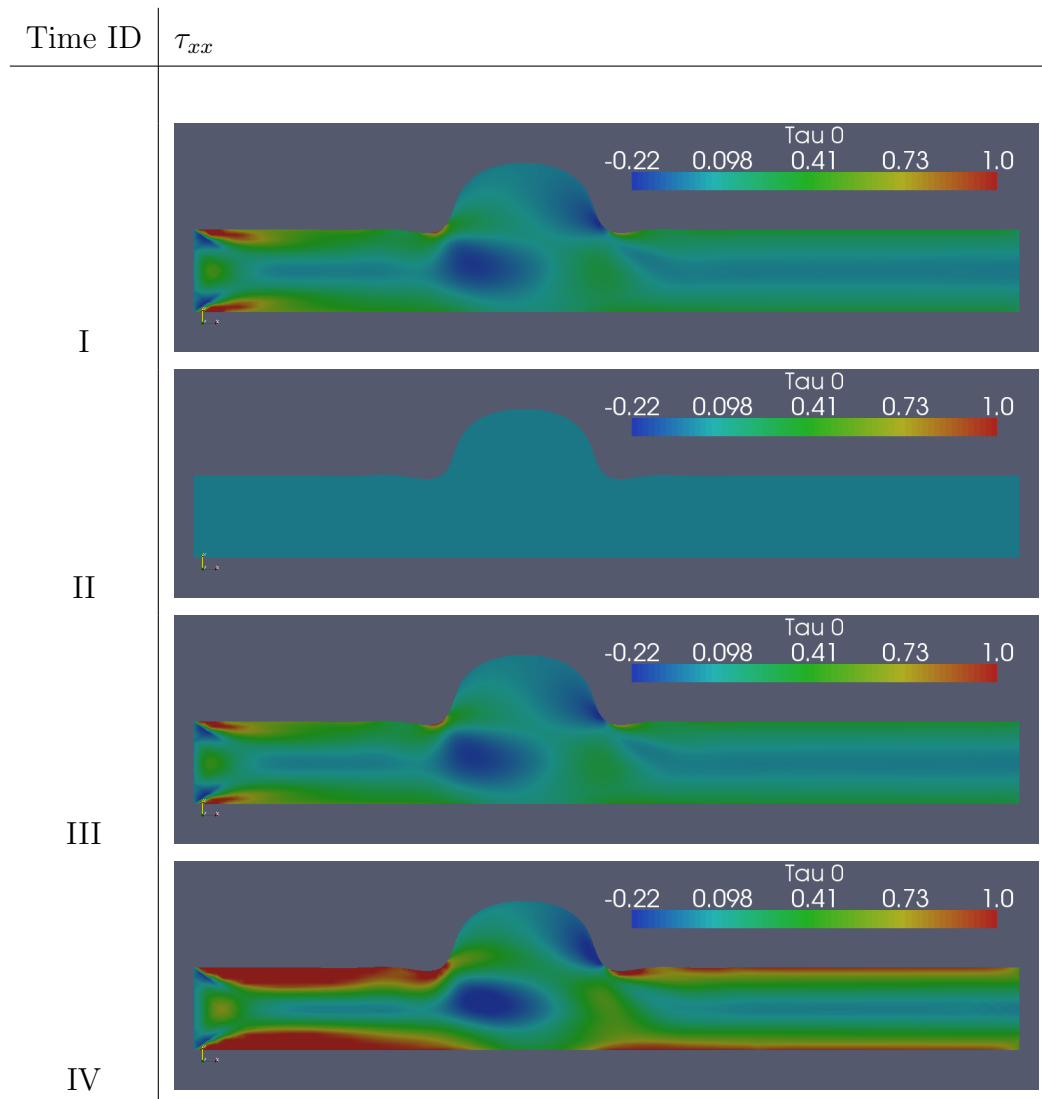


Figure 3.31: Component τ_{xx} of the elastic-stress tensor, at times I - IV of the pulsating test case.

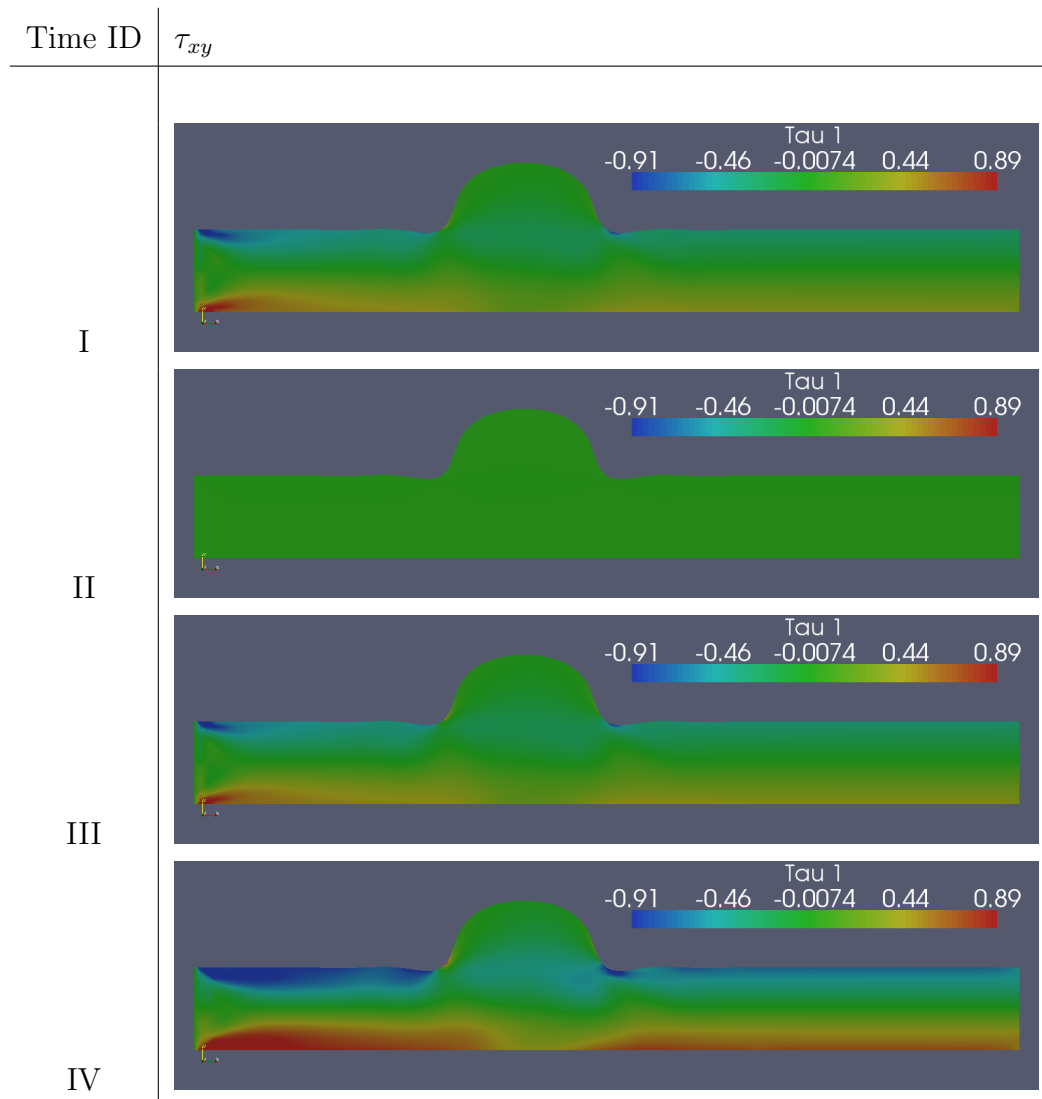


Figure 3.32: Component τ_{xy} of the elastic-stress tensor, at times I - IV of the pulsating test case.

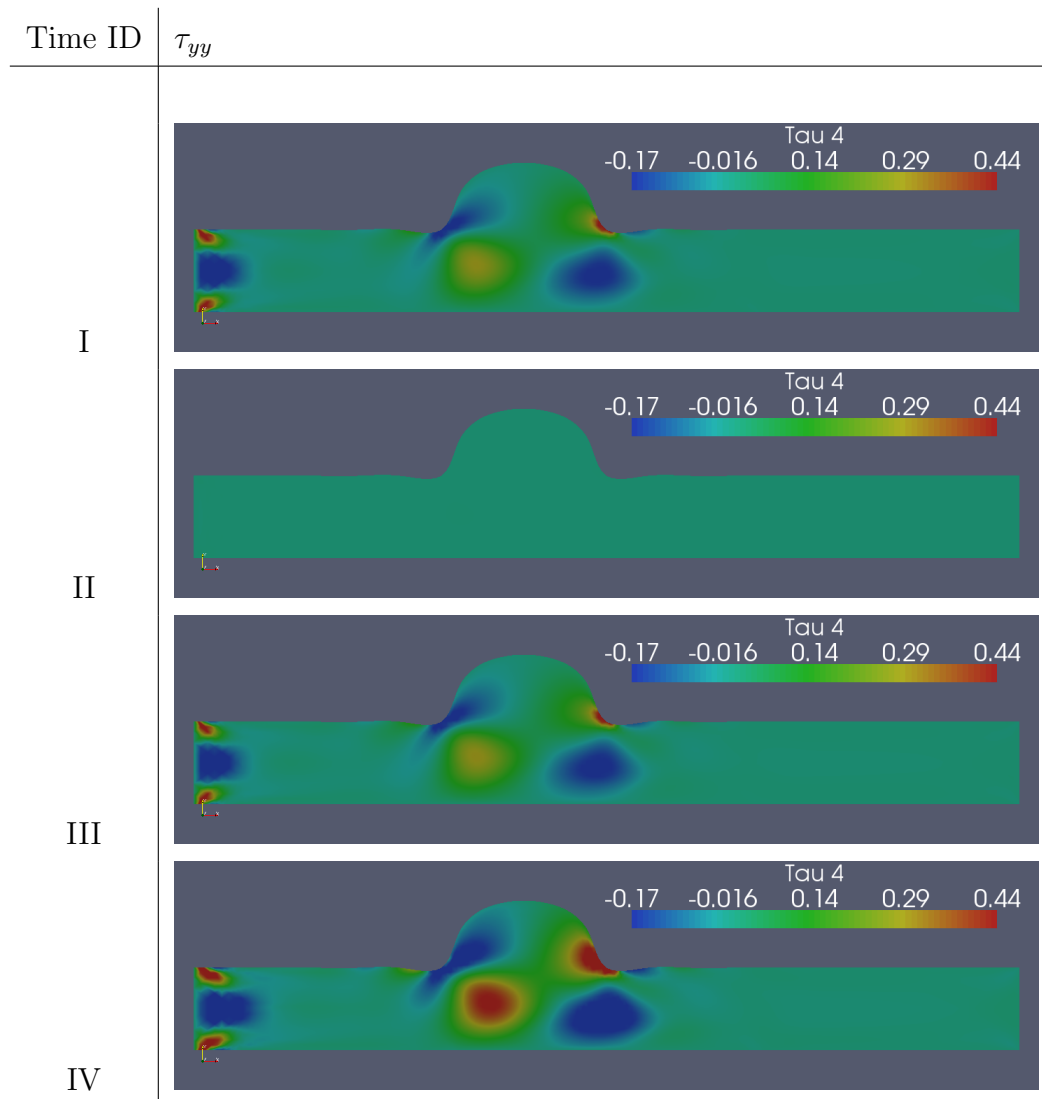


Figure 3.33: Component τ_{yy} of the elastic-stress tensor, at times I - IV of the pulsating test case.

that there is not enough time in this flow regime for the RBC's to aggregate into larger rouleaux. Therefore \hat{N} remains relatively constant despite the relatively large oscillations in \mathbf{u} and $\dot{\gamma}$.

Remark 3.3.1 Note that the pulsatile experiment in the dilated channel provided a posteriori one of the justifications for applying the SUPG technique on the equations. In particular setting α_h^{SU} to zero in Eqs. (2.4.4) and (2.4.5) (i.e if not utilizing SUPG) will result in a divergent solution during the middle of the first pulse cycle, whereas solutions can be obtained otherwise.

3.3.5 Comparison against Newtonian Flows

Having defined and established in Sec. 3.2.5 the Newtonian fluid equivalent to the viscoelastic fluid, we now proceed to compare the viscoelastic pulsatile flow against an equivalent Newtonian fluid. We solve for the Newtonian fluid as for the viscoelastic fluid by first obtaining a steady solution and then using this steady solution as an initial condition the time-dependent problem. The boundary conditions for the Newtonian model are just the velocity, \mathbf{u} , that was prescribed on the viscoelastic model. We use the value of η_a obtained in Sec. 3.2.5, $\eta_a = 4.6\eta_s$.

We first verify that the steady viscoelastic and Newtonian flows are indeed equivalent. This is roughly the case as could be seen by looking at the pressures from steady flow inside the dilated channel for both rheological models (see Fig. 3.35). As in the numerical experiment used to determine the value of η_a for the equivalent Newtonian fluid in the straight channel, there is a discrepancy in the area near the inlet between the pressures for the viscoelastic and the Newtonian models. This discrepancy is slightly more significant in the dilated channel. There is more restriction to flow and hence higher pressure drop induced by the inlet plug flow in the viscoelastic case than for the Newtonian model.

To analyze the differences between the two models, we will again consider the spatial

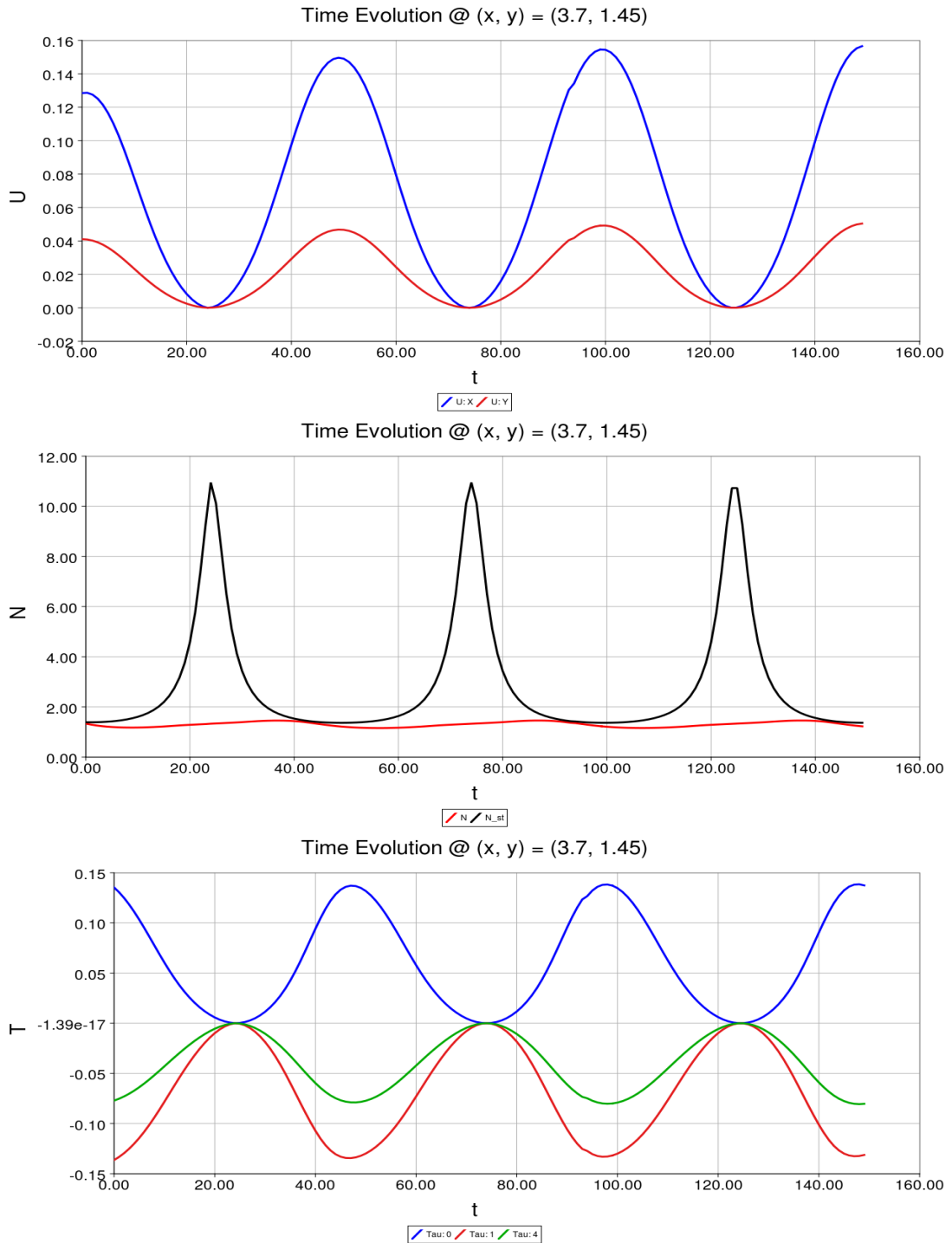


Figure 3.34: Time evolution for \mathbf{u} , \hat{N} , $\boldsymbol{\tau}$ over three pulsatile cycles inside the dilation of the dilated channel. From top to bottom \mathbf{u} , \hat{N} and $\boldsymbol{\tau}$. Top - u_x (blue) and u_y (red). Middle - \hat{N} (red) and \hat{N}_{st} (black). Bottom - τ_{xx} (blue), τ_{xy} (red) and τ_{yy} (green).

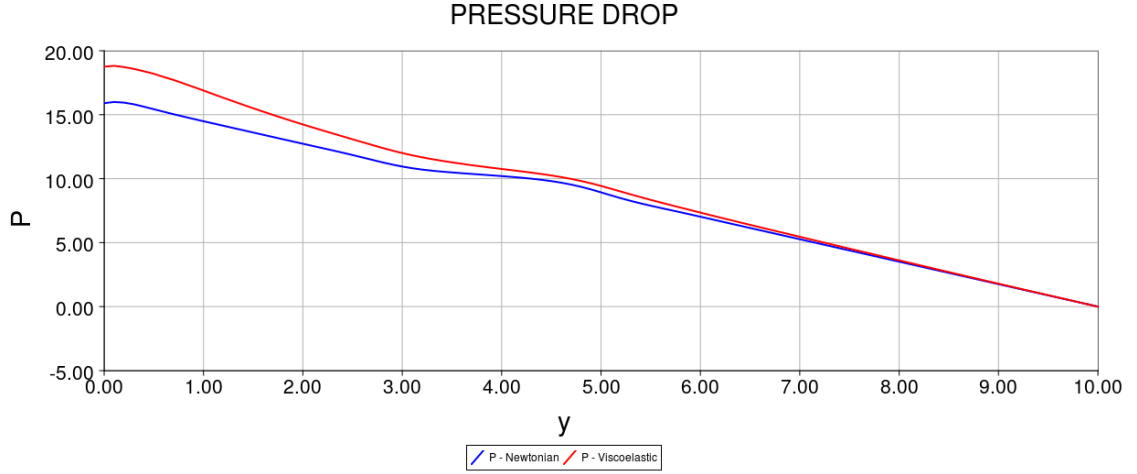


Figure 3.35: *Pressure drops for a Newtonian fluid and a viscoelastic fluid in a dilated channel. The Newtonian fluid is in blue and the viscoelastic fluid - in red*

distribution of the variables at the four instants in time defined by the peaks and the inflection points of the inlet velocity, $u_x|_{\Gamma_i}$, as indicated in Fig. 3.27, during the third, last cycle of the simulation. In particular we will inspect the variables along the following lines $x = 3.3, 4.7, 5.3$, respectively labelled as Increasing Dilation (ID), Diminishing Dilation (DD) and No Dilation (ND). We will see then what happens to the flow as it enters the dilation, as it begins to leave it and just after it has left it. In particular we will focus on the velocity components, u_x, u_y , and the components of the Cauchy stress tensor, σ_{xx}, σ_{xy} , and σ_{yy} . Recall that for a Newtonian model, the Cauchy stress tensor is given by

$$\boldsymbol{\sigma} = 2\eta_a \dot{\boldsymbol{\gamma}} \quad (3.3.2)$$

and that for the viscoelastic model, the Cauchy stress tensor is given by

$$\boldsymbol{\sigma} = \boldsymbol{\tau} + 2\eta_s \dot{\boldsymbol{\gamma}} \quad (3.3.3)$$

The comparisons between the variables from the two models can be seen in Figs.

3.36 to 3.40. As is typical for this type of viscoelastic fluid, the viscoelastic velocity profile is smeared in comparison to the velocity of the Newtonian fluid; that is the viscoelastic velocity has a flatter profile near the middle and then it falls off more steeply to reach zero near the walls. This behaviour remains true at all times during the cycle. The differences in u_x are on the order of 10%, the differences in u_y up to 30%. With regards to stress, the viscoelastic model has consistently higher values for all components of the Cauchy stress tensor, most dramatically for the tensile stresses, i.e. σ_{xx} and σ_{yy} .

We also looked at the evolution in time of the Cauchy stress near the wall inside the dilation. In Fig. 3.41 we plot the time evolution of σ_{xy} , the shear-stress component of $\boldsymbol{\sigma}$, as computed at the top of the dilation, i.e. $(x, y) = (4, 1.81)$. The probe location is also highlighted as a black dot in Fig. 3.22. We observed that the viscoelastic shear stress has a slightly delayed response and shows variation with larger amplitude than the Newtonian shear stress. Similarly to the timeplots in Fig. 3.34, the timeplot in Fig. 3.41 again demonstrates, at least heuristically, that the system quickly reaches a periodic state for both the viscoelastic as well as the Newtonian models.

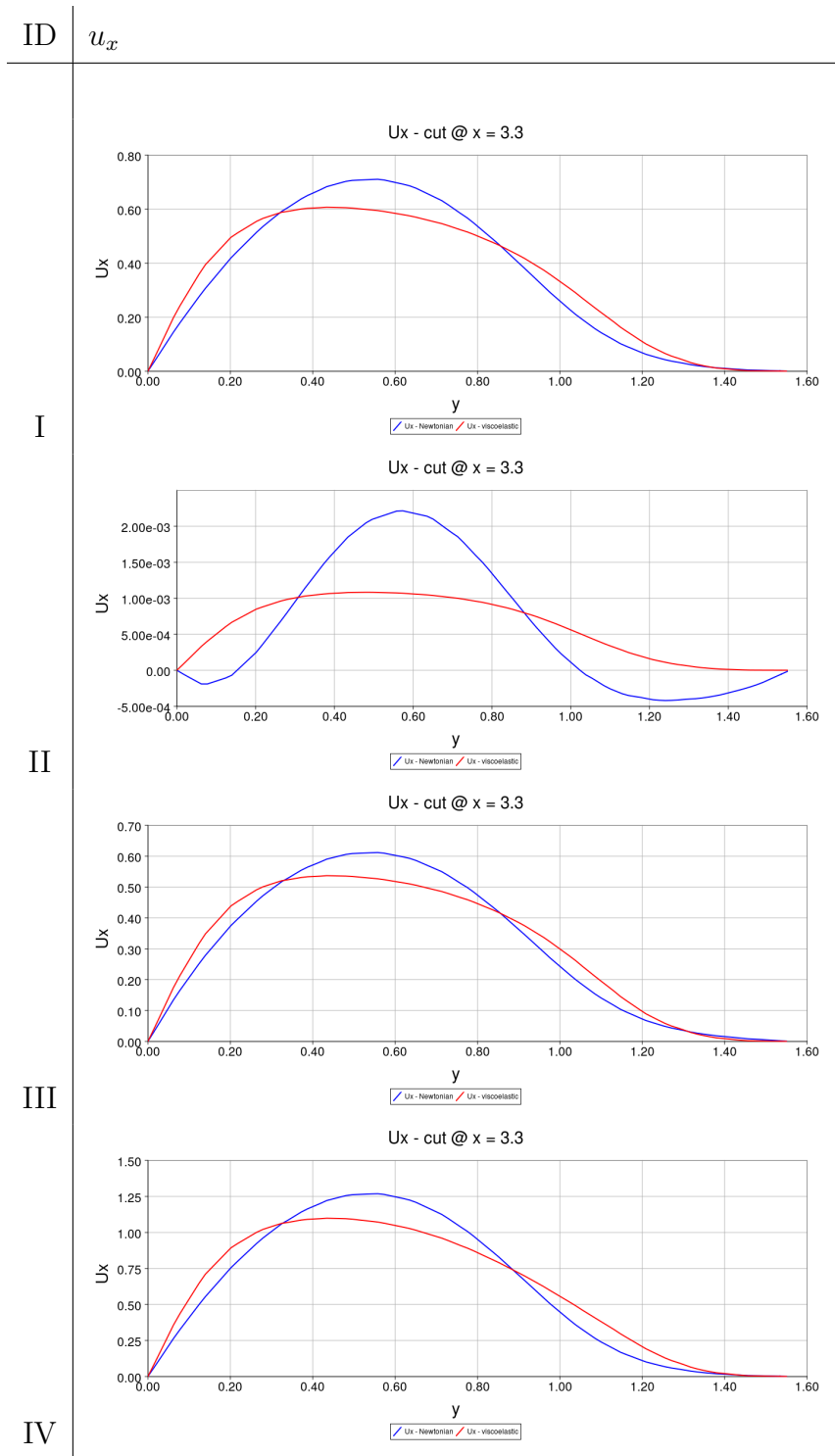


Figure 3.36: Comparison between u_x for a Newtonian fluid (blue) and the viscoelastic fluid (red) at four different times. The cut is taken along $x = 3.3$.

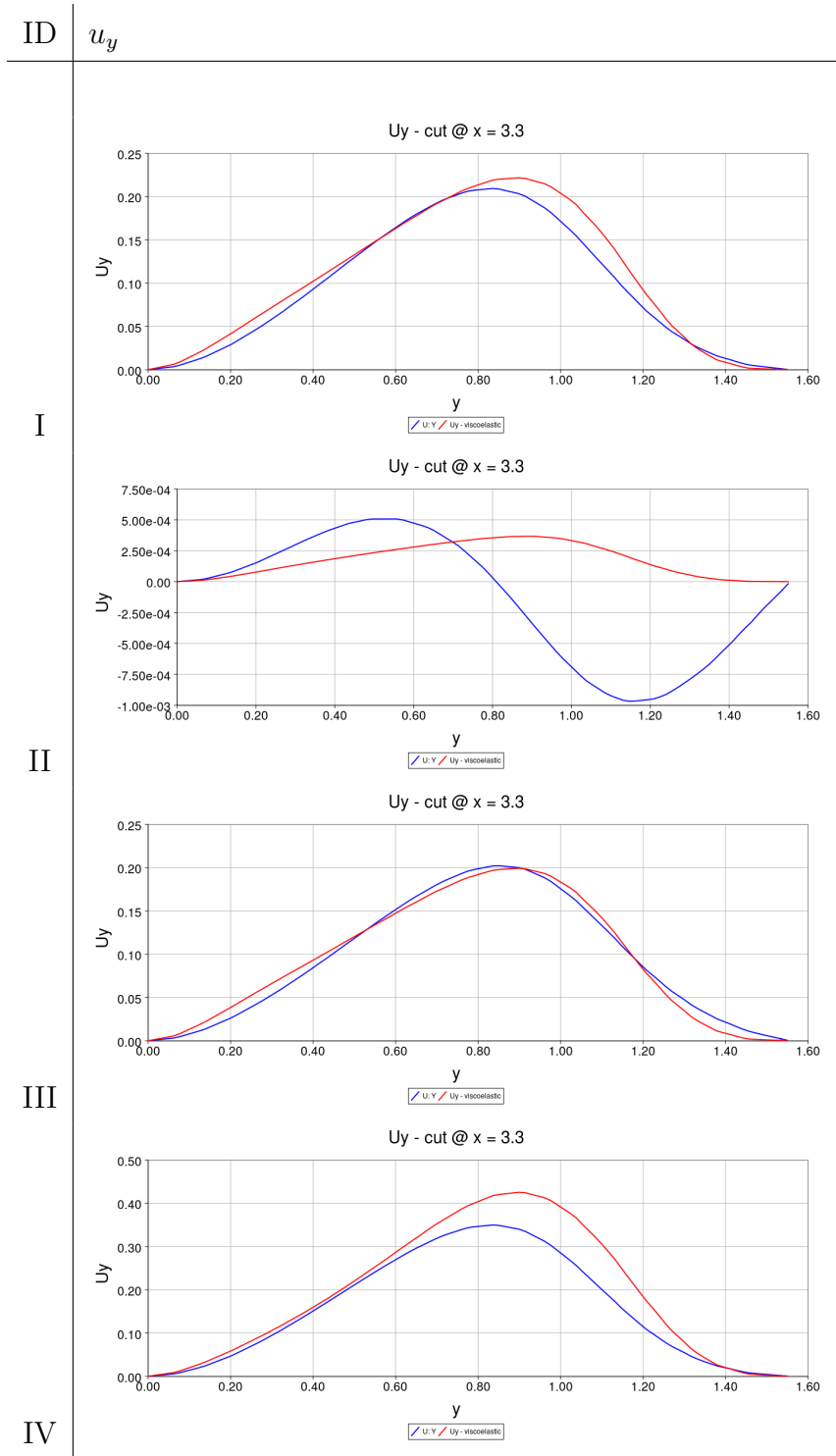


Figure 3.37: Comparison between u_y for a Newtonian fluid (blue) and a viscoelastic fluid (red) at four different times. The cut is taken along $x = 3.3$.

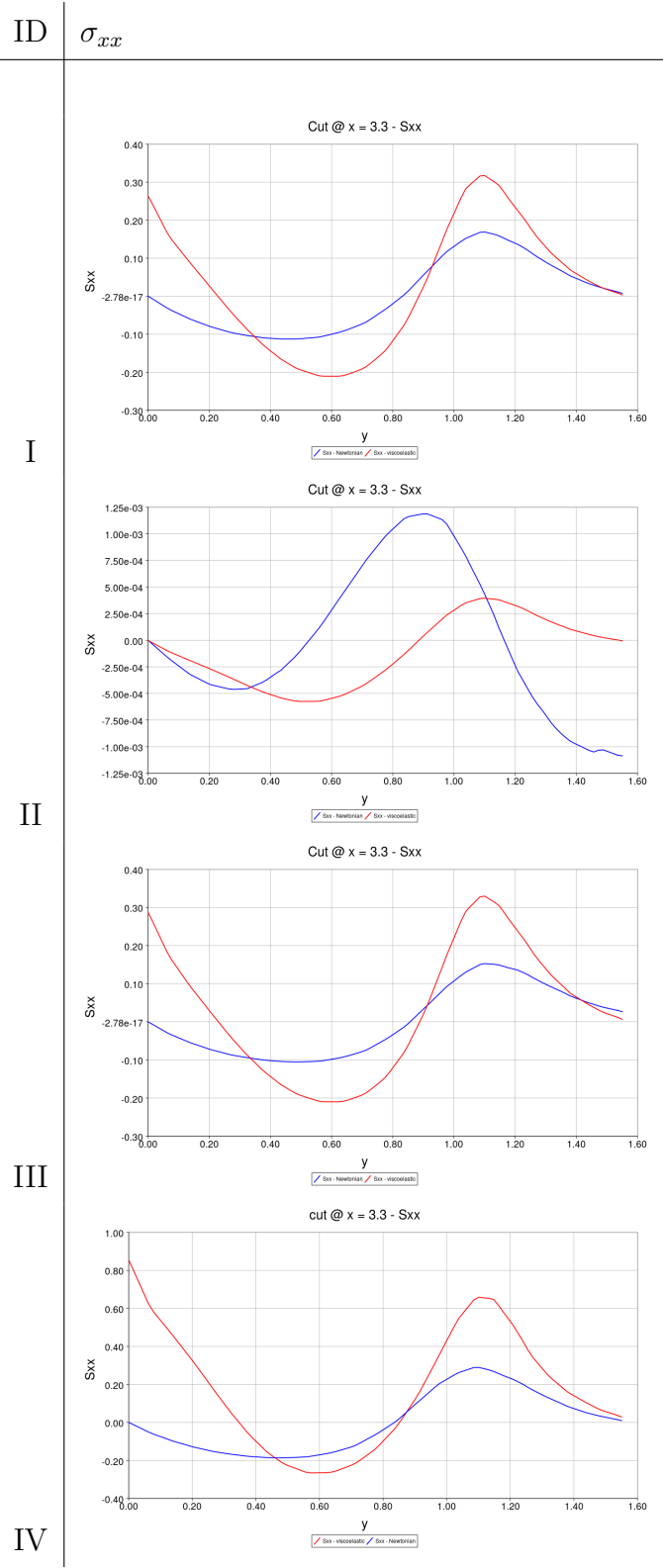


Figure 3.38: Comparison between σ_{xx} for a Newtonian fluid (blue) and a viscoelastic fluid (red) at four different times. The cut is taken along $x = 3.3$.

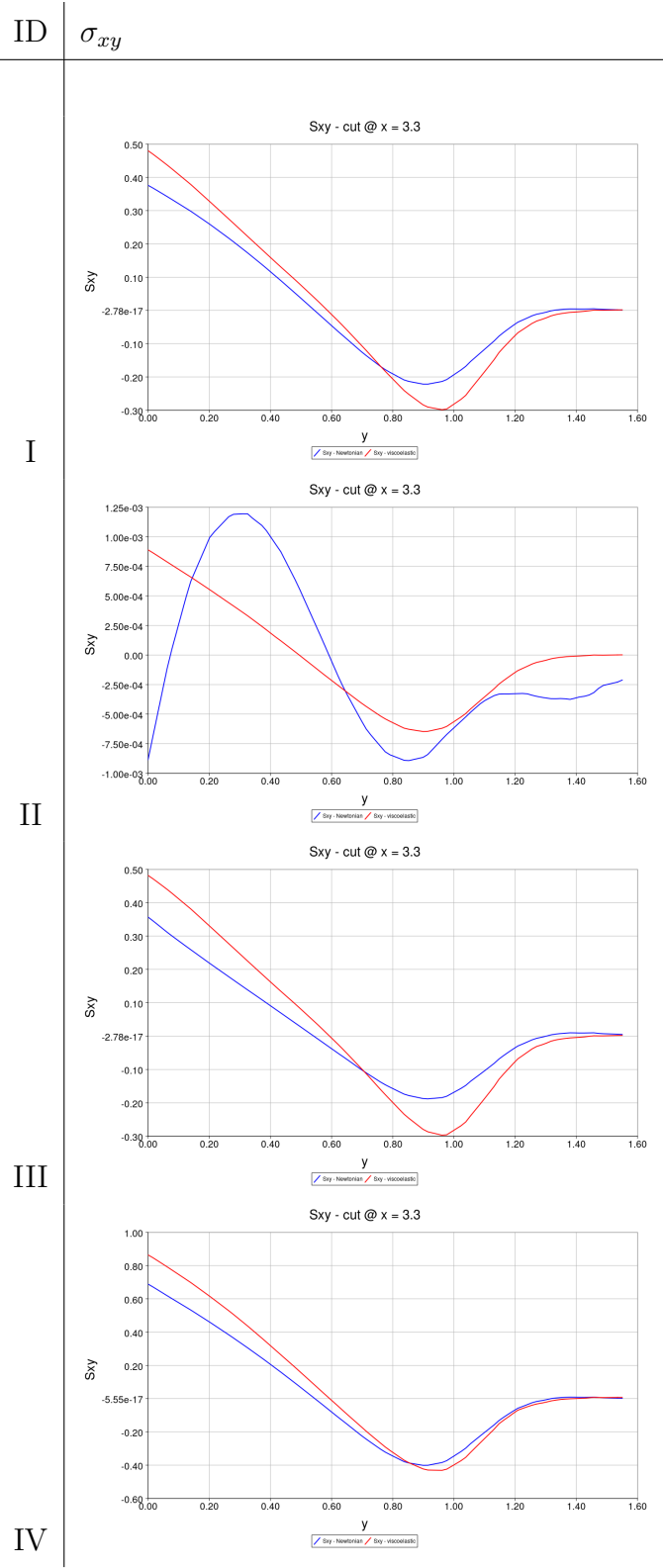


Figure 3.39: Comparison between σ_{xy} for a Newtonian fluid (blue) and a viscoelastic fluid (red) at four different times. The cut is taken along $x = 3.3$.

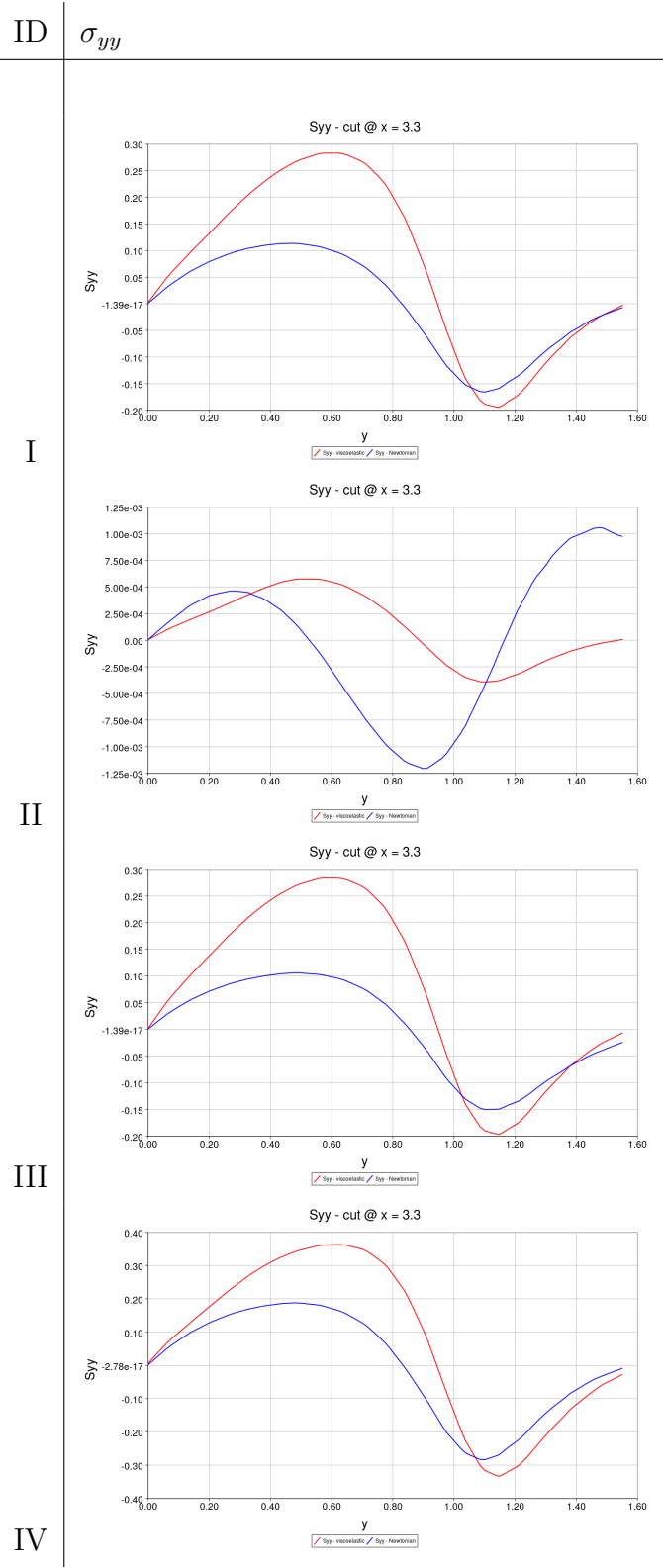


Figure 3.40: Comparison between σ_{yy} for a Newtonian fluid (blue) and a viscoelastic fluid (red) at four different times. The cut is taken along $x = 3.3$.

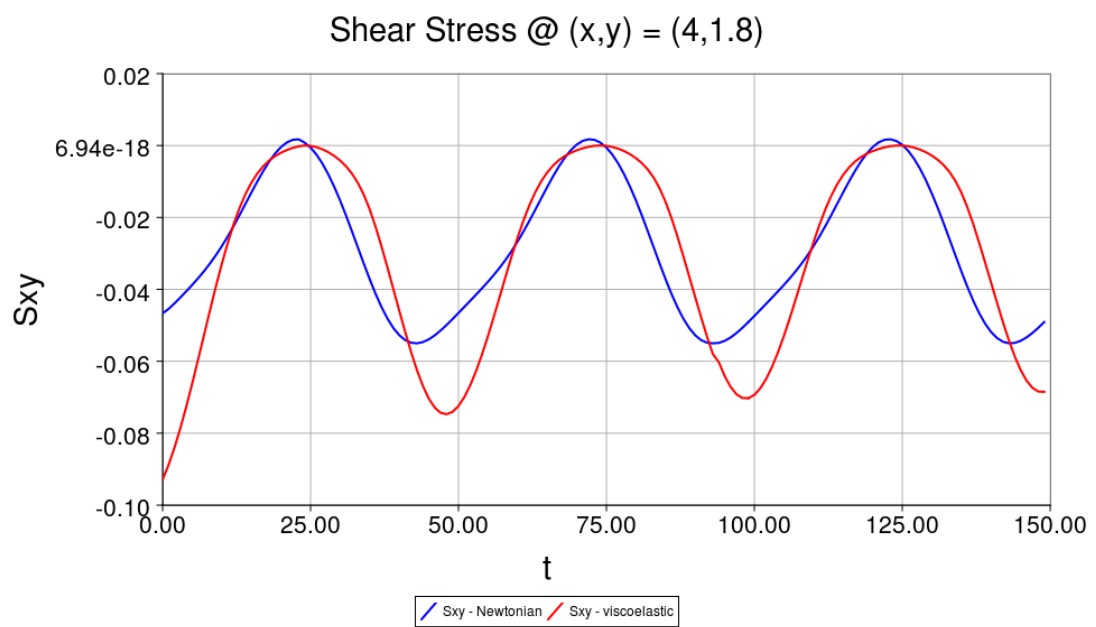


Figure 3.41: Comparison between σ_{xy} for a Newtonian fluid (blue) and a viscoelastic fluid (red) over three pulsatile cycles at the top of the dilation, $(x, y) = (4, 1.81)$.

Chapter 4

Conclusions

This work sets up the framework for the numerical, in particular finite element, solution of microstructure-based, Oldroyd-B type models for blood. Following the 0-D computations in [20] and the 1-D oscillatory flow simulations in [7], we were able to employ the finite element method to perform 2-dimensional pulsatile flow simulations in a non-trivial geometry (our dilated channel). Using physiologically plausible values for the model's parameters in this geometry we found differences in the velocity profiles predicted by the viscoelastic blood model and an equivalent Newtonian fluid. There were also notable differences in the predicted internal stresses. It would be interesting to see how this translates into more complex geometries and in 3D, e.g. for flows in an aneurysm.

From a numerical point-of-view we showed the necessity for utilizing stabilized FEM methods such as the SUPG and DEVSS techniques.

We encountered several roadblocks. As expected, our methods were limited in the range of Deborah number, De , for which we could successfully perform numerical experiments. Also our current computational scheme incurs a rather high computational cost.

There are several possibilities for overcoming those two problems. To overcome the

high De problem one could employ the Log-Conformation method introduced by Fattal et al. [9] where a change of variables introduces the log of the conformation tensor $\mathbf{s} = \log(\boldsymbol{\tau} + \mathbf{I})$. This has been shown to raise the maximum achievable value for De . Another technique is to couple the solver to a mesh adaptation algorithm, as in [13], which refines the mesh selectively near critical areas of the flow. A more fundamental resort involves what is already done in Owens' newer version of his model [17], which is to change the constitutive relation. There are variations on the Oldroyd-B model such as the Giesekus model which can be simulated at much higher values for De (e.g. see [15]).

In terms of performance, the two major improvements would be to implement Newton's method in order to solve the full system at each time step and to approximate $\boldsymbol{\tau}$ and d with less computationally demanding finite element spaces such as the MIX2 element used in [11].

Given the herein studied physical model's rich rheological behaviour as revealed in ours and others' work, it is hoped that the future implementation of the aforementioned techniques will allow the model's features to enter the mainstream of computational haemorheology.

Bibliography

- [1] S. Balay et al. PETSc Web page, <http://www.mcs.anl.gov/petsc>, 2009.
- [2] G. K. Batchelor, **An Introduction to Fluid Dynamics** Cambridge University Press, 1967.
- [3] R. B. Bird, C. F. Curtiss, R. C. Armstrong, and O. Hassager, **Dynamics of Polymeric Liquids, Vol. 2, Kinetic Theory**, Wiley, New York (1977, 2nd edition 1987)
- [4] M. Bureau, J.C. Healy, D. Bourgoïn, M. Joly, Rheological hysteresis of blood at low shear rate, *Biorheology* 17, 191-203, 1980.
- [5] É. Chamberlain, R. Guénette, MEF++ v4.0: Les grands concepts, <http://www.giref.ulaval.ca/coursmefpp/mefpp40grand.pdf>, 2006.
- [6] A. Ern, J.L. Guermond, **Theory and Practice of Finite Elements**, Applied Mathematical Sciences, Springer 2005.
- [7] J. Fang, R. G. Owens, A new microstructure-based constitutive model for human blood, *Biorheology*, 43, 637-660, 2006.
- [8] J. Fang, R. G. Owens, A non-homogeneous constitutive model for human blood Part III. Oscillatory flow, *J. Non-Newtonian Fluid Mech*, 155, 161-173, 2008.

- [9] R. Fattal, R. Kupferman, Time-dependent simulation of viscoelastic flows at high Weissenberg number using the log-conformation representation, *J. Non-Newtonian Fluid Mech*, 126, 23-37, 2005.
- [10] M. Fortin, R. Guénette, R. Pierre, Numerical analysis of the modified EVSS method *Comput. Methods Appl. Mech. Engrg* 143, 79-95, 1997.
- [11] A. Fortin, R. Guénette, R. Pierre, On the discrete EVSS method *Comput. Methods Appl. Mech. Engrg* 189, 121-139, 2000.
- [12] R. Guénette, M. Fortin, A new mixed finite element method for computing viscoelastic flows *J. Non-Newtonian Fluid Mech* 60, 27-52, 1995.
- [13] R. Guénette, A. Fortin, A. Kane, J.-F. Héту, An adaptive remeshing strategy for viscoelastic fluid flow simulations *J. Non-Newtonian Fluid Mech*, 153, 34-45, 2008.
- [14] T. Hughes, J. Marsden, **A Short Course in Fluid Mechanics** Mathematics Lecture Series, Publish or Perish Inc., 1976.
- [15] M. A. Hulsen, R. Fattal, R. Kupferman, Flow of viscoelastic fluids past a cylinder at high Weissenberg number: Stabilized simulations using matrix logarithm, *J. Non-Newtonian Fluid Mech*, 127, 27-39, 2005.
- [16] O. A. Ladyzhenskaya, **The Mathematical Theory of Viscous Incompressible Flow** Gordon and Breach, New York, 1969.
- [17] M. Moyers-Gonzalez, R. G. Owens, J. Fang, A non-homogeneous constitutive model for human blood. Part 1. Model derivation and steady flow, *J. of Fluid Mech*, 617, 327-354, 2008.

- [18] T. de Mulder, Stabilized Finite Element Methods (SUPG, GLS, ...) for incompressible flows *28th CFD Lectures Series at the von Karman Institute for Fluid Dynamics*, March, 1997.
- [19] P. Neofytou, D. Drikakis, Effects of blood models on flows through a stenosis, *International Journal for Numerical Methods in Fluids* 43, 597-635, 2003.
- [20] R. G. Owens, A new microstructure-based constitutive model for human blood, *Journal of Non-Newtonian Fluid Mechanics*, 140, 57-70, 2006.
- [21] R. G. Owens, T.N. Phillips, **Computational Rheology**, Imperial College Press, 2002.
- [22] G.B. Thurston, Elastic Effects in pulsatile blood flow. *Microvasc. Res.* 9, 145-157, 1975.
- [23] C. Tu, M. Deville, Pulsatile flow of non-Newtonian fluids through arterial stenoses *J. of Biomech*, 29, 899-908, 1996.
- [24] J. Zhang, Z. Kuang, Study on blood constitutive parameters in different blood constitutive equations *J. of Biomech*, 33, 355-360, 2000.